Experimental and theoretical investigation of direct frequency comb spectroscopy

Elisabeth Peters

München 2011

Experimental and theoretical investigation of direct frequency comb spectroscopy

Elisabeth Peters

Dissertation
an der Fakultät der Physik
der Ludwig–Maximilians–Universität
München

vorgelegt von
Elisabeth Peters
aus Stepnoje-Osero

München, den 29.03.2011

Erstgutachter: Prof. T. W. Hänsch
Zweitgutachter: Prof. U. Kleineberg
Tag der mündlichen Prüfung: 11.05.2011

Zusammenfassung

Gegenstand der vorliegenden Arbeit ist die experimentelle und theoretische Untersuchung der Zweiphotonen Frequenzkamm-Spektroskopie (DFCS) an atomaren zwei-Niveau Systemen.

Diese Methode stellt ein äußerst vielversprechendes Werkzeug zur Spektroskopie bei kurzen Wellenlängen dar, die mit cw Lasern nur begrenzt oder gar nicht erreichbar sind. Die hohen Spitzenintensitäten eines Frequenzkamms ermöglichen eine effiziente nichtlineare Konversion in bisher unerschlossene Frequenzbereiche, beispielsweise durch Erzeugung von hohen Harmonischen (HHG). Grundlage der DFCS sind theoretische Arbeiten aus den 1970er Jahren, die gezeigt haben, dass der Pulszug eines modengekoppelten Lasers einen Zweiphotonen Übergang ebenso effizient treibt wie ein cw Laser der gleichen mittleren Leistung. Dabei ist die effektive Linienbreite gegeben durch die schmale Breite einer einzelnen Kammmode und nicht durch die spektrale Breite eines Einzelpulses. Damit vereint ein Frequenzkamm die spektrale Reinheit eines cw Lasers mit den hohen Spitzenintensitäten eines gepulsten Lasers.

Zur Demonstration der Eignung nichtlinear konvertierter Frequenzkämme für die Spektroskopie wurde in einem ersten Experiment die Absolutfrequenz einer Zweiphotonen Resonanz in ^{24}Mg bei 431 nm vermessen, wobei Literaturwerte um mehr als zwei Größenordnungen verbessert werden konnten.

Des Weiteren wurden zwei in diesem Zusammenhang wichtige Effekte, die sich auf Übergangsraten auswirken, erstmalig quantitativ untersucht: der Einfluss eines linearen Chirp und eines nicht-zentrierten Laserspektrums auf die Spektroskopie. Die Pulse eines nichtlinear konvertierten Frequenzkamms sind im Allgemeinen nicht Bandbreiten limitiert, was zu einer teilweise destruktiven paarweisen Addition der Moden führt. Zur Beschreibung des Einflusses eines linearen Chirp wurde ein Modell entwickelt und mittels Zweiphotonen Spektroskopie an Cäsium experimentell verifiziert. Überdies haben Theorie und Experiment einen Gaußschen Abfall der Anregungsrate mit zunehmender Dezentrierung des Laserspektrums gezeigt.

Schließlich werden Fortschritte in Richtung einer Spektroskopie des $1S-3S$ Übergangs in Wasserstoff vorgestellt. Dabei handelt es sich um einen viel versprechenden Kandidaten um die Quantenelektrodynamik gebundener Zustände zu testen. Die Übergangswellenlänge von 205nm ist mit cw Lasern nur schwer zu erzeugen, daher bietet sich das System für die DFCS an. Neben einer Beschreibung der experimentellen Fortschritte werden Erkenntnisse, die in der Spektroskopie an Cs und Mg gewonnen wurden, und deren Konsequenzen für die Wasserstoffspektrosopie diskutiert.

Im Rahmen dieser Arbeit wurde ein frequenzvervierfachtes Lasersystem erweitert und verbessert, das ps Frequenzkämme hoher Leistung mit gutem Strahlprofil bei 820 nm, 410 nm und 205 nm erzeugt. Insgesamt stehen nun max. 100 mW bei 205 nm zur Verfügung, die bisher höchste mittels SHG erzeugte Leistung. Darüber hinaus wurde für die H-Spektroskopie ein neues Spektrometer entworfen und gebaut.

Abstract

This thesis reports on theoretical and experimental examination of two-photon direct frequency comb spectroscopy (DFCS) using atomic two-level systems.

This method is a very promising tool to extend optical spectroscopy into the short wavelength region where only few cw laser sources exist. The high peak intensities of pulsed lasers facilitate efficient nonlinear conversion into frequency regions which are so far unexplored, for example by high harmonic generation (HHG). DFCS is based on theoretical work in the 1970s which showed that a pulse train of a mode-locked laser drives a two-photon transition as efficient as a cw laser of same average power. Thereby the effective line width is determined by the narrow width of a single comb mode rather than by the spectral width of a single pulse. In this way a frequency comb combines the spectral purity of a cw laser with the high peak intensity of a pulsed laser.

To demonstrate the capability of a nonlinearly converted frequency comb for DFCS, the absolute frequency of a two-photon transition in ^{24}Mg at 431 nm was measured in a first experiment. The accuracies of the values could be improved by more than two orders of magnitude with respect to previously reported values.

Furthermore two crucial effects which affect the transition rates were analyzed quantitatively for the first time: the impact of a linear chirp and non-centered spectral envelope on the spectroscopy. In general the pulses of a nonlinear converted frequency comb are not bandwidth limited leading to a partially destructive pairwise addition of modes. To describe the impact of a linear chirp a theoretical model was developed and verified experimentally using two-photon spectroscopy on cesium. Moreover, theory and experiment have shown a Gaussian decrease in the transition rate with increasing detuning of the laser spectrum.

Finally the progress of $1S-3S$ spectroscopy in hydrogen is presented. This transition is a promising candidate for a test of bound state quantum electrodynamics. Using cw lasers the required wavelength of 205 nm is hard to generate, making this transition to an eligible system for DFCS. Beside the experimental achievements also the lessons learned from Cs and Mg spectroscopy and their consequences for the H spectroscopy are discussed.

In the scope of this work a frequency quadrupled laser system was extended and improved, providing ps frequency combs of high average power and good beam profile at 820 nm, 410 nm and 205 nm. An overall output power of max. 100 mW is now available at 205 nm, the up to date highest power generated by SHG. Moreover for H spectroscopy a new spectrometer was designed and built.

Contents

1. Introduction

Physics aims to describe natural phenomena quantitatively by using preferably few simple, universal laws. To test and improve the developed theories simple systems are used, which can be calculated with high accuracies and are accessible for high precision experiments. Laser spectroscopy on simple atomic systems is a powerful tool for testing theories. Hydrogen and hydrogen like ions, for example, are the most simple systems and can be calculated within 10^{-12}, while spectroscopy allows for experimental results with unprecedented uncertainty of 10^{-15}.

In 1947, for example, W. E. Lamb and R. C. Retherford observed a small difference in energy levels in hydrogen to the well established model. This experimentally found Lamb shift led to a paradigm shift and in its course to a development of quantum electrodynamics which is the best tested theory at present. Since a theory can never be proved right but one experiment is enough to disprove it, physicists keep measuring atomic transitions with ultra high accuracies.

So far, most of the known transitions lie in the visible (VIS) and near infrared (NIR), where stable continuous wave (cw) lasers are available. However, many interesting but so far unexploited transitions are located in the deep ultra-violet (DUV) and at even shorter wavelengths. Just to name some examples there are two-photon transitions in hydrogen from the ground to higher S and D states which require wavelengths at 243 nm and below and in hydrogen like He^+ at around 61 nm. While 243 nm (H $1S-2S$) can still be generated with sufficient laser power using a cw laser, cw radiation at 205 nm (H $1S-3S$) can only be generated with very low powers (≈ 1 mW) and lower wavelengths are completely inaccessible to cw lasers. In contrast, using a mode-locked laser allows to drive nonlinear processes as second harmonic, sum frequency and high harmonic generation very efficient, which can be used to convert visible and IR lasers into the DUV wavelength region.

Direct frequency comb spectroscopy (DFCS), using a mode-locked laser, is a very promising tool to extend spectroscopy into the so far barely tapped DUV wavelength region. It was first proposed by Ye. V. Baklanov and V. P. Chebotayev in 1970s [1, 2]. In their theoretical work they showed that a pulse train of a mode-locked laser drives a two-photon transition as efficient as a cw laser of same average intensity. At the same time the effective line width is determined by the width of a single comb mode rather

than by the spectral width of a pulse. Hence a frequency comb combines the high peak intensity of a mode-locked laser with the spectral purity of a cw laser.

Shortly after the suggestion of the method, first experimental realization of DFCS was demonstrated by T. W. Hänsch *et al.* [3, 4]. Narrow spectral lines could be observed by exciting the $3S-5S$ transition in sodium using nanosecond pulses inside a passive optical resonator. Using the $3S-4D$ transition in sodium the feasibility of high-resolution two-photon DFCS with picosecond mode-locked lasers was established.

This thesis presents a thorough experimental and theoretical investigation of two-photon DFCS, both at the fundamental and with a non-linearly converted comb. More specifically, two important systematic effects, which affect the transition rates, were studied quantitatively for the first time using a two-photon resonance in Cs at 822 nm: the influence of a linear chirp and of a non-centered spectral envelope.

In general, ultrashort pulses are not necessarily Fourier limited. Upon propagation through a medium, e.g. a nonlinear crystal, they may acquire a nonlinear spectral and/or temporal phase. In a three-level system with a resonant or nearly resonant intermediate state such a nonlinear phase may enhance the transition rate [5–9]. In contrast, in real two-photon absorption in a two-level system this phase leads to a destructive interference of the comb modes, reducing the performance. A simple theoretical model is developed to describe the influence of a linear chirp on the DFCS and its validity is verified using a two-photon resonance in ^{133}Cs at 822 nm. An important result is that although the transition amplitude is reduced by the linear chirp, the line width as well as its position is not affected by the chirp.

Another crucial systematic effect comes along with a detuning of the spectral envelope with respect to the transition frequency. Only if the carrier frequency corresponds to the half of the transition frequency every comb mode on the red side has a counterpart on the blue side and vice versa and the signal is maximized. Theoretical and experimental examination of this effect revealed a Gaussian signal decrease upon shifting the spectral envelope. At the same time a shift of the line center is observed with increasing detuning.

As a proof of principle study of two-photon DFCS with nonlinear converted combs the absolute frequency of a two-photon resonance in ^{24}Mg near 431 nm and the isotope shift between ^{26}Mg and ^{24}Mg are measured. Using this technique the uncertainties of the measured frequencies could be reduced by more than two orders of magnitude with respect to previously reported values. These measurements also serve as test of the laser system and pave the way for H spectroscopy at 205 nm.

In the second part of this thesis prospects to measure the $1S-3S$ two-photon transition in hydrogen at 205 nm are summarized. High precision spectroscopy on simple atomic systems as hydrogen and hydrogen like ions serves as an excellent test of bound-state quantum electrodynamics (QED), which is the best tested theory at present. Narrow two-photon transitions can be measured with an unprecedented accuracy. One of the currently most precise measurements is the first order Doppler-free $1S-2S$ two-photon

resonance in hydrogen with an uncertainty of around 10^{-14} which has a long tradition in our group. However theoretical predictions do not reflect this accuracy. One of the parameters entering into theoretical calculations, the proton charge radius, is only known within 2 % and limits theoretical predictions. Recently R. Pohl *et al.* [10] succeeded in measuring the Lamb shift in muonic hydrogen providing a proton charge radius with a greatly reduced uncertainty but 5 standard deviations away from the recommended value by CODATA. This discrepancy brings up new questions and for their clarification further high precision measurements are necessary.

Combining at least two narrow two-photon resonances in H and utilizing the $1/n^3$ scaling law for the Lamb shifts, leading QED contributions containing the proton charge radius cancel out. This allows an experimental determination of the values for the Rydberg constant and the ground state Lamb shift with an improved accuracy limited by the uncertainty of the frequency intervals rather than by the rms proton charge radius. Transitions from the ground state are experimentally easier accessible and are less sensitive to electric fields, allowing for higher accuracies than could be achieved in, say, $2S - 8S/D$ and $2S - 12D$ measurements. Therefore, $1S - 3S$ is a promising candidate for this purpose and in our group as well as in the group around F. Biraben an experiment to measure this transition was set up.

The group in Paris probes this transition with a cw laser, whereby the required UV light at 205 nm wavelength is generated by frequency quadrupling a Ti:sapphire laser at 820 nm in two subsequent resonant second harmonic generation (SHG) stages providing up to 1 mW output power. While the first SHG stage works very well, the second one is operated close to the cut-off of phase matchable wavelength. Additionally two limiting effects could be observed: photochemical reactions on the crystal faces and the photo refractive effect [11]. After servo locking the cavity the intra cavity power at 410 nm as well as the generated 205 nm wavelength catalyze photochemical reactions on the faces of the crystal, resulting in permanent damage within several minutes. This can partly be suppressed by flushing the crystal faces with oxygen. On a longer time scale a counter propagating beam at 410 nm appears in the ring cavity. Finally both beams are of equal intensity and the second harmonic power is reduced by a factor four. This behavior can be attributed to the photo refractive effect. To improve the performance of this conversion step the cavity is operated in a quasi-continuous regime, i.e. the cavity is over modulated at 15 kHz such that it is resonant twice per modulation period. In this way 6 μs long pulses at a repetition rate of 30 kHz are generated. Due to this modulation an additional Doppler shift is introduced to the resonance line. Furthermore the spectroscopy is carried out on a thermal atomic beam ($v = 2500$ m/s) resulting in a strong velocity dependent line shift and broadening.

Due to these drawbacks this system is an ideal candidate for DFCS. Our approach is to drive the transition with a mode-locked laser. By frequency quadrupling a ps Ti:sapphire laser at 820 nm in two successive resonant SHG stages, 2 ps long pulses

at 82 MHz repetition frequency are generated with 100 mW maximum average power. Resonant conversion allows to use a shorter nonlinear crystal to maintain a good spatial beam profile without losing second harmonic power.

This thesis is organized as follows: In the second chapter theoretical concepts of DFCS are summarized for later reference. The third chapter describes in detail the laser system generating frequency combs at 820, 410 and 205 nm and its performance. A demonstration of the method using a two-photon resonance in Cs and investigation of crucial systematic effects are described in chapter four. In chapter five spectroscopy in Mg is described, which demonstrates the feasibility of two-photon DFCS with nonlinearly converted combs. Finally, chapter six summarizes the progress to measure the $1S - 3S$ two-photon resonance in H.

2. Direct frequency comb spectroscopy

Optical frequency combs, honored by the Nobel prize in 2005, have revolutionized spectroscopy. Their main field of application was so far calibration of a spectroscopy laser, which was usually a cw laser. However, as was proposed by Ye. V. Baklanov and V. P. Chebotayev [1, 2] and demonstrated by T. W. Hänsch *et al.* [3, 4], a frequency comb can be utilized for spectroscopy directly. Some of the current applications of DFCS are reviewed by M. C. Stowe *et al.* in ref. [12].

In contrast to one-photon frequency comb spectroscopy, where only one comb mode is used, in two-photon DFCS the combined power of all modes is used to probe the transition. In this way a pulse train drives a two-photon transition as efficient as a cw laser of same average power. At the same time the effective line width is limited by the spectral width of a single mode rather than by the bandwidth of a pulse. Furthermore the high peak intensity of a pulsed laser facilitates efficient non-linear conversion into DUV and XUV wavelength regions e.g. by high harmonic generation (HHG). Hence a frequency comb combines the spectral purity of a cw laser with the high peak intensity of a pulsed laser. Therefore DFCS promises to make previously inaccessible wavelengths accessible.

In an experiment several systematic effects can broaden and shift the spectral lines. In gaseous samples the major broadening mechanism results from the motion of the gas particles (Doppler effect). Utilizing a Doppler-free arrangement, where two counter propagating pulses drive the transition, the Doppler effect cancels in first order. This allows for high resolution spectroscopy of ultra narrow spectral lines. However, also two photons propagating in the same direction can be absorbed providing a Doppler-broadened background signal. The actual signal is a narrow spectral line superimposed on a Doppler pedestal.

In this chapter the theoretical aspects of DFCS are presented. In the first part the basic idea of the method is described. In the second part optical Bloch equations for two-photon spectroscopy are derived and solved first for cw excitation and then for the more general case of DFCS. In the latter case transform limited pulses are assumed, but in general short pulses easily acquire a chirp. Therefore DFCS with chirped pulses is

treated in the third part. In the last part, finally, it is shown that the transition rate is maximized for a perfectly centered spectral pulse envelope. A relation is provided to describe the signal decrease with increasing spectral detuning.

2.1. Method of DFCS

In this section the basic idea of the method of DFCS is presented. Before describing the method a short review of the frequency comb basics is given. In the end an expression for the contrast between the Doppler-free signal and the Doppler pedestal is derived.

2.1.1. Comb basics

Consider a periodic sequence of light pulses emitted by a mode-locked laser with a repetition rate ω_r. The electric field of the pulses $E(t) = \mathcal{E}(t)\sin(\omega_0 t)$ oscillates at a carrier frequency ω_0 with a real pulse envelope function $\mathcal{E}(t)$. In frequency domain such a pulse train corresponds to regularly spaced narrow frequency modes centered around the carrier ω_0. The spacing of the modes corresponds to the pulse repetition rate ω_r (figure 2.1). Looking closely one finds that the comb modes are not simply integer multiples of the pulse repetition rate, but are rather shifted by an offset frequency ω_{ce}

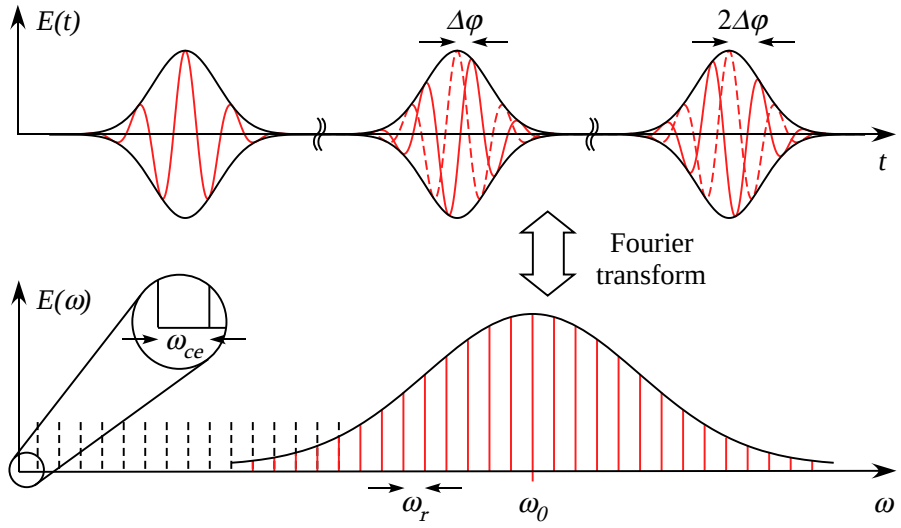

Figure 2.1.: *Temporal and spectral representation of a mode-locked laser. Upper part: Pulse train containing three subsequent pulses. While propagating through a resonator the pulses acquire a pulse to pulse phase shift $\Delta\varphi$. Lower part: Spectrum of an infinitely long pulse train centered around the carrier frequency ω_0. The comb modes are separated by the pulse repetition rate ω_r and are shifted by the carrier-offset frequency $\omega_{ce} = \Delta\varphi\omega_r/2\pi$ (inset).*

(see inset in figure 2.1). This frequency shift can be attributed to a pulse to pulse phase shift $\Delta\varphi$ between the carrier and the envelope function [13] and is thus referred to as carrier-envelope frequency (CE-frequency).

The mode structure, described above, is the so-called frequency comb and the frequency of the n-th mode is given by $\omega_n = \omega_{ce} + n\omega_r$. Setting now the carrier frequency $\omega_0 = \omega_{ce} + n_0\,\omega_r$ and reenumerate the comb modes such that they are counted with respect to ω_0 ($n = n_0 + m$), the frequencies of the comb modes can be written in the form

$$\omega_m = \omega_0 + m\omega_r\,. \tag{2.1}$$

2.1.2. Interaction of a comb with a two-level system

With the expression for the frequencies of the comb modes (equation (2.1)) the interaction of a frequency comb with a two-level system can now be described.

Consider an atomic two-level system with a ground state $|g\rangle$ and an excited state $|e\rangle$ interacting with the electric field of two counter propagating pulse trains. After being excited the atom decays back into the ground state with a decay rate γ. Provided that γ is much smaller than the mode spacing of the comb ($\gamma \ll \omega_r$) the comb modes appear as narrow cw lasers which probe the transition. Tuning the comb on resonance ($\Delta\omega = \omega_{eg}/2 - \omega_0 = 0$, ω_{eg} is the frequency interval between the ground and the excited state), every mode on the red side of the pulse has a counterpart on the blue side and vice versa and all modes can add up pairwise, as shown in figure 2.2. If the comb modes are all properly phased, this addition is totally constructive.

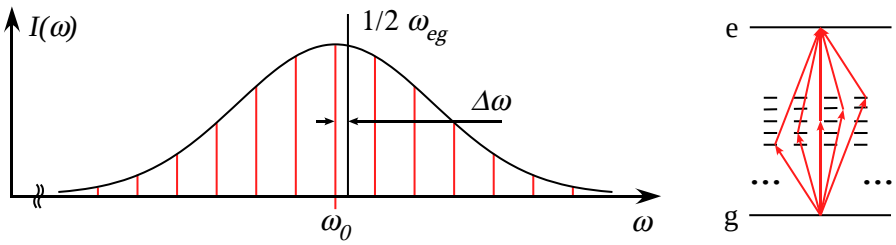

Figure 2.2.: *Left: spectral envelope centered around ω_0 with a detuning $\Delta\omega = (1/2)\omega_{eg} - \omega_0$. Right: on resonance ($\Delta\omega = 0$) a pairwise addition of properly phased modes provides an efficient excitation of the atoms.*

In general the atoms are not at rest but rather move with velocity $\boldsymbol{v}$. Due to the Doppler-effect the moving atoms see a laser frequency shifted by $-\boldsymbol{k}\cdot\boldsymbol{v}$, where $\boldsymbol{k}$ is a wave vector. To drive the two-photon transition the following condition must be fulfilled

$$\omega_{eg} = 2\omega_0 + (m + m')\,\omega_r - (\boldsymbol{k}_m + \boldsymbol{k}_{m'})\cdot\boldsymbol{v}\,, \tag{2.2}$$

where $\boldsymbol{k}_m$ and $\boldsymbol{k}_{m'}$ are wave vectors of mode m and m'. When the atoms absorb two counter propagating photons of equal frequency ($\boldsymbol{k}_m = -\boldsymbol{k}_{m'}$) the velocity dependent term in equation (2.2) vanishes. This gives rise to a narrow in first order Doppler-free spectral line. Detuning the frequency comb ($\Delta\omega \neq 0$), the signal repeats itself with $\omega_r/2$ appearing at the points

$$\omega_0 = \frac{\omega_{eg}}{2} - (m + m')\frac{\omega_r}{2}\,. \tag{2.3}$$

The atoms may also absorb two photons coming from the same direction. In this case the velocity dependent term in equation (2.2) does not cancel and an integration over all velocities yields a Doppler-broadened background signal. Hence the actual signal obtained in an experiment shows a narrow Doppler-free resonance line of natural line width superimposed on a Doppler-broadened pedestal (see figure 2.3). Using circularly polarized light the Doppler background can be suppressed.

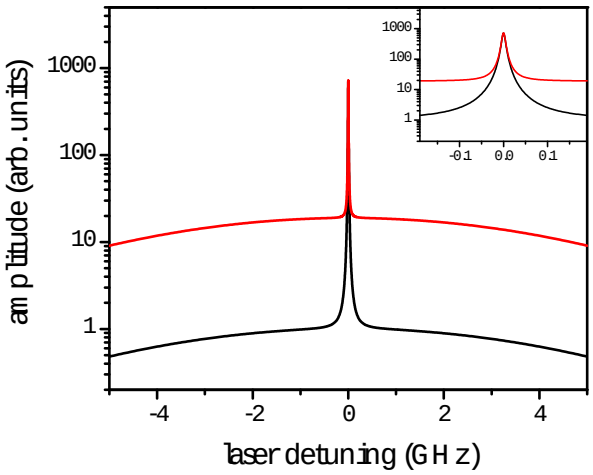

Figure 2.3.: *Sample curves of a two-photon signal for a linearly polarized cw laser (black curve) and a mode-locked laser (red curve). The curves show the 1st-order Doppler-free signal superimposed on a Doppler-broadened pedestal. The inset shows a blow-up of the narrow resonance.*

2.1.3. Contrast between the Doppler-free signal and the background

Using linearly polarized light for two-photon spectroscopy, the atoms can absorb either two photons propagating in the same direction or two counter propagating photons, as described above. The resulting signal is a superposition of a narrow Lorentzian spectral line with amplitude $\Re_{\mathrm{L}} = 4|\Omega|^2/(\gamma\pi)$ and a Doppler-broadened Gaussian pedestal with amplitude $\Re_{\mathrm{G}} = |\Omega|^2/(kv_p\sqrt{\pi})$ (see figure 2.3), where Ω is a two-photon Rabi frequency defined as [14]

$$\Omega = 2(2\pi\beta_{eg})(\varepsilon_0 c)E_1(t)E_2(t)\,, \tag{2.4}$$

with the dielectric constant ε_0, c the speed of light, β_{eg} the transition matrix element and $E_1(t)$, $E_2(t)$ the forth and back propagating electric field. The narrow spectral line

depends on the decay rate γ of the excited state while the Doppler-broadened background depends on the most probable velocity $v_p = \sqrt{2k_\mathrm{B}\,T/M}$ and the wave number $k = 2\omega_0/c$, where k_B is the Boltzman constant, T the gas temperature and M the atomic mass.

Probing the transition with a cw laser, the electric fields $E_1 = \sqrt{2\mathcal{I}_1/(\varepsilon_0 c)}$ and $E_2 = \sqrt{2\mathcal{I}_2/(\varepsilon_0 c)}$, with intensities $\mathcal{I}_1$ and $\mathcal{I}_2$, are constant and $\Omega = 4(2\pi\beta_{eg})\sqrt{\mathcal{I}_1\mathcal{I}_2}$. One can now define a contrast C_cw as a ratio between the Lorentzian and Gaussian amplitude [15]

$$C_\mathrm{cw} = \frac{\mathfrak{R}_\mathrm{L}}{\mathfrak{R}_\mathrm{G}} = \frac{4k\,v_p}{\gamma\sqrt{\pi}}\,. \tag{2.5}$$

Driving the transition with a frequency comb the electric field of a single comb mode m can be approximated by $E_{m,m'} = \sqrt{2\mathcal{I}_{1,2}/(\varepsilon_0 cN)}$ where $\mathcal{I}_{1,2}$ is the average intensity in the first and second beam and N the total number of modes. As described in the previous section, in two-photon spectroscopy all modes with $m = -m'$ contribute to drive the transition, so the Rabi frequency can be written as

$$\Omega = \sum_{m=1}^{N} 2(2\pi\beta_{eg})(\varepsilon_0 c)E_m^2 = 4(2\pi\beta_{eg})\sqrt{\mathcal{I}_1\mathcal{I}_2}\,. \tag{2.6}$$

This is exactly the same Rabi frequency as obtained for the cw case above and is valid for the Doppler-free spectral line and for the amplitude of a Doppler-broadened line resulting from one velocity component. In contrast to the cw case, not only one but rather all velocity components within the Maxwell distribution which are covered by the FWHM bandwidth $\Delta\omega_L$ of the laser contribute to the Doppler background. Hence the background is enhanced by the number of velocity components which are addressed by the laser. For a Doppler width $\omega_D = 2\sqrt{\ln(2)}\,k\,v_p$ narrower than the laser bandwidth ($\omega_D < \Delta\omega_L$), the increase of the background can be approximated by $2\omega_D/\omega_r$ reducing the contrast to

$$C_\mathrm{comb} = \frac{4k\,v_p}{\gamma\sqrt{\pi}}\,\frac{\omega_r}{2\omega_D} = \frac{\omega_r}{\gamma\sqrt{\pi\ln(2)}}\,. \tag{2.7}$$

This contrast may be further reduced if several spectral lines, as e.g. hyperfine components and transitions to lower or higher levels, are addressed by the laser. While the Doppler-free component splits into a corresponding amount of lines with the respective relative amplitudes, the background is formed by a superposition of the Doppler-broadened signals of all the addressed lines. Furthermore the narrow spectrum originates only from the pulse collision volume, where two counter-propagating photons can be absorbed, whereas the Doppler-broadened signal is generated all along the laser beam including the pulse collision volume. The approximation in equation (2.7) applies only for the pulse collision volume. In the experiment the imaged volume may exceed this region, downgrading the contrast.

2.2. Optical Bloch equations

After the general description of the method in the previous section, in this section the interaction dynamics are treated resulting in a set of optical Bloch equations. These equations are solved first for a cw laser and then for the more general case of a frequency comb. In the last part an overview of the two-photon absorption selection rules is given.

A semi classical model is used to describe the interaction between a laser field and a two-level atomic system. The electric field $E(t)$, traveling along the z-axis, is treated classically and the atom quantum mechanically by a wave function ψ. The unperturbed atom is described by a time independent Hamiltonian H_0 with the eigenstates $|n\rangle$ and the eigenvalues $\mathfrak{E}_n = \hbar\omega_n$ ($\hbar$ is the Planck constant over 2π), which correspond to the Bohr energy levels. Switching on the laser field introduces a time dependent perturbation $V(t)$, which induces transitions between the eigenstates of the unperturbed system. The time-dependent Schrödinger equation

$$i\hbar\frac{\partial}{\partial t}\left|\psi(t)\right\rangle = H(t)\left|\psi(t)\right\rangle = \Big(H_0 + V(t)\Big)\left|\psi(t)\right\rangle, \tag{2.8}$$

with the time dependent Hamiltonian $H(t)$ and states $|\psi(t)\rangle$ describes the time evolution of the system, but does not contain damping due to spontaneous decay of the excited state and ionization. Switching over to the density matrix formalism, damping terms can easily be included in form of a matrix $\Gamma(\rho)$. All virtual intermediate states are off-resonant with respect to one-photon absorption, thus their relaxation can be neglected and only the spontaneous decay of the excited state will be considered here. The time evolution of the density matrix ρ with the matrix elements $\rho_{nm}(t) = \langle n|\rho(t)|m\rangle = c_n(t)c_m^*(t)$, obeys the Liouville equation:

$$i\hbar\dot{\rho} = [H(t),\rho] + i\hbar\Gamma(\rho)\ . \tag{2.9}$$

In this thesis we are only interested in two-photon transitions in an effective two-level system. Hence, keeping only the terms which reflect the two-photon nature of the transition, the optical Bloch equations can be written in the form [2]:

$$\dot{\rho}_{ng}(t) = -i\big[\omega_{ng} + \Delta\omega_{ng}^{\mathrm{AC}}\big]\rho_{ng}(t) - \frac{i}{\hbar}V_{ng}(t)\rho_{gg}(t)\,, \tag{2.10a}$$

$$\dot{\rho}_{eg}(t) = \Big[-i(\omega_{eg} + \Delta\omega_{eg}^{\mathrm{AC}}) - \frac{\gamma}{2}\Big]\,\rho_{eg}(t) - \frac{i}{\hbar}\sum_n V_{en}(t)\rho_{ng}(t)\,, \tag{2.10b}$$

$$\dot{\rho}_{en}(t) = -i\big[\omega_{en} + \Delta\omega_{en}^{\mathrm{AC}}\big]\rho_{en}(t) + \frac{i}{\hbar}V_{ng}^*(t)\rho_{eg}(t)\,, \tag{2.10c}$$

$$\dot{\rho}_{ee}(t) = -\gamma\rho_{ee}(t) + \frac{i}{\hbar}\sum_n \big[V_{en}^*(t)\rho_{en}(t) - V_{en}(t)\rho_{en}^*(t)\big]\,, \tag{2.10d}$$

where $\omega_{ij} = (\omega_i - \omega_j)$ is the frequency interval between the states i and j ($i,j = e,g,n$), $\Delta\omega_{ij}^{\mathrm{AC}} = \omega_{\mathrm{AC}}(i) - \omega_{\mathrm{AC}}(j)$ is the total AC-Stark shift of the transition, $V_{ij}(t) = \langle i|V(t)|j\rangle$ are the interaction matrix elements, and $\gamma = 2\pi\nu_\gamma$ is the decay rate of the excited state.

2.2.1. Transition rate – continuous wave excitation

The optical Bloch equations (2.10) can be solved using time-dependent perturbation theory. With the initial condition that for $t \leq 0$ all atoms are in the ground state ($\rho_{gg} = 1$ and $\rho_{ng} = \rho_{eg} = \rho_{en} = \rho_{ee} = 0$) the solutions read

$$\rho_{ng}(t) = -e^{-i(\omega_{ng}+\Delta\omega_{ng}^{\mathrm{AC}})t}\,\frac{i}{\hbar}\int_0^t V_{ng}(t')\,e^{i(\omega_{ng}+\Delta\omega_{ng}^{\mathrm{AC}})t'}\,\mathrm{d}t'\,, \tag{2.11a}$$

$$\rho_{eg}(t) = -e^{-i(\omega_{eg}+\Delta\omega_{eg}^{\mathrm{AC}})t-\gamma t/2}\,\frac{i}{\hbar}\int_0^t \sum_n V_{en}(t')e^{i(\omega_{eg}+\Delta\omega_{eg}^{\mathrm{AC}})t'+\gamma t'/2}\,\rho_{ng}(t')\,\mathrm{d}t'\,, \tag{2.11b}$$

$$\rho_{en}(t) = e^{-i(\omega_{en}+\Delta\omega_{en}^{\mathrm{AC}})t}\,\frac{i}{\hbar}\int_0^t V_{ng}^*(t')\,e^{i(\omega_{en}+\Delta\omega_{en}^{\mathrm{AC}})t'}\,\rho_{eg}(t')\,\mathrm{d}t'\,, \tag{2.11c}$$

$$\rho_{ee}(t) = e^{-\gamma t}\,\frac{i}{\hbar}\int_0^t \sum_n \left[V_{en}^*(t')\,e^{\gamma t'}\,\rho_{en}(t') - V_{en}(t')\,e^{\gamma t'}\,\rho_{en}^*(t')\right]\,\mathrm{d}t'\,. \tag{2.11d}$$

In dipole approximation the interaction potential is given by the dipole moment operator $\mathfrak{p}$ times the electric field, $V(t) = -\mathfrak{p}\cdot\boldsymbol{E}(t)$. Assuming a Doppler-free arrangement the total electric field $\boldsymbol{E}(t)$ is a superposition of two counter propagating electric fields with frequencies $\omega_1 = \omega_{01} + \boldsymbol{k}_1\cdot\boldsymbol{v}$ and $\omega_2 = \omega_{02} + \boldsymbol{k}_2\cdot\boldsymbol{v}$, polarizations $\boldsymbol{\epsilon}_1$ and $\boldsymbol{\epsilon}_2$ and constant field amplitudes E_{01} and E_{02}:

$$\begin{aligned}\boldsymbol{E}(t) &= \frac{1}{2}\left(\boldsymbol{E}_1(t) + \boldsymbol{E}_1^*(t)\right) + \frac{1}{2}\left(\boldsymbol{E}_2(t) + \boldsymbol{E}_2^*(t)\right)\\ &= \frac{1}{2}\boldsymbol{\epsilon}_1\left(E_{01}e^{-i\omega_1 t} + E_{01}^* e^{i\omega_1 t}\right) + \frac{1}{2}\boldsymbol{\epsilon}_2\left(E_{02}\,e^{-i\omega_2 t} + E_{02}^*\,e^{i\omega_2 t}\right)\,.\end{aligned} \tag{2.12}$$

Using this total electric field the integrals in equations (2.11) can be solved successively. For two laser fields of equal frequency ($\omega_{01} = \omega_{02} = \omega_0$) and equal polarization ($\boldsymbol{\epsilon}_1 = \boldsymbol{\epsilon}_2 = \boldsymbol{\epsilon}$) propagating in the z direction ($\boldsymbol{k}\cdot\boldsymbol{v} = kv_z$) and with the matrix elements $\mathfrak{p}_{en} = \langle e|\boldsymbol{\epsilon}\cdot\mathfrak{p}|n\rangle$ and $\mathfrak{p}_{ng} = \langle n|\boldsymbol{\epsilon}\cdot\mathfrak{p}|g\rangle$ the resulting excited state population can be written

$$\begin{aligned}\rho_{ee}(t) = \frac{1}{16\,\hbar^4}\left|\sum_n \frac{\mathfrak{p}_{en}\,\mathfrak{p}_{ng}}{\omega_{ng}-\omega_0}\right|^2 \Bigg[&\frac{4\,|E_{01}E_{02}|^2}{(\omega_{eg}-2\,\omega_0)^2+\gamma^2/4} + \\ &\frac{|E_{01}^2|^2}{(\omega_{eg}-2\omega_0-2kv_z)^2+\gamma^2/4} + \frac{|E_{02}^2|^2}{(\omega_{eg}-2\omega_0+2kv_z)^2+\gamma^2/4}\Bigg]\,,\end{aligned} \tag{2.13}$$

which corresponds to the two-photon transition probability from the ground to the excited state. The first term in the square bracket gives the Doppler-free resonance generated by absorption of two counter-propagating photons and the last two terms give the Doppler shifted resonances, caused by absorption of two photons propagating in

the same direction. Assuming a thermal velocity distribution along the z direction and averaging over all velocities results in a superposition of two Doppler-broadened lines, which forms the Doppler background. In high precision spectroscopy only the narrow Doppler-free component is of interest, thus the Doppler-background is omitted in further considerations. The resulting Doppler-free two-photon transition rate can be written in the form

$$\mathfrak{R}_{ge} = \gamma\rho_{ee}(t) = \frac{4(2\pi\beta_{eg})^2\mathcal{I}_1\mathcal{I}_2\,\gamma}{(\omega_{eg}-2\omega_0)^2+\gamma^2/4} = \frac{\gamma|\Omega|^2/4}{(\omega_{eg}-2\omega_0)^2+\gamma^2/4}\,, \tag{2.14}$$

with the two-photon Rabi frequency Ω as given in equation (2.4) and the transition matrix element β_{eg} defined by [14]

$$\beta_{eg} = \frac{1}{2\hbar h\varepsilon c}\left|\sum_n \frac{\mathfrak{p}_{en}\,\mathfrak{p}_{ng}}{\omega_{ng}-\omega_0}\right|\,. \tag{2.15}$$

2.2.2. Transition rate – pulsed excitation

Based on the solutions found in the previous section the transition rate for DFCS is calculated in this section. Therefore the temporal profile of the laser beams is assumed to be Gaussian[i] and the field amplitudes of the counter propagating beams become time dependent. Assuming linearly polarized light, the total electric field of two counter propagating pulse trains at any axial position z can be written as

$$E(t,z) = \frac{1}{2}\left(E_{01}\,\mathcal{E}(t+z/c)\,e^{-i(\omega_1 t+kz)} + E_{02}\,\mathcal{E}(t-z/c)\,e^{-i(\omega_2 t-kz)}\right) + \text{c.c.}\,, \tag{2.16}$$

with a time dependent envelope function $\mathcal{E}(t\pm z/c)$. The transverse spatial dependence of the electric field is neglected here, but can be included by simply multiplying the field by a factor $\exp\left[-r^2/w_0^2\right]$ where $r^2=x^2+y^2$ and w_0 is the beam waist radius. Assuming transform limited pulses, the temporal and spectral envelope functions of the electric field can be written as

$$\mathcal{E}(t\pm z/c) = \frac{1}{\sqrt{\tau}}\sqrt[4]{\frac{2}{\pi}}\,\exp\left[-\left(\frac{t\pm z/c}{\tau}\right)^2\right]\,, \tag{2.17a}$$

$$\mathcal{E}(\omega) = \frac{\sqrt{\tau}}{\sqrt[4]{2\pi}}\,\exp\left[-\frac{1}{4}(\tau\omega)^2 \pm \frac{i\omega z}{c}\right]\,, \tag{2.17b}$$

which are normalized such that the pulse energy is independent of the pulse duration τ. The intensity full widths at half maximum (FWHM) of the envelopes in equations (2.17)

[i] Although the pulses may have a different pulse shape, a Gaussian is a good approximation in most cases.

are $\Delta t = \tau\sqrt{2\ln(2)}$ and $\Delta\nu = \sqrt{2\ln(2)}/(\tau\pi)$, so the time bandwidth product (TBP), indicating transform limited pulses, is given by

$$\Delta t\,\Delta\nu = \frac{2\ln(2)}{\pi}\,. \tag{2.18}$$

The spectral envelope in equation (2.17b) may be used to model the electric field of a frequency comb. Substituting $\omega \to m\omega_r$ in equation (2.17b) with the mode number $m = \{0, \pm1, \pm2, ...,\}$ and assuming a pulse train with a monochromatic carrier which spectral envelope is a Delta-function, the renormalized electric field of the frequency comb propagating in the z direction can be written in the form

$$E_{1,2}(t,z) = E_{01,02}\sum_m \mathcal{E}'(m\omega_r)\,e^{-i\omega_1 t - ik_m z}\,, \tag{2.19}$$

where $\mathcal{E}'(m\omega_r) = \sqrt{\omega_r}\mathcal{E}(m\omega_r)$ is the renormalized envelope function. For two counter-propagating fields with frequencies $\omega_1 = \omega_m = \omega_0 + m\omega_r$ and $\omega_2 = \omega_{m'} = \omega_0 + m'\omega_r$ the Doppler-free two-photon transition rate can be written in the form

$$\mathfrak{R}_{ge}^{\mathrm{comb}} = \frac{1}{4}(c\varepsilon_0)^2\left(\frac{2\pi}{2\hbar hc\varepsilon_0}\right)^2\left|\sum_{m,m'}\frac{E_{01}E_{02}\mathcal{E}'(m\omega_r)\mathcal{E}'(m'\omega_r)e^{-i(\omega_m+\omega_{m'})t-(k_m-k_{m'})z}}{i(\Delta\omega_{eg}+(m+m')\omega_r)+\gamma/2}\right.$$
$$\left.\sum_n\frac{\mathfrak{p}_{en}\,\mathfrak{p}_{ng}}{\omega_{ng}-\omega_0-m\omega_r}+\frac{\mathfrak{p}_{en}\,\mathfrak{p}_{ng}}{\omega_{ng}-\omega_0-m'\omega_r}\right|^2\,, \tag{2.20}$$

where $\Delta\omega_{eg} = 2\omega_0 - \omega_{eg}$ is the detuning. The mode numbers m and m' count the comb modes with respect to the carrier frequency $\omega_0 = \omega_{eg}/2$, thus only the modes with $m' = -m$ are resonant, all the other modes are off-resonant and can be neglected. Furthermore the spectral half width at half maximum of the laser pulses amounts to around 70 GHz while the laser frequency is 1.5×10^{15} Hz, thus $\omega_0 + m\omega_r \approx \omega_0$ is a good approximation in equation (2.20). Substituting the electric fields in equation (2.20) by equation (2.19), setting $m' = -m$ and approximating $\omega_0 + m\omega_r$ by ω_0 results in

$$\mathfrak{R}_{ge}^{\mathrm{comb}} = 4(2\pi\beta_{eg})^2\frac{\mathcal{I}_1\mathcal{I}_2\,\gamma}{\Delta\omega_{eg}^2+\gamma^2/4}\,\frac{(\tau\omega_r)^2}{2\pi}\left|\sum_m\exp\left[-\frac{1}{2}(\tau m\omega_r)^2 + i2m\omega_r\frac{z}{c}\right]\right|^2\,, \tag{2.21}$$

Assuming a sufficient number of modes the sum over m in equation (2.21) may be approximated by an integral resulting finally in

$$\mathfrak{R}_{ge}^{\mathrm{comb}} = 4(2\pi\beta_{eg})^2\mathcal{I}_1\mathcal{I}_2\,\frac{\gamma}{\Delta\omega_{eg}^2+\gamma^2/4}\,e^{-4z^2/(c\tau)^2}\,. \tag{2.22}$$

This solution shows that the transition rate $\mathfrak{R}_{ge}$ is proportional to the product of the average intensities $\mathcal{I}_1$ and $\mathcal{I}_2$ rather than to the peak intensities in the two counter

propagating beams. The exponential decrease of the transition rate with z^2 in equation (2.22) is just due to a fall off of the laser intensity away from the pulse collision point. A comparison of equation (2.22) with (2.14) shows that probing a two-photon transition with a mode-locked laser yields the same transition rate as with a cw laser of same average laser power ($z = 0$). The Doppler-free resonance shows a Lorentzian line profile with a FWHM determined by the decay rate γ of the excited state.

2.2.3. Two-photon absorption selection rules

The selection rules for two-photon absorption are obtained by analyzing the matrix elements β_{eg}, given by equation (2.15). Applying the Wigner-Eckart theorem β_{eg} can be expressed in terms of a $3j$ symbol and a reduced matrix element

$$\beta_{eg}^2 = \frac{1}{4\hbar^2 h^2 c^2 \varepsilon_0^2} \left| \sum_{n,m_{J_n}} (-1)^{J'+J_n-(m'_J+m_{J_n})} \langle eJ'||D||J_n n\rangle \langle nJ_n||D||Jg\rangle \right.$$
$$\times \sum_{\mu,\nu=-1}^{1} \left[\frac{\epsilon_{1,-\mu}\,\epsilon_{2,-\nu}}{\omega_{ng}-\omega_2} \begin{pmatrix} J' & 1 & J_n \\ -m'_J & \mu & m_{J_n} \end{pmatrix} \begin{pmatrix} J_n & 1 & J \\ -m_{J_n} & \nu & m_J \end{pmatrix} \right.$$
$$\left. \left. + \frac{\epsilon_{2,-\nu}\,\epsilon_{1,-\mu}}{\omega_{ng}-\omega_1} \begin{pmatrix} J' & 1 & J_n \\ -m'_J & \nu & m_{J_n} \end{pmatrix} \begin{pmatrix} J_n & 1 & J \\ -m_{J_n} & \mu & m_J \end{pmatrix} \right] \right|^2 . \quad (2.23)$$

This relation is nonzero if the Wigner $3j$ symbols $\left(\begin{smallmatrix} J_1 & J_2 & J_3 \\ m_1 & m_2 & m_3 \end{smallmatrix}\right)$ satisfy the following conditions:

1. triangle relation:
   $J_1 - J_2 \leq J_3\,, \qquad J_2 - J_3 \leq J_1\,, \qquad J_3 - J_1 \leq J_2$
2. magnetic quantum numbers sum to zero:
   $m_1 + m_2 + m_3 = 0$
3. $J_1 + J_2 + J_3 =$ integer

The $3j$ symbols can be calculated using the Racah formula [16] providing the selection rules for the two-photon absorption summarized in table 2.1 [17]. The selection rules for hyperfine transitions are obtained by substituting J and m_J in equation (2.23) and table 2.1 by F and m_F respectively.

2.3. Chirp investigation

In section 2.2 the pulses were assumed to be bandwidth limited. In general, however, short pulses can acquire a temporal and spectral phase resulting in a spectral and temporal broadening. Figure 2.4 shows the electric field of a linearly up-chirped pulse, i.e. the

Table 2.1.: *Two-photon selection rules for the total angular momentum J. Transitions which satisfy the general selection rule are allowed, excluding the forbidden transitions for particular polarizations. For a forbidden transition the condition for ΔJ as well as for Δm_J must be satisfied simultaneously.*

general selection rules			
$\Delta J = 0, \pm 1, \pm 2$		same parity	$J' + J$: integer
particular polarization rules			
polarization			
ω_1	ω_2	forbidden transitions	
σ^+	σ^-		$\Delta m_J \neq 0$
σ^+	π	ΔJ: $0 \to 0$	$\Delta m_J \neq -1$
σ^-	π	ΔJ: $0 \to 0$	$\Delta m_J \neq 1$
π	σ	ΔJ: $0 \to 0$	$\Delta m_J \neq \pm 1$
π	π	ΔJ: $0 \leftrightarrow 1$	$\Delta m_J \neq 0$
σ^+	σ^+	ΔJ: $0 \leftrightarrow 1$, $0 \leftrightarrow 0$, $1/2 \leftrightarrow 1/2$	$\Delta m_J \neq -2$
σ^-	σ^-	ΔJ: $0 \leftrightarrow 1$, $0 \leftrightarrow 0$, $1/2 \leftrightarrow 1/2$	$\Delta m_J \neq 2$
additional rules for photons of equal frequency			
$J: \ 0 \to 1$ $\Delta J = \pm 1, \quad m_J: \ 0 \to 0$		} forbidden for all polarizations	

instantaneous frequency rises linearly with time. The temporal chirp broadens the spectrum of the pulse. Group velocity dispersion (GVD) leads to a spectral phase and thus a temporal broadening of the pulses. A GVD of e.g. 35 fs^2/mm of fused silica at 800 nm doubles the initial pulse length of 10 fs after around 2 mm of material. However, to double the pulse duration of initially 1 ps long pulses, around 18 m of fused silica is necessary.

Defining an additional temporal and spectral phase with the chirp parameters p_1 and p_2 the complex temporal and spectral pulse envelopes can be written in the form

$$\tilde{\mathcal{E}}(t) = \left(\frac{2p_1}{\pi}\right)^{1/4} \frac{E_0}{\sqrt{\tau}} \exp\left[-(p_1 + ip_2)\,\frac{(t \pm z/c)^2}{\tau^2}\right], \tag{2.24a}$$

$$\tilde{\mathcal{E}}(\omega) = \left(\frac{p_1}{2\pi}\right)^{1/4} E_0 \sqrt{\frac{\tau}{p_1 + ip_2}} \exp\left[-\frac{p_1(\omega\tau)^2}{4(p_1^2 + p_2^2)} + \frac{ip_2(\omega\tau)^2}{4(p_1^2 + p_2^2)} \pm \frac{i\omega z}{c}\right]. \tag{2.24b}$$

The envelopes are normalized such that the pulse energy is independent of τ and the chirp parameters p_1 and p_2. Setting $p_1 = 1$ and $p_2 = 0$ Fourier limited pulses with a TBP given by equation (2.18) are obtained. The phase factor $(p_1 + ip_2)$ accounts for

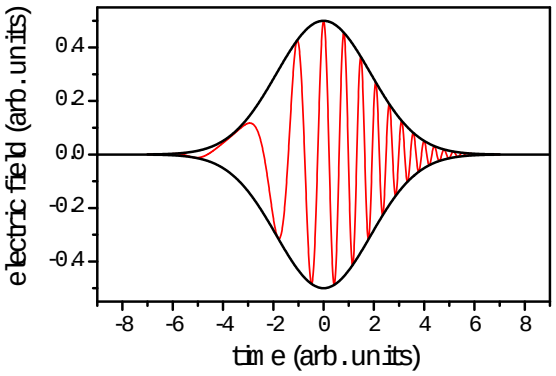

Figure 2.4.: Electric field of an up-chirped pulse. The instantaneous frequency increases with time.

both the temporal and spectral broadening effects so the intensity FWHM in the time and frequency domain for chirped pulses can be written:

$$\Delta t = \tau\sqrt{\frac{2\ln(2)}{p_1}}\,, \qquad \Delta\nu = \frac{1}{\pi\tau}\sqrt{2\ln(2)p_1\left(1+\frac{p_2^2}{p_1^2}\right)}\,, \tag{2.25}$$

$$\Delta t\,\Delta\nu = \frac{2\ln(2)}{\pi}\sqrt{1+\left(\frac{p_2}{p_1}\right)^2}\,. \tag{2.26}$$

It can be seen in equation (2.25) that pure spectral broadening occurs for $p_1 = 1$, whereas for pure temporal broadening $p_2^2 = p_2(1-p_1)$ must hold. Substituting the electric fields in equation (2.20) by $\tilde{E}_{1,2}(t,z) = E_{01,02}\sqrt{\omega_\mathrm{r}}\sum_m \tilde{\mathcal{E}}(m\omega_\mathrm{r})\exp\left[-i(\omega_0+m\omega_\mathrm{r})t\right]$, with the field amplitude of mode m as defined in equation (2.24b) ($\omega \to m\omega_\mathrm{r}$), keeping only the resonant terms and approximating the sum over the mode number m by an integral yields the two-photon transition rate with chirped pulses

$$\mathfrak{R}_{ge}^{\mathrm{chirp}} = 4(2\pi\beta_{eg})^2\mathcal{I}_1\mathcal{I}_2\frac{\gamma}{\Delta\omega_{eg}^2+\gamma^2/4}\,\frac{2\ln(2)}{\pi}\,\frac{1}{\Delta t\,\Delta\nu}\,\exp\left[-\frac{4z^2}{(c\tau)^2}\right]. \tag{2.27}$$

A comparison of this result with equation (2.22) shows that a chirp leads to an extra factor that depends on the TBP and cause the transition rate to decay with $(\Delta t\,\Delta\nu)^{-1}$. For unchirped pulses this factor reduces to 1 yielding the maximum two-photon transition rate given by equation (2.22). A further important feature is that within this model neither the line shape nor the line position is affected by the chirp. In addition the AC Stark shift, which is calculated by analyzing the matrix element, does not change upon spectroscopy with chirped pulses.

2.4. Detuning of spectral envelope

So far it was explicitly assumed that the spectral pulse envelope is centered around $\omega_{eg}/2$ (see upper plot in figure 2.5). In this case two photons from the central mode excite

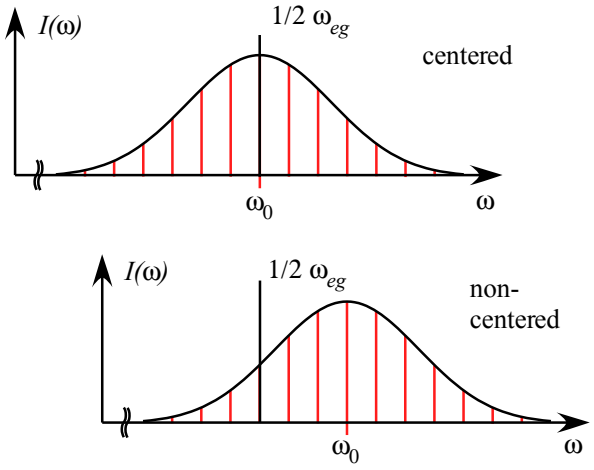

Figure 2.5.: Demonstration of a centered (upper plot) and a non-centered (lower plot) spectral envelope.

the transition. The mode number m and m' count the comb modes with respect to the carrier so only the modes with $m = -m'$ are resonant and add up pairwise as described in section 2.1.2. In general, however, the central comb mode ω_0 may be shifted with respect to the half of the transition frequency (lower plot in figure 2.5). In this case two photons from the mth mode excite the transition and the mode sum $m + m' = \mu \neq 0$, in contrast to a perfectly centered comb. Substituting $m' = \mu - m$ in equation (2.20), rearranging the terms and approximating the sum over m by an integral results in

$$\Re_{ge}^{\mathrm{det}} = \Re_{ge}^{\mathrm{comb}} \times \exp\left[-\frac{1}{2}(\tau\mu\omega_r)^2\right], \tag{2.28}$$

with $\Re_{eg}^{\mathrm{comb}}$ as given by equation (2.22). This result shows that a detuning of the spectral envelope introduces an additional factor which cause the transition rate to decrease exponentially with μ^2. For zero detuning ($\mu = 0$) the maximum transition rate is obtained.

3. Experimental setup and test of the laser system

This chapter provides a detailed description of the design and performance of the laser system used for the experiments presented in this thesis. It is capable of generating frequency combs at around 820, 410 and 205 nm wavelength. The latter can be used to drive the $1S - 3S$ two-photon transition in hydrogen. The discussion includes requirements on the laser system, design and characteristics of the laser system and UV-degradation of mirrors and the crystal in the final conversion stage.

3.1. Requirements on the laser system

A straightforward way to build up a laser source in the DUV wavelength region is by frequency quadrupling e.g. the output of a mode-locked Ti:sapphire laser in two SHG stages. In contrast to e.g. sum frequency generation where two waves at different frequencies are mixed to generate a third wave, in SHG two photons of same frequency are converted to one photon at the SH. Therefore, to increase the efficiency of the conversion process an enhancement resonator at the fundamental wavelength can easily be implemented for resonant SHG. Utilizing resonant SHG, a shorter nonlinear crystal (e.g. 5 mm instead of a 10 mm long crystal) can be used with no or a small loss of output power, in contrast to the longer crystal, but a greatly improved beam profile due to reduced spatial walk-off. Using a short crystal also the temporal walk-off is reduced providing a broader acceptance bandwidth. The limit of nonlinear mixing is set by the phase matching condition and transparency range of nonlinear crystals. The shortest wavelength reachable by SHG in a BBO crystal is around 204.7 nm.

The actual design of the laser setup should meet the following conditions:

- Output power. Two-photon spectroscopy requires in general rather high average intensity compared to dipole allowed transitions. Unfavorable effects as e.g. residual chirp and non-centered spectral pulse envelope can further reduce the signal. Monte Carlo simulations, presented later in this thesis, show that power levels exceeding 10 mW are necessary to achieve an appreciable rate.

- Repetition rate. High resolution DFCS is only possible provided that the repetition frequency exceeds the natural linewidth of the excited state, $\omega_r > \gamma$. Transitions with several MHz natural line widths require thus high repetition laser systems.

- Pulse length. Nonlinear conversion requires high peak intensity of the laser to drive the process efficiently. The peak intensity of a pulsed laser is by orders of magnitude higher than its average intensity. Hence short pulses make the nonlinear conversion appreciable efficient. However, for frequency conversion of fs pulses and below group velocity mismatch limits the effective interaction length and thus the conversion efficiency.

- Transform limited pulses. Short pulses easily acquire a chirp while propagating through a medium. As discussed in section 2.3, in DFCS with chirped pulses the transition rate decreases according to equation (2.27) with increasing TBP.

- Beam profile. Enhancement resonators are used for the UV light generation and spectroscopy. To achieve a high coupling efficiency into these resonators an adequate beam profile is necessary.

- Stabilization. For absolute frequency determination the laser must be carefully stabilized. The natural linewidth of the transition and experimental conditions, as e.g. the interaction volume, set an upper limit on the width of a comb mode.

3.2. Design of the system

The laser system shown in figure 3.1 may be divided into three parts: stabilized and referenced fundamental laser, first resonant SHG stage and second resonant SHG stage. The fundamental laser is a commercial actively mode-locked ps Ti:sapphire laser (Spectra Physics, Tsunami) which is pumped by a frequency doubled, diode-pumped Nd:vanadate laser (Coherent, Verdi V10/V18). The resonant SHG cavities are both 6-mirror ring resonators, whose free spectral range is matched to the pulse repetition rate. In the following the three parts are described in detail.

3.2.1. Titanium:sapphire laser

The tunable Ti:sapphire laser is adjusted to emit ps pulses at 820 nm with a repetition frequency of around 82 MHz. To analyze, stabilize and reference the laser a small amount of the output power (10 %) is branched off. An optical spectrum analyzer (OSA) monitors the spectral envelope and is used for its alignment with respect to the transition frequency while an autocorrelator (AC) provides a measure for the pulse duration.

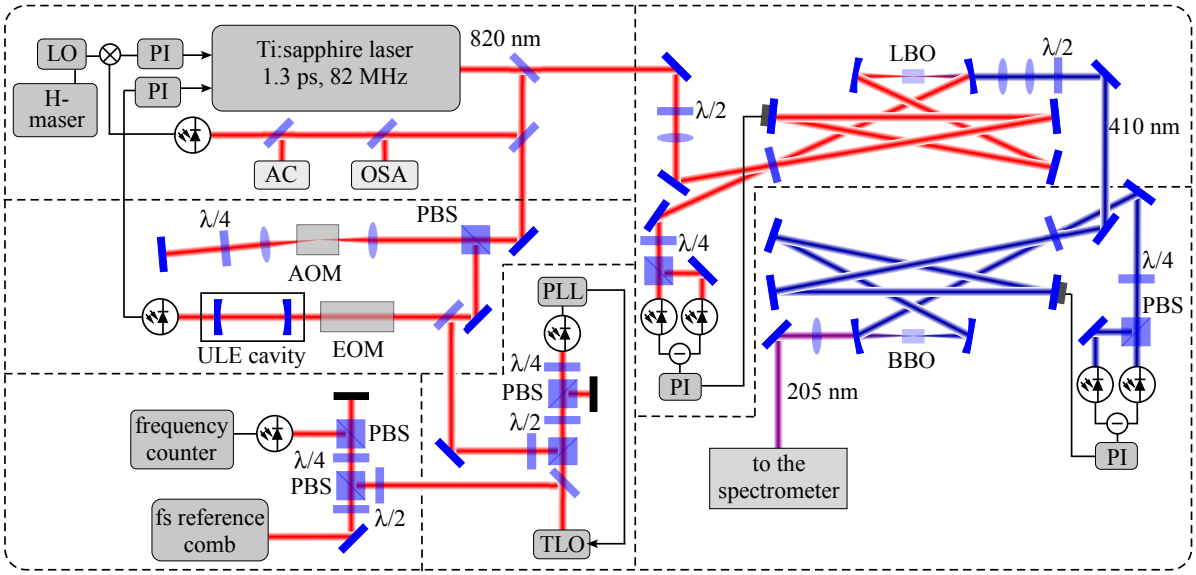

Figure 3.1.: *Experimental setup for deep UV frequency comb generation. DPD: difference photo diode; EOM: electro optic modulator; AOM: acousto optic modulator; ULE: ultra-low-expansion glass; PI: proportional-integral controller; TLO: Transfer laser oscillator; LO: local oscillator; PBS: polarizing beam splitter; OSA: optical spectrum analyzer; AC: autocorrelator.*

In order to stabilize the laser, both the carrier ω_0 and the repetition rate ω_r must be locked. This can be done by controlling the length and the dispersion of the laser cavity [18]. The Tsunami was modified with a linear translation stage for coarse length tuning and a piezo actuator for fast control while the built-in Gires-Tournois interferometer (GTI) was used for dispersion control.

The repetition frequency was measured with a fast photo diode and stabilized to a synthesizer. For this purpose the signal of the photo diode was mixed with a radio frequency from the synthesizer, which was referenced to a 10 MHz signal coming from a hydrogen maser. The generated error signal was fed back to the built-in GTI in the Ti:sapphire laser.

To stabilize the carrier, the modes of the Ti:sapphire laser were servo locked to an external reference cavity which is well isolated from acoustics and temperature variations [19]. The required error signal was generated with the Pound-Drever-Hall method [20] and fed back on the piezo driven folding mirror of the laser. The free spectral range of the reference cavity is matched to the pulse repetition rate such that it is an integer ratio of 1:10, i.e. every 10th mode of the incoming spectrum is transmitted by the reference cavity, reducing its finesse by a factor of 10 to $\mathcal{F} \approx 300$. This moderate finesse of the reference resonator allows to stabilize the repetition frequency without impairing the lock of the Ti:sapphire laser to the reference resonator.

An acousto-optic modulator (AOM) in double pass configuration in front of the reference resonator (s. figure 3.1) allows to tune the laser in frequency while it is locked.

For absolute frequency determination the frequency of a single comb mode is measured using a reference fs frequency comb. For this purpose a cw transfer laser oscillator (TLO), which is a laser diode running at around 820 nm, is phase-locked to a mode of the Ti:sapphire laser and the heterodyne signal between the TLO and a mode of the reference fs comb is continuously measured. Based on this measurement the frequencies of all the other comb modes of the Ti:sapphire laser can be calculated with high precision.

3.2.2. Conversion efficiency calculation

For a proper choice of nonlinear crystals and characterization of the resonant SHG stages in the subsequent sections, relations to calculate SHG conversion efficiencies are derived in this section. By resonant SHG generation with short pulses pump depletion is easily achieved. Therefore the final result provides expressions for the conversion efficiency in the non-depleted and depleted pump regime. These expressions also account for temporal and spatial walk-off as well as for focusing effects.

Interactions between electro magnetic fields and materials are described by the Maxwell equations. Based on these equations a reduced wave equation for a linearly polarized electric field propagating as a plane wave in the z-direction can be written:

$$\left(\frac{\partial^2}{\partial z^2} - \frac{\mathfrak{n}^2}{c^2}\frac{\partial^2}{\partial t^2}\right) E(t,z) = \frac{1}{c^2\varepsilon_0}\frac{\partial^2}{\partial t^2} P_{NL}(t,z)\,, \tag{3.1}$$

with a refractive index $\mathfrak{n}$ and nonlinear polarization $P_{LN}(t,z)$. The crucial parameter for nonlinear mixing is the nonzero source term on the right hand side which is responsible for the generation of new frequencies. The second order nonlinear polarization $P_{LN}(t,z)$ can be written as [21]

$$P_{NL}(t,z) = \varepsilon_0 \chi^{(2)} E(t,z)^2\,,$$

where $\chi^{(2)}$ is the second order dipole susceptibility tensor. If the polarization of the incident and generated field is known $\chi^{(2)}$ can be treated as a scalar and is twice the effective nonlinearity $\chi^{(2)} = 2d_{\text{eff}}$. Restricting the following calculations to SHG the electric field of the optical waves propagating in the z-direction inside a nonlinear crystal can be written as a superposition of the incident $E_1(t,z)$ and generated $E_2(t,z)$ beam $E(t,z) = E_1(t,z) + E_2(t,z)$. Inserting this total field in equation (3.1), equating the coefficients and applying the slowly varying envelope approximation (SVEA) results in two coupled partial differential equations for the envelope functions $\mathcal{E}_1(t,z)$ and $\mathcal{E}_2(t,z)$. For a pulsed electric field substitute $\mathfrak{n}_{1,2}/c \to 1/v_{1,2} = (\mathfrak{n}_{1,2}/c) + (\omega_{1,2}/c)(\mathrm{d}\mathfrak{n}_{1,2}/\mathrm{d}\omega_{1,2})$, where $\mathfrak{n}_1$ and $\mathfrak{n}_2$ are the refractive indices of the material for the fundamental (F) and second harmonic (SH) beam and v_1, v_2, ω_1 and ω_2 the group velocities and the angular frequencies of the F and SH wave respectively.

For small conversion efficiencies the fundamental pulses travel without loss in a frame moving with the group velocity v_1 and their envelope at any position z is given by $\mathcal{E}_1(t - z/v_1)$ resulting in a SH envelope function

$$\mathcal{E}_2\left(t - \frac{L}{v_2}, L\right) = -i\,\frac{\chi^{(2)}\omega_2^2}{4c^2k_2}\int_0^L \mathcal{E}_1^2\left(t - \frac{z}{v_2} + \left(\frac{1}{v_2} - \frac{1}{v_1}\right)z\right)e^{-i\Delta k z}\mathrm{d}z\,, \tag{3.2}$$

where L is the crystal length and $\Delta k = 2k_1 - k_2$ the phase mismatch. Transformation into the frequency domain and integration with respect to the propagation direction yields the second harmonic spectral intensity (eq. (3.107) in ref. [21])

$$\mathcal{I}_2(\omega', L) = \frac{4\pi\mathfrak{n}_1}{c\varepsilon_0\mathfrak{n}_2^2}\left(\frac{\chi^{(2)}\omega_2^2 L}{4c^2k_2}\right)^2 \mathrm{sinc}^2\left\{\left[\left(\frac{1}{v_2} - \frac{1}{v_1}\right)\omega' - \Delta k\right]\frac{L}{2}\right\} \times \mathcal{I}_1^2(\omega')\,. \tag{3.3}$$

Here $I_1(\omega')$ is the spectral intensity of the fundamental wave with the detuning ω' from the carrier frequency, for which proper phase matching (i.e. $\Delta k = 0$) can be assumed. The term $(v_2^{-1} - v_1^{-1})z$ in equation (3.2) describes a separation of the fundamental and SH pulses (temporal walk-off) upon propagation due to the group velocity mismatch (GVM). After traveling the characteristic length L_{GVM} defined as

$$L_{\mathrm{GVM}} = \Delta t_1\left(\frac{1}{v_2} - \frac{1}{v_1}\right)^{-1}\,, \tag{3.4}$$

with Δt_1 the FWHM of the fundamental pulse, the F and SH pulses are completely separated. In the frequency domain this corresponds to a spectral filtering that limits the phase matching bandwidth. The temporal walk-off causes a broadening of the SH pulses accompanied by a spectral narrowing such that the TBP is not affected by GVM for Fourier limited fundamental pulses. For a crystal length shorter than the characteristic length $L << L_{\mathrm{GVM}}$ and $\Delta k = 0$ the temporal walk-off can be neglected and the temporal pulse envelope is simply squared, giving rise to a pulse narrowing by $\sqrt{2}$ for Gaussian and by a factor of 1.45 for sech^2 pulses. If $L >> L_{\mathrm{GVM}}$, the spectral bandwidth of the incident pulses exceeds the acceptance bandwidth and the spectrum is filtered by the sinc^2-function. In this case the second harmonic pulse duration is determined by the GVM and approaches the value $L \cdot |v_2^{-1} - v_1^{-1}|$.

In this simple approach only GVM and phase mismatch are included, which is sufficient in some cases. To give more accurate predictions for the conversion efficiency and output beam profile, focusing effects, that depend on the confocal parameter b, and spatial walk-off, depending on the walk-off angle δ and the beam waist radius w_0, must be included in the calculations. To estimate their significance, let's define the characteristic lengths [22]

$$L_f = \frac{\pi\, b}{2}\,, \tag{3.5}$$

$$L_\delta = \sqrt{\pi}\,\frac{w_0}{\delta}\,. \tag{3.6}$$

A detailed theoretical description of SHG including these effects in the low conversion efficiency regime was developed by G. D. Boyd and D. A. Kleinman [22]. Their approach was extended by H. Wang and A. M. Weiner for pulsed laser sources, where temporal walk-off is a serious limiting effect, providing an expression for the conversion efficiency in the non-depleted pump regime η_{nd} including spatial and temporal walk-off as well as focusing effects [23]

$$\eta_{\mathrm{nd}} = \frac{\mathcal{W}_2(L)}{\mathcal{W}_1(0)} = \mathcal{W}_1(0)\mathcal{H}(L) = \mathcal{W}_1(0)\sqrt{\frac{2\ln(2)}{\pi}}\,\frac{4\omega_1^2 d_{\mathrm{eff}}^2 L}{\mathfrak{n}_1\mathfrak{n}_2 c^3\varepsilon_0\lambda_1\Delta t_1}\,h(A,B,\xi)\,, \tag{3.7}$$

$$h(A,B,\xi) = \frac{1}{4\xi}\iint_{-\xi}^{\xi}\frac{\exp\left[i\frac{1}{2}\Delta k b(\xi_1'-\xi_2') - \frac{(4\xi B^2+A^2)}{4\xi^2}(\xi_1'-\xi_2')^2\right]}{(1-i\xi_1')(1+i\xi_2')}\,\mathrm{d}\xi_1'\mathrm{d}\xi_2'\,,$$

where $\mathcal{W}_1$ and $\mathcal{W}_2$ are the F and SH pulse energies, $\xi = L/b$ the focusing parameter, parameters $A = L/L_{\mathrm{GVM}}$ and $B = \delta\sqrt{k_1 L}/2$ represent the temporal and spatial walk-off respectively and $\xi_{1,2}' = (2z_{1,2}/b) - \xi$. In Figure 3.2 function $h(A,B,\xi)$ is plotted for $\Delta k = 0$ and $A = 1$, $B = 1,2,4,8$ (left plot) and $A = 6$, $B = 1,2,4,8$ (right plot).

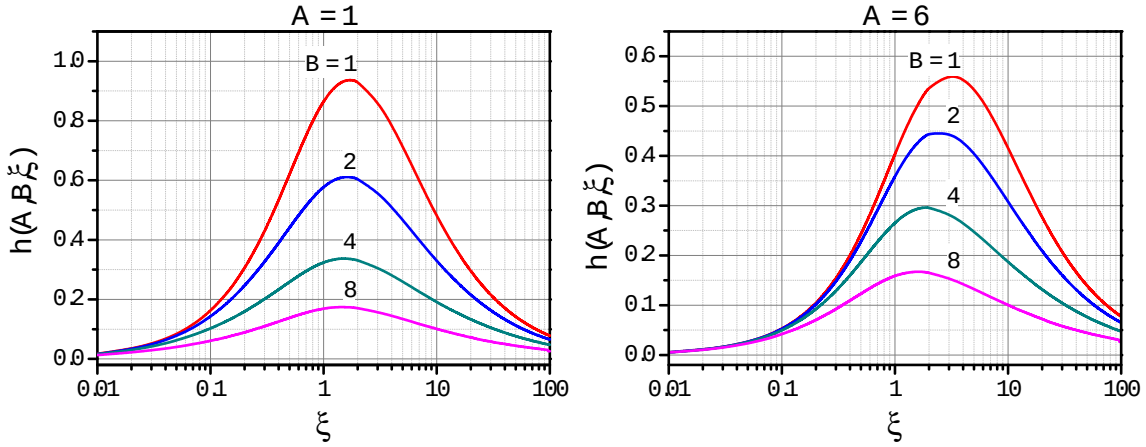

Figure 3.2.: *$h(A,B,\xi)$ plotted as a function of the focusing parameter ξ for $\Delta k = 0$ and $A = 1$, $B = 1,2,4,8$ (left plot) and $A = 6$, $B = 1,2,4,8$ (right plot).*

Based on this result an approximate expression for the conversion efficiency including fundamental wave depletion can be derived. Sub-dividing the nonlinear crystal in small segments the second harmonic and fundamental energy change in such a segment can be written as

$$\frac{\mathrm{d}\mathcal{W}_2}{\mathrm{d}z} = \mathcal{W}_1^2\,\mathcal{H}'(z)\,, \tag{3.8a}$$

$$-\frac{\mathrm{d}\mathcal{W}_1}{\mathrm{d}z} = \frac{\mathcal{W}_2}{\mathrm{d}z}\,. \tag{3.8b}$$

Solving this set of differential equations finally results in the conversion efficiency η_d including pump depletion [23]

$$\eta_\mathrm{d} = 1 - \frac{1}{1+\eta_\mathrm{nd}}\,. \tag{3.9}$$

The validity of this approximation was checked using a numerical model provided by the SNLO software (Sandia National Laboratories, v51), which is based upon integration of the Maxwell equations using a split-step FFT method [24]. This model is able to simulate single pass short pulse mixing of Gaussian beams including all the limiting effects and accounting for the boundary conditions of every slab $\mathrm{d}z$. As will be shown in the next sections, equation (3.9) overestimates the efficiency compared to the numerical model. That may be explained by reshaping effects which are not included in the calculations above. Due to the nonlinear nature of the second harmonic generation process the central part of a pulse with higher intensity will be depleted stronger than the less intense pulse wings. This results in a spatial and temporal beam reshaping of the fundamental and SH pulses. The beam reshaping at the boundaries is much slower for lower effective nonlinearity of the crystal providing more accurate results in this case even at higher intensities of the fundamental beam.

For the actual experimental parameters equation (3.9) provides a good approximation for the conversion efficiencies.

3.2.3. First resonant second harmonic generation stage

For SHG of the mode-locked ps Ti:sapphire laser described in section 3.2.1, its output is mode matched into an enhancement cavity. In order to achieve a high conversion efficiency while maintaining an acceptable beam profile of the SH beam, an appropriate nonlinear crystal is chosen. In this section first the choice of the nonlinear crystal is discussed followed by a description of the resonant SHG cavity.

Chrystal choice

Resonant SHG of a tunable cw as well as a mode-locked Ti:sapphire laser around 820 nm using lithium triborate LiB_3O_5 (LBO) [25–27] and lithium iodate $LiIO_3$ [28, 29] was already reported in the early 90s. A third nonlinear crystal suitable for this process is β-barium borate BaB_2O_4 (BBO) [30]. An overview of some parameters for the crystals is given in table 3.1. All three of them have good transparency down into the UV wavelength region and high damage threshold compared to the estimated 3 mJ/cm^2 pulse energy inside the enhancement resonator. While $LiIO_3$ has the highest nonlinear coefficient, 1.7 times higher than BBO and 4.5 times higher than LBO, LBO shows the lowest walk-off angle and dispersion, promising a much better output beam profile.

Accounting for spatial and temporal walk-off and pump depletion the SHG process might be optimized with respect to the waist radius w_0 for a given crystal length L. In

Table 3.1.: *Overview of the parameters for LBO, BBO and $LiIO_3$, suitable for type I SHG around 820 nm [31]. Also listed are the corresponding calculated characteristic lengths and single pass conversion efficiencies for $L = 10$ mm.*

820 nm (o) + 820 nm (o) = 410 nm (e)			
	LBO	BBO	$LiIO_3$
refractive index $\mathfrak{n}$	1.610	1.660	1.866
group velocity index $\mathfrak{n}_{g,1}$ / $\mathfrak{n}_{g,2}$	1.631 / 1.665	1.683 / 1.737	1.911 / 2.067
walk-off δ [mrad]	15.59	66.78	86.54
phase matching angle [deg]	29.5	28.5	41.1
d_{eff} [pm/V]	0.763	2.0	3.46
transparency range [nm]	$160 - 2600$	$185 - 2600$	$300 - 6000$
damage threshold [J/cm^2] for 10 ns pulses @ 1064 nm	~ 25	~ 13	~ 1
characteristic lengths and conversion efficiency as defined in section 3.2.2			
L_{GVM} [mm]$^{(1)}$	11.5	7.2	2.5
L_δ [mm]$^{(2)}$	3.1	0.75	0.57
$\eta^{(3)}$	35 %	47 %	60 %
$\eta_{SNLO}{}^{(4)}$	34 %	44 %	54 %

(1) calculated using equation (3.4) with $\Delta t_1 = \Delta t_\omega = 1.3$ ps

(2) calculated using equation (3.6) with $w_0 = 28$ μm

(3) calculated using equation (3.9) with $w_0 = 28$ μm, $\Delta k = 0$ and $\mathcal{P} = 1.6$ W average power in front of the resonator

(4) $\eta_{SNLO} = \mathcal{W}_2/\mathcal{W}_1$, calculated using SNLO software, same parameters as in (3)

figure 3.3 the single pass conversion efficiencies calculated using equation (3.9) and, as a validity check, simulated using the SNLO software are plotted as functions of the waist radius for 10 mm long nonlinear crystals listed in table 3.1. As discussed in the previous section the theoretical model in equation (3.7) overestimates the conversion efficiency. The deviation between the theoretical model and numerical calculation becomes stronger for high pulse energies and effective nonlinearity [23], consequently it is smaller for LBO and stronger for $LiIO_3$, due to the higher nonlinearity of the latter. Indeed figure 3.3 reflects this behavior. For $LiIO_3$ the deviation amounts to 11 % while for LBO it is only ≈ 3 % so equation (3.9) provides a good approximation for the conversion efficiency here.

Despite its lower nonlinearity and expected conversion efficiency, LBO is chosen for SHG of 820 nm because of its lower temporal and spatial walk-off. While GVM merely

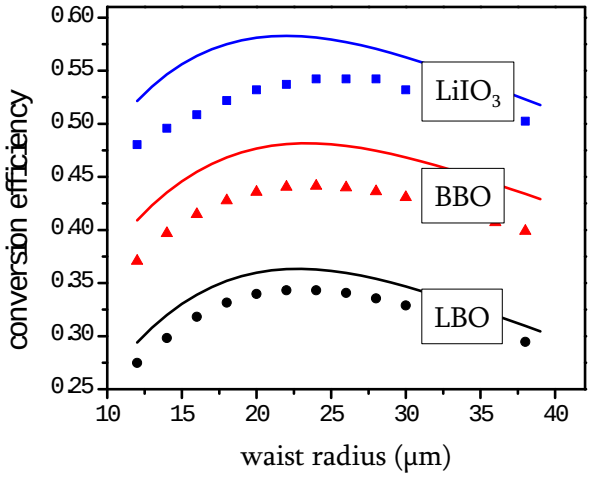

Figure 3.3.: *Calculated single pass conversion efficiency as a function of the waist radius w_0 in a 10 mm long LBO (black), BBO (red) and $LiIO_3$ (blue) crystal respectively. The solid lines show the conversion efficiency calculated using equation (3.9) and the data represented by the symbols are obtained by the numerical model provided by the SNLO software. In both approaches birefringence, focusing and pump depletion are included and absorption, group velocity dispersion, chirp and Fresnel losses are neglected.*

broadens the pulses, a strong spatial walk-off causes an elliptical output beam profile which can only be partially compensated.

Resonant SHG cavity

A Brewster cut LBO crystal with $\theta = 90°$ and $\phi = 29.6°$ for type I phase matching is used in the first conversion stage for SHG at 410 nm. G. D. Boyd and D. A. Kleinman found an optimum ratio between the crystal length L and the confocal parameter b which is $\xi = L/b = 2.84$ [22]. However this optimum applies only for negligible temporal and spatial walk-off ($A = B \approx 0$). For actual experimental parameters, however, $A = 1$ and $B = 2$ resulting in an optimum focusing parameter of $\xi = 1.6$ (see left plot in figure 3.2). For a given confocal parameter of e.g. $b = 6$ mm ($w_0 = 28$ μm) the optimum crystal length is around 10 mm. This exceeds the characteristic length for spatial walk-off L_δ (see table 3.1) and will result in an elliptical output beam profile. The effect of GVM, however, will be very small. Using a shorter crystal, e.g. 5 mm, will greatly improve the output beam profile but the SH power will drop due to a reduced conversion efficiency. To compensate for the lower efficiency the crystal is placed in an enhancement cavity for resonant SHG. In this way conversion efficiencies of more than 50 % can be achieved with short crystals while maintaining a good output beam profile.

A LBO crystal is placed in an astigmatism compensated ring enhancement cavity [32] for resonant second harmonic generation (figure 3.1). To protect the crystal from moisture it is held in an aluminum mount which is temperature stabilized at 45(1)°C and allows to purge the crystal with dry oxygen.

The ring design allows for an easy separation of the incoming and the reflected beam. The latter is used to generate an error signal following the polarization method [33] for

electronic feedback on a piezo-mounted folding mirror in order to stabilize the cavity length. The resonators round trip length needs to be set properly to match the pulse repetition rate of 82 MHz of the Ti:sapphire laser corresponding to a resonator length of 3.66 m. Two focusing mirrors with 200 mm radius of curvature generate an almost spherical focus of 28 μm waist radius at the center of the crystal. The focusing mirrors are coated to be high reflective (HR, $\mathcal{R} > 99.9$ %) at the fundamental and high transmissive (HT, $\mathcal{T} > 90$ %) at the second harmonic wavelength. The plane folding mirrors (HR, $\mathcal{R} > 99.9$ %), used to match the cavity length to the pulse repetition rate, are arranged to allow full folding angles of $\phi = 16°$ on the focusing mirrors for compensation of the astigmatism caused by the Brewster cut nonlinear crystal [32]. For proper impedance matching the reflectivity of the input coupler (IC) $\mathcal{R}_{\mathrm{IC}}$ has to be chosen such that it compensates the round trip losses $(1 - \mathcal{V})$ of the resonator. These losses arise from absorption, transmission, and scattering of the high reflective mirrors, absorption by the medium inside the cavity, and conversion into the second harmonic, while the latter is the desired process. The efficiency of SHG is power dependent so the conversion losses are power dependent and therefore depend on the enhancement U given by

$$U = \frac{1 - \mathcal{R}_{\mathrm{IC}}}{(1 - \sqrt{\mathcal{V}\mathcal{R}_{\mathrm{IC}}})^2}\,, \tag{3.10}$$

which itself depends on $\mathcal{V}$ and is maximum for $\mathcal{R}_{\mathrm{IC}} = \mathcal{V}$. Neglecting other than conversion losses, what is a good approximation for our power levels, we can set $1 - \mathcal{V} = 1 - \mathcal{R}_{\mathrm{IC}} = \eta_d$ where η_d is defined by equation (3.9). Substituting η_{nd} in equation (3.9) by $(1 - \mathcal{R}_{\mathrm{IC}})^{-1}\eta_{nd}$, to take the enhancement dependence of the conversion efficiency into account, yields finally

$$\frac{1}{\mathcal{R}_{\mathrm{IC}}} = 1 + \frac{1}{1 - \mathcal{R}_{\mathrm{IC}}}\,\eta_{nd}\,, \tag{3.11}$$

where η_{nd} is the single pass conversion efficiency in the non depleted pump regime given by equation (3.7). With an average input power of $\mathcal{P}_1 = 1.6$ W in front of the cavity an optimal input coupler reflectivity is calculated to be $\mathcal{R}_{\mathrm{IC}} = 49$ %. For a perfectly impedance matched resonator $\eta_d = \mathcal{P}_2/(U\mathcal{P}_1) = 1 - \mathcal{R}_{\mathrm{IC}}$ amounts to 51 % and therefore the resonant conversion efficiency defined by $\eta = \mathcal{P}_2/\mathcal{P}_1 = \eta_d/(1 - R_{\mathrm{IC}})$ is equal 1, as expected for a perfectly impedance matched cavity with no losses other than conversion losses.

In these calculations scattering and absorption of the mirrors as well as Fresnel losses at the input and output surfaces and linear and nonlinear absorption of the crystal are not included. Measuring the single pass conversion efficiency provides a more reliable value of 16 % for given experimental parameters. The resulting optimum input coupler is calculated to have 67 % reflectivity. For an input coupler at hand with $\mathcal{R}_{\mathrm{IC}} = 75$ % the theoretical resonant conversion efficiency is calculated to be $\eta = 98$ %. To optimize the impedance matching and for more flexible operation the input coupler is replaced

by a recently bought gradient input coupler (GOC) with a reflectivity of 75 ± 10 %. The reflectivity of such a mirror is maximum (85 %) on one edge and decreases across the substrate to 65 % on the other edge.

3.2.4. Second resonant second harmonic generation stage

In this section the final conversion stage capable of generating a frequency comb at 205 nm is presented. The discussions include the crystal choice and design of the resonator.

Crystal choice

There are three nonlinear crystals reported that are suitable for SHG at 205 nm, BBO, $KBe_2BO_3F_2$ (KBBF) [34] and $Sr_2Be_2B_2O_7$ (SBBO) [35]. All three of them are transparent down to 190 nm and have comparable effective nonlinearities for SHG at 205 nm. While the phase matching angle for SHG at 205 nm in BBO ($\theta = 86.4°$) is unfavorably close to the SHG cut off (90°), KBBF and SBBO seem promising because of their lower cut off wavelength for this process.

Due to its layered structure along the phase matching direction the KBBF crystal is rather fragile and the growth of a bulk crystal is very difficult [34]. The thin plate-like crystals cannot be cut along the phase matching direction and have to be tilted for proper phase matching. As a consequence of this technique the phase matching cut off is inaccessible and the tilt gives rise to high Fresnel losses at the crystal faces. Using a prism-coupling technique phase matching close to the cut-off wavelength becomes possible while the Fresnel losses are reduced [34, 36], but absorption losses inside the prisms reduce the performance. However, SHG at a wavelength as low as 177.3 nm was demonstrated experimentally using a KBBF crystal in combination with a prism-coupling technique.

The SBBO crystal was developed to solve the problem with the layered structure of KBBF but maintains its advantages. However, it is so far unexplored concerning the phase matching angles and nonlinear coefficients, so no data is available for this crystal. In addition SBBO is currently not commercially available. In table 3.2 some of the parameters of BBO and KBBF are listed, including the relevant calculated characteristic lengths and the theoretical conversion efficiencies. Although the phase matching angle for SHG at 205 nm is much higher for BBO than for KBBF, the effective nonlinearity of them is very similar and the 5.6 times smaller spatial walk-off in BBO provides a much better beam profile than with KBBF. One drawback of BBO is the three times smaller characteristic length for the group velocity mismatch than the one for KBBF. However, GVM only reduces the conversion efficiency and broadens the pulses but maintains the spatial beam profile, which is important for further beam shaping. The theoretical single pass conversion efficiency as a function of the waist radius is calculated using

Table 3.2.: *Overview of the parameters for BBO and KBBF, suitable for type I SHG of 410 nm [31]. Also listed are the corresponding calculated characteristic lengths and the single pass conversion efficiencies for $L = 5$ mm.*

410 nm (o) + 410 nm (o) = 205 nm (e)	BBO @ $-10°$ C	KBBF
refractive index $\mathfrak{n}$	1.691	1.491
group velocity index $\mathfrak{n}_1$ / $\mathfrak{n}_2$	1.776 / 2.165	1.529 / 1.654
walk-off δ [mrad]	14.09	65.83
phase matching angle [deg]	85.7	50.8
d_{eff} [pm/V]	0.343	0.354
transparency range [nm]	185 - 2600	157 - 3500
characteristic lengths and conversion efficiency		
L_{GVM} [mm](1)	0.8	2.6
L_δ [mm](2)	2.1	0.5
η(3)	8.7 %	5.8 %
η_{SNLO}(4)	8.6 %	5.8 %

(1) calculated using equation (3.4) with $\Delta t_1 = \Delta t_{2\omega} = 1.1$ ps

(2) calculated using equation (3.6) with $w_0 = 17$ μm

(3) calculated using equation (3.9) with $w_0 = 17$ μm, $\Delta k = 0$ and $\mathcal{P} = 0.6$ W average power in front of the cavity

(4) $\eta_{SNLO} = \mathcal{W}_2/\mathcal{W}_1$, calculated using SNLO software, same parameters as in (39)

equation (3.9) and the numerical model (s. figure 3.4). In spite of the comparable nonlinearity of the two crystals and the strong GVM in BBO the maximal single pass conversion efficiency in BBO is two times higher than for KBBF. Additionally the KBBF crystal is currently not commercially available and least of all with 5 mm crystal length, leaving BBO as the only present option for the type I SHG at 205 nm.

Resonant SHG

A Brewster cut BBO crystal with $\theta = 85.7°$ for type I phase matching is used in the second conversion stage for SHG at 205 nm. The phase matching angle of 85.7° is unfavorably close to the cut-off of phase matchable wavelength (90°). Approaching the cut-off the effective nonlinearity drops rapidly, hence, despite the high peak intensities of ps pulses in single pass only several percent of the power at 410 nm can be converted into the UV using a BBO crystal (see figure 3.4 and table 3.2). By cooling the crystal, however, this edge can be pushed to shorter wavelengths, as was demonstrated for SFG and SHG in BBO [37, 38]. At room temperature the nonlinearity of BBO for SHG

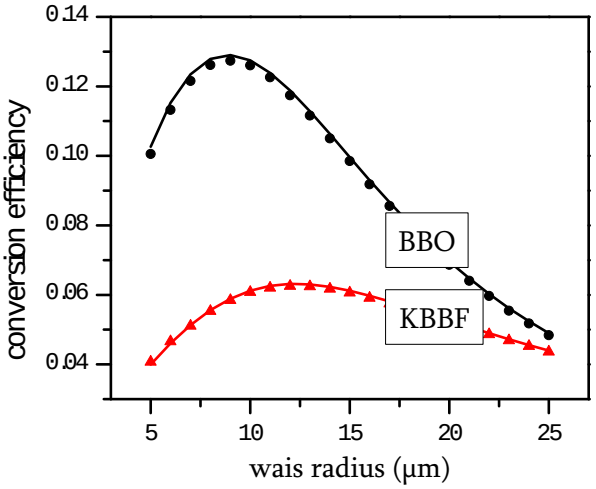

Figure 3.4.: *Single pass conversion efficiency as a function of the waist radius w_0 in a 5 mm long BBO (black) and KBBF (red) crystal respectively. The solid lines show the conversion efficiency calculated using equation (3.9) and the data represented by the symbols are obtained by the numerical model provided by the SNLO software. In both approaches absorption, group velocity dispersion, chirp and Fresnel losses are neglected.*

at 205 nm is $d_{\text{eff}} = 0.31$ pm/V. Cooling the crystal to $T = -10°\text{C}$ shifts the phase matching angle by about 1° resulting in a small increase of the effective nonlinearity to $d_{\text{eff}} = 0.35$ pm/V and enhances the transparency of the BBO crystal in the DUV wavelength range. That leads to around two times higher output power at 205 nm compared to SHG in a BBO crystal at room temperature.

For SHG in BBO at 205 nm, $A = 6$ and $B = 2$ giving an optimum focusing parameter of $\xi \approx 2.5$ (right plot in figure 3.2). With a confocal parameter of $b = 4$ mm ($w_0 = 17\ \mu$m) the optimum crystal length is then $L = 10$ mm and exceeds the characteristic lengths listed in table 3.2. As discussed above a shorter crystal (e.g. 5 mm long BBO) may be used in combination with an enhancement cavity for resonant SHG providing high output powers at the SH and maintaining a good beam profile.

The input beam at 410 nm wavelength is mode matched by two cylindrical lenses to fit the mode of the second SHG cavity. In this way the astigmatism may be removed, but beam distortions due to the spatial walk-off in the first SHG stage can only be partially compensated. The total coupling efficiency, including mode and impedance matching, amounts to only $40 - 50$ %, reducing the power entering the cavity. The second SHG stage houses a BBO crystal, cooled to $-10°\text{C}$, for SHG at 205 nm. To prevent condensation and convection, 32 mm long tubes oriented along the laser are used, that are purged with a steady flow of dry oxygen away from the crystal housing. Additionally, the oxygen prevents the crystal surfaces from being degraded by the intense UV light [11]. This UV degradation will be discussed in section 3.4.

Focusing mirrors with 175 mm radius of curvature generate a 17 μm beam waist in the crystal. All mirrors apart from the input coupler are high reflective ($\mathcal{R} > 99$ %) at 410 nm and arranged to give a full folding angle of 12 deg for astigmatism compensation caused by the Brewster cut crystal. Assuming that the cavity losses are dominated by the conversion process, the input coupler reflectivity for proper impedance matching is

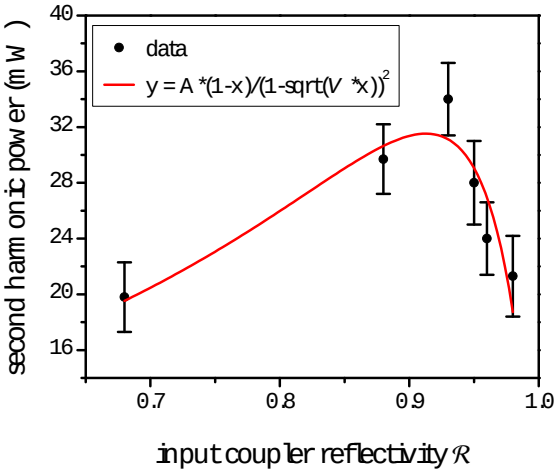

Figure 3.5.: *Second harmonic power at 205 nm as a function of the input coupler reflectivity. For* $\mathcal{R}_{\mathrm{IC}} = 92$ % *(maximum SH power) optimum impedance matching is achieved. Equation* (3.10) *is fitted to the data (solid line).*

calculated using equation (3.11) to be 78 % for 0.6 W average incident power. However limiting effects, as e.g. one and two-photon absorption at the fundamental as well as at the SH wavelength, are not taken into account in the above calculations. This effects further reduces the single pass conversion efficiency. The optimum input coupler with 92 % reflectivity is found experimentally by measuring the second harmonic power at 205 nm as a function of input coupler reflectivity. The results are plotted in figure 3.5.

3.3. Results

In this section results and characteristics of the laser system, which is described in the previous section, are summarized. The discussions include the overall achieved output powers, resonant conversion efficiencies and pulse characteristics. The characterization of the laser system is carried out in the original configuration of the Ti:sapphire laser and using Brewster cut nonlinear crystals. At this time the parts required for the improvement of the laser system were not at hand. After the characterization, the system was step by step modified in order to improve its output powers and beam profiles at different stages. The paragraphs in this section are organized as follows: First the original configuration of the respective stage is described. Then the modifications which lead to higher output powers are presented. Finally the characterization results of the respective stage are discussed.

Fundamental wavelength

Pumped by 9 W from a Verdi V10 the Ti:sapphire laser emits 1.8 W at 820 nm with a repetition rate of 82 MHz. Around 10 % of this output is branched off for stabilization, referencing and characterization of the laser. The remaining power of 1.6 W is used for the first SHG stage. To increase the output power of the Ti:sapphire laser the pump

laser, V10, is replaced by a V18 allowing to pump with 13.5 W. To keep the circulating intra cavity power at an acceptable level, to avoid changing the balance of GVD and SPM required for mode-locking, the original output coupler with 85 % reflectivity is replaced by one with 70 %. The resulting output power in this configuration amounts to around 2.3 W at 820 nm.

The characterization of the laser has been carried out in its original configuration (9 W pump, $\mathcal{R} = 0.85$). The duration of the fundamental pulses at 820 nm is measured with a background-free autocorrelator (Femtoscope, MC2) to $\Delta t_\omega = 1.3$ ps assuming a sech^2 pulse shape. The spectral intensity profile is obtained using an optical spectrum analyzer (Ando, AQ-6315A) and is best described by a sech^2 function giving a bandwidth of $\Delta\nu_\omega = 0.24$ THz. For transform limited pulses there is a minimum time bandwidth product $\Delta t_\omega \, \Delta\nu_\omega \geq c_B$. In case of sech^2 pulses the constant is $c_B = 0.315$ and for Gaussian shaped pulses it is $c_B = 0.441$. With the experimental parameters for the pulses at 820 nm a time bandwidth product of 0.24 THz $\times$ 1.3 ps = 0.31 is obtained.

SH wavelength

Pumped with $\mathcal{P}_\omega = 1.6$ W at 820 nm in front of the enhancement cavity an output power of $\mathcal{P}_{2\omega} = 600$ mW at 410 nm could be achieved with a 10 mm long crystal giving a conversion efficiency of $\eta = \mathcal{P}_{2\omega}/\mathcal{P}_\omega = 0.6$ W/1.6 W = 37 %. The LBO crystal is Brewster cut for the p-polarized fundamental beam at 820 nm thus the s-polarized second harmonic beam experiences 20 % Fresnel loss at the output surface. Accounting for this loss and the 90 % transmissivity of the output coupler for 410 nm the second harmonic power inside the crystal amounts to 830 mW resulting in a conversion efficiency of 52 % inside the crystal.

Replacing the Brewster cut LBO by a 90° cut, AR coated one and the focusing mirrors by spherical lenses (to avoid astigmatism), a conversion efficiency of 61 % ($\mathcal{P}_\omega = 1.3$ W, $\mathcal{P}_{2\omega} = 820$ mW) could be achieved. The lower incident power at 820 nm is due to transmission losses in an optical isolator. The isolator avoids back reflected light from the crystal facets that will compromise the mode-locking of the Ti:sapphire laser. With increasing single pass conversion efficiency the reflectivity of the input coupler must be decreased for proper impedance matching. The input coupler with 75 % reflectivity under couples the enhancement resonator limiting the output power at the SH.

The 10 mm long LBO crystal exceeds the characteristic length for the spatial walk-off L_δ by a factor 3 resulting in a reduced conversion efficiency and an elliptic second harmonic beam profile. Using a 5 mm long crystal instead improves the output beam profile while the conversion efficiency of 58 % remains almost the same providing 780 mW at 410 nm. Since the second harmonic beam is used for the next resonant conversion step, a good beam profile is favorable to improve the coupling efficiency.

With the modified Ti:sapphire laser around 1.9 W at 820 nm (measured after the optical isolator) are coupled into the SHG cavity. The SH power at 410 nm is measured

to be 1 W with a 5 mm long 90° cut, AR coated LBO, giving a conversion efficiency of 52 %. At this point a gradient input coupler became available and the cavity was optimized with respect to impedance matching.

In an ideal case, when all broadening effects are negligible a pulse narrowing upon SHG, according to equation (3.3), by a factor of 1.45 for sech^2 pulses is expected resulting in SH pulse duration of $\Delta t_{2\omega} = 1.3$ ps/1.45 = 0.89 ps. The phase matching bandwidth $\Delta\nu_{\mathrm{PM}} = \Delta k c/(2\pi)$ of a $L = 10$ mm LBO crystal, defined at the points where $L\,\Delta k$ varies between $\pm\pi$, amounts to 0.88 THz corresponding to a temporal walk-off of 1.1 ps. From the time bandwidth product $\Delta t_{\mathrm{GVM}}\,\Delta\nu_{\mathrm{PM}} = 0.315$ for a sech^2 pulse envelope the temporal broadening caused by GVM is given by $\Delta t_{\mathrm{GVM}} = 0.315/0.88$ THz = 0.35 ps and therefore the expected SH pulse duration including GVM calculates to $((0.89\text{ ps})^p + (0.35\text{ ps})^p)^{1/p} = 1$ ps with $p = 1.615$ [39]. The temporal pulse broadening goes along with a corresponding spectral narrowing maintaining Fourier limited pulses. To verify this expectation the SH pulse duration as well as the spectral envelope are measured. This measurements are carried out at the lower power, where the Ti:sapphire laser is in its original configuration and a Brewster cut LBO is used for SHG. The pulse duration is measured by cross correlating the SH with fundamental pulses from the Ti:sapphire laser by difference frequency generation (410 nm (e) - 820 nm (o) = 820 nm (o)) in a 2.5 mm long BBO crystal with the crossing angle limiting the interaction length to slightly shorter distances. Due to the temporal walk-off of 0.45 ps inside this crystal, the cross correlation curve is broadened by 0.315×0.45 ps = 0.14 ps, assuming that the sech^2 pulse shape is maintained. The FWHM of the cross correlation curve is measured to be $\Delta t_{\mathrm{DF}} = 1.9$ ps and using relation $(\Delta t_\omega^p + \Delta t_{2\omega}^p + (0.14\text{ ps})^p)^{(1/p)} = 1.9$ ps the duration of the second harmonic pulses is calculated to be $\Delta t_{2\omega} = 1.1$ ps which matches the estimated one quite well.

The spectrum at 410 nm is recorded using an optical spectrum analyzer and is found to posses a nearly sech^2 shape with a width of $\Delta\nu_{2\omega} = 0.32$ THz giving a time bandwidth product of 0.35. This value is somewhat higher than the Fourier limit of 0.315 but may be explained by alignment dependent small chirp of the laser pulses.

FH wavelength

For the fourth harmonic generation around 600 mW at 410 nm are mode-matched into the second SHG cavity containing a 5 mm long Brewster cut BBO crystal. Despite of the Fresnel losses of 23 % for the 205 nm wavelength at the back surface of the crystal up to 70 mW of average power at 205 nm can be extracted through one of the focusing mirrors. This results in a conversion efficiency of $\eta = 70$ mW/600 mW = 11.7 %. The high output power of 70 mW is only available for less than a minute. After this time the power drops to one tenth of the maximum due to heating effects after locking the cavity. A part of the intra cavity power is dissipated inside the crystal increasing the temperature and changing the phase matching condition. This can be compensated by lowering the

temperature of the crystal or tilting the crystal to align the phase matching angle. For several reasons, which will be discussed in the following section, this realignment does not restore the maximum power. The UV power settles at a level of 25 to 30 mW. At this level it remains stable for more than one hour.

As shown in figure 3.4 the conversion efficiency as a function of waist radius reaches its maximum at around 10 μm (using a BBO crystal) and decreases with increasing waist radius. However going to a weaker radius inside the crystal (e.g. 55 μm waist radius) improves the overall stability of the output beam, but a corresponding power decrease can not be observed in the experiment. This indicates some sort of saturation effect for tighter focusing. Small variations in the output power could be observed for different crystals from different manufacturers. These can be attributed to different degrees of purity which affect the transparency range and the phase matching cut-off.

Replacing the Brewster-cut BBO by a 90° cut, AR coated one does not show the same increase as described in the previous paragraph for the first resonant SHG. Also the power increase to 900 mW at 410 nm does not lead to a corresponding power increase at 205 nm for almost all crystals in our lab (Brewster and 90° cut). Starting with a rather high average power at 205 nm it always settles at a level of 25 to 30 mW.

However one of the crystals (BBO, $5 \times 5 \times 5$ mm^3, $\theta = 86.3°$, AR at 410 nm and P at 205 nm, manufactured by the Institute of Geology and Mineralogy SB RAS) behaves differently. The maximum observed power is measured to $\sim$ 100 mW (with the weaker focus of 55 μm waist radius and 90° cut BBO crystal) and after the fast drop the power level settles at around 60 mW for more than 30 minutes. The reason for this behavior may probably be a higher purity of the crystal, but further investigations are required.

In the second resonant SHG stage a strong group velocity mismatch in BBO causes a temporal walk-off of 6.5 ps between the 205 nm and 410 nm pulses after traveling the crystal length $L = 5$ mm. This walk-off corresponds to a phase matching bandwidth of 0.15 THz at 410 nm, so a pulse broadening by 0.315×6.5 ps $= 2.1$ ps (for sech^2 pulse envelope) is expected. The fourth harmonic pulse length is calculated to be $\Delta t_{4\omega} = ((1.1 \text{ ps}/1.45)^p + (2.1 \text{ ps})^p)^{(1/p)} = 2.3$ ps. The actual pulse duration is determined by cross correlating the 205 nm pulses with those at 820 nm in a 0.1 mm thin BBO crystal, so that the temporal walk-off can be neglected. With the cross correlation width of $\Delta t_{\mathrm{DF}} = 2.9$ ps the pulse width at 205 nm is obtained using the relation $(\Delta t_{4\omega}^p + \Delta t_{\omega}^2)^{1/p}$, resulting in $\Delta t_{4\omega} = 2.4$ ps. The spectral bandwidth at 205 nm is measured with a monochromator (Jobin Yvon, HR640) to $\Delta\nu_{4\omega} = 0.14$ THz (figure 3.6) giving rise to a time bandwidth product of 0.34. That is close enough to the Fourier limit so it seems safe to assume chirp free pulses at 205 nm as well as at 410 nm.

With the conversion efficiencies of 52 % (5 mm LBO) in the first and 11.1 % (5 mm BBO) in the second stage respectively using 90° cut, AR coated nonlinear crystals, an overall efficiency of $\sim$ 6 % is achieved providing an average output power of 100 mW at 205 nm for only a couple of minutes and 60 mW for longer than 30 minutes. Mea-

surements of the auto and cross correlation curves and spectral envelopes (shown in figure 3.6) revealed close to Fourier limited pules at the fundamental, second and fourth harmonic. The characteristics of the all-solid state laser system, as described above, are summarized in table 3.3.

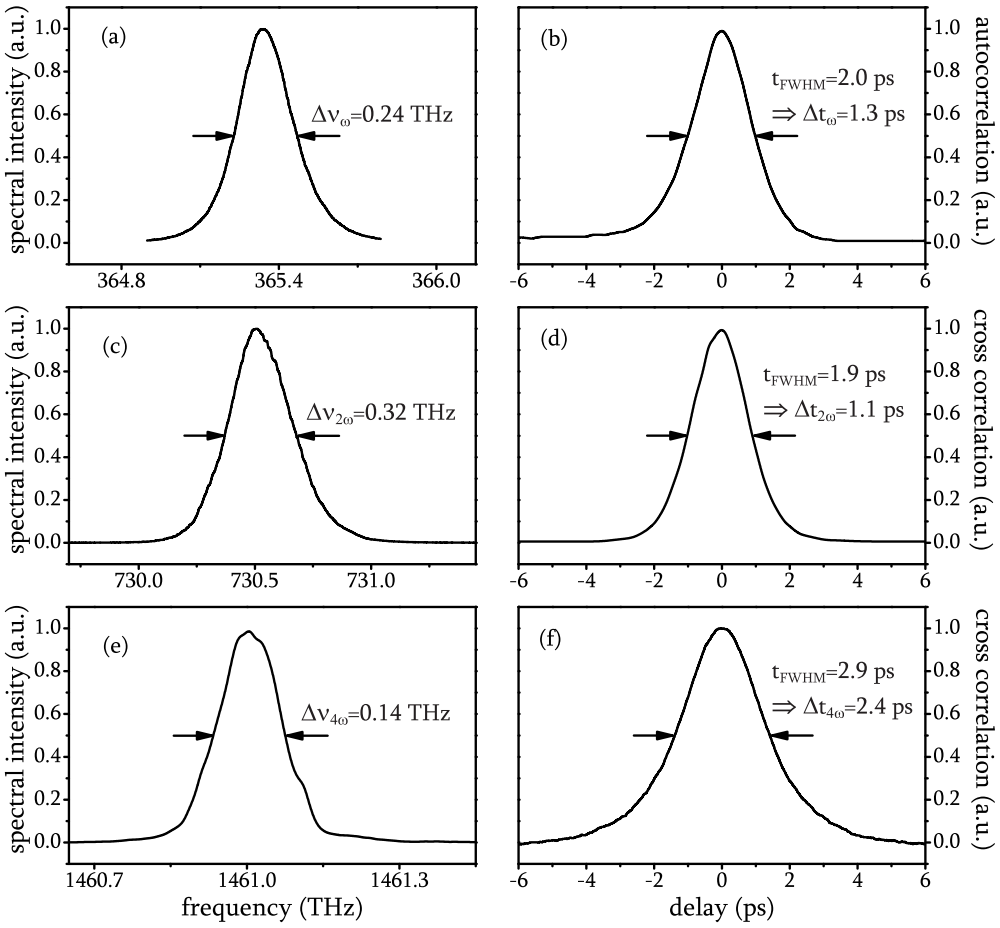

Figure 3.6.: *Power spectra and correlation measurements for the fundamental, second harmonic and fourth harmonic pulses.(a) Power spectrum and (b) auto correlation trace of the fundamental pulses at 820 nm. (c) Power spectrum and (d) cross correlation trace of the second harmonic pulses at 410 nm. (e) Power spectrum and (f) cross correlation trace of the fourth harmonic pulses.*

Table 3.3.: *Overview about the characteristics of the laser system.*

λ [nm]	$\Delta\nu$ [THz]	NL crystal	output power	acceptance bandwidth	GVM	pulse duration	TBP
820.58	0.24		2.1 W$^{(1)}$			1.3 ps	0.31
410.29	0.32	LBO	1 W$^{(1)}$	0.88 THz	1.1 ps	1.1 ps	0.35
205.15	0.14	BBO	60 mW$^{(1,2)}$	0.15 THz	6.5 ps	2.4 ps	0.34

(1) This high powers were achieved with the modified Ti:sapphire laser (13.5 W pump, $\mathcal{R} = 0.75$).
(2) The measured maximum UV power amounts to around 100 mW (for explanations see text).

3.4. UV degradation

During the operation of the laser system a power decrease of the UV light could be observed on different time scales. A fast power drop occurred within less than 1 second and is due to thermal effects as discussed above. After realignment the power settled at an intermediate level. After 30 to 60 minutes a slower power decrease could be observed. This can be attributed to a degradation of the BBO crystal as reported in [11,40]. There are some suggestions for the origin of this degradation: photo chemical reactions at the crystals surfaces, distortion of spontaneous polarization of the BBO or increased crystal defects upon interaction with UV radiation. These effects can be slowed down in a very clean and oil free environment of the crystal, by purging the dust and out-gas from the mechanical components of the cavity with nitrogen [40]. Photochemical reactions on the crystal surfaces can be prevented by flushing the surfaces with oxygen [11].

As demonstrated in [40] the degradation rate is proportional to the strength of the UV optical electric field. Generating a weaker focus inside the crystal reduces the UV intensity at the surfaces and the degradation rate. This could be verified by varying the waist radius inside the crystal and measuring the output power over around 60 minutes.

A similar degradation was observed in operating the enhancement cavity at 205 nm in vacuum. Here the high reflective mirrors degrade upon UV radiation observable as a decrease in the finesse of the cavity. This degradation may be attributed to the deposition of carbon atoms onto the dielectric surface [41]. These carbon atoms are generated by cracking residual hydrocarbons from e.g. the pumps or sealings. Because of the higher intensity most radicals are generated in and close to the focus leading to a faster degradation of nearby mirrors. The quality of the mirrors may be restored by treating them with oxygen plasma followed by thermal annealing (180 min at 230°C) [41]. In our case it turned out to be sufficient to fill the vacuum chamber with oxygen to at least 1 mbar pressure or to expose the mirrors to air. After this procedure the cavity finesse is restored.

4. Spectroscopy at the laser fundamental: Cs $6S - 8S$

This chapter reports on experimental investigations of two crucial effects in DFCS: the impact of chirped pulses and a non-centered pulse spectrum on the spectroscopy. These effects are only sparsely explored in DFCS of two-photon transitions with no resonant intermediate states. They result in a significant decrease of the excitation rate and thus may present a significant challenge in DFCS with short pulses which are required for efficient nonlinear conversion as e.g. HHG.

4.1. Motivation

The transition rates of a two-photon transition are usually orders of magnitude lower than for dipole allowed transitions. Thus, for efficient excitation high intensities and long interaction times are required. For a number of technical reasons the available laser power drops rapidly at shorter wavelengths so the detected signal is expected to be small. Known systematic effects, chirped pulses and non-centered spectrum, may further reduce this already weak signal and may thus be a serious challenge. Indeed, short pulses easily acquire a phase shift upon propagation through any kind of medium. Longer pulses, however, (e.g. ps or ns pulses) are less sensitive to chirp. Here meters of material are necessary to chirp such long pulses. But on the other hand they provide lower peak intensities and the nonlinear conversion precesses are less efficient.

Spectroscopy with pulses possessing a symmetric phase shift relative to the atomic transition will result in a partially destructive interference of frequency modes, reducing the transition rate. For an antisymmetric phase shift this is not the case, because it cancels in the pairwise addition of modes.

Furthermore for a maximized transition amplitude the pulse spectrum should be centered with respect to the transition frequency, otherwise not all of the comb modes contribute to drive the transition. These two effects were discussed theoretically in section 2.3 and 2.4 and will be analyzed experimentally in this chapter using the $6\,^2S_{1/2} - 8\,^2S_{1/2}$ two-photon interval in ^{133}Cs.

4.2. Setup

The experiments are performed using the stabilized ps Ti:sapphire laser described in section 3.2.1. To match the two-photon transition frequency the laser is tuned to 822 nm wavelength. At this point we are only interested in the signal amplitude so the reference fs frequency comb is not used. The spectroscopy takes place in a 10 cm long cesium gas-cell at room temperature with a vapor pressure of 1.33×10^{-6} mbar. A level diagram for Cs with its relevant states and transitions is shown in figure 4.1.

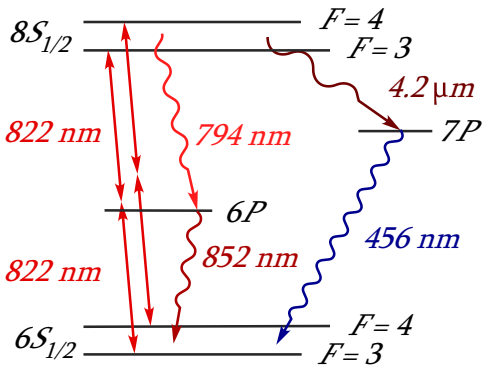

Figure 4.1.: *Cesium level diagram with relevant states and transitions. The two-photon transition is accessible by two photons at 822 nm. The exited state decays via the $7P$ or $6P$ state back into the ground state emitting two successive photons.*

4.2.1. Non-centered spectrum

A schematic drawing of the setup for the investigation of a non-centered frequency comb is shown in figure 4.2. The pulses at 822 nm are coupled through a Cs gas-cell. Two

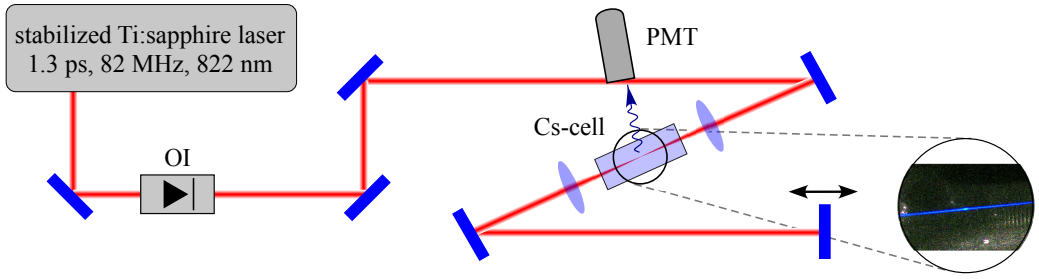

Figure 4.2.: *Schematic of the setup for investigation of the non-centered frequency comb. The Ti:sapphire laser (see section 3.2.1) is focused into the center of a Cs-cell. An adjustable plane mirror behind the cell retro-reflects the pulses such that two counter propagating pulses overlap at the center of the cell. An optical isolator (OI) avoids back-reflections into the laser. Inset: A photograph of the Cs-cell. The somewhat brighter spot in the center shows the pulse collision volume which is the origin of the Doppler-free signal.*

focusing lenses around this cell (f = 150 mm) generate a 56 μm waist diameter at the center of the Cs-cell. A plane mirror mounted on a linear translation stage retro-reflects the laser beam. It is placed 1.83 m behind the Cs-cell to ensure that two counter propagating pulses overlap at the center of the cell. An optical isolator avoids back-reflections into the laser which could otherwise disturb the mode-locking.

Along the entire length of the cell the atoms can absorb two photons coming from the same direction generating the Doppler-broadened background. At the pulse collision volume additional absorption of two counter propagating photons takes place providing the narrow Doppler-free signal. This region appears as a somewhat brighter spot in the inset in figure 4.2. The excited $8\,^2S_{1/2}$ state decays via the $7P$ state emitting two successive photons, one in the IR at 4.2 μm and one in the visible wavelength range at 456 nm. The latter one is detected using a PMT (Hamamatsu, R6358) by imaging the pulse collision volume onto its photo cathode. An interference filter with 450 nm central wavelength and 15 nm bandwidth suppresses background coming from the laser and the environment. With a PMT quantum efficiency of 17(2) %, a filter transmittance of 62(1) % at 456 nm and a solid angle of 5(1) % the overall detection efficiency amounts to 0.5(1) %.

4.2.2. Chirp investigation

The characterization of the fundamental pulses at 820 nm in section 3.3 revealed transform limited pulses. However, depending on the alignment of the laser, the output pulses may exhibit a small chirp. In order to investigate its impact on the excitation rate, a controllable amount of chirp is introduced by e.g. sending the comb through optical fibers of variable length. The two main mechanisms responsible for a chirp of short pulses are group velocity dispersion (GVD) and self phase modulation (SPM). While GVD causes a temporal broadening of the pulses, SPM broadens the spectrum. The characteristic lengths L_D for GVD and L_NL for SPM are defined as [42]

$$L_\mathrm{D} = \frac{\Delta t^2}{4\,\ln(2)\,|k''|}\,, \tag{4.1a}$$

$$L_\mathrm{NL} = \frac{1}{\kappa\,\mathcal{P}_p}\,. \tag{4.1b}$$

The dispersive length depends on the initial FWHM pulse duration Δt and is the distance after which GVD broadens the pulse duration by $\sqrt{2}$. The non-linear length is proportional to the inverse peak power $\mathcal{P}_p$ and nonlinear coefficient $\kappa = \mathfrak{n}_2\omega_0/cA_\mathrm{eff}$, which is a function of the second order nonlinear refractive index $\mathfrak{n}_2$, carrier frequency ω_0 and effective core area A_eff. After traveling this length the maximum spectral phase shift through SPM amounts to $\phi = \pi/2$. For 1 W average power and 1.3 ps pulses propagating in a fused silica ($k'' = 3.44 \times 10^{-26}$ s^2/m and $\mathfrak{n}^2 = 2.6 \times 10^{-6}$ cm^2/W) of 15 μm

diameter the characteristic lengths for GVD and SPM are calculated to be $L_D \approx 18$ m and $L_{NL} = 0.1$ m. With these numbers one possibility to seriously chirp ps pulses is by launching them into an optical fiber.

For chirp investigation the setup as described in the previous paragraph is extend by an optical fiber (s. figure 4.3).

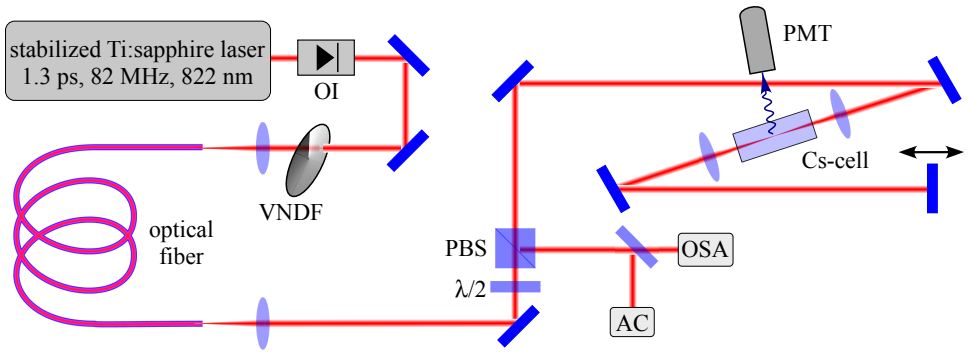

Figure 4.3.: *Schematic drawing of the experimental setup for chirp investigation. For chirping the pulses they are coupled through an optical fiber. To vary the amount of chirp either the power coupled through the fiber is adjusted by a variable neutral density filter (VNDF) or the fiber length is varied by successive shortening. A fraction of power is branched off for measuring the spectral and temporal widths using an optical spectrum analyzer (OSA) and an autocorralator (AC) respectively.*

In order to generate a wide range of chirp parameters the power level coupled through the fiber as well as the length of the fiber can be changed. By changing the power level, using a variable neutral density filter (VNDF), the strength of SPM is varied. To analyze the impact of temporally broadened pulses the fiber is successively shortened while the power level is kept constant. In order to maintain the alignment through the Cs gas-cell, the fiber is always shortened at the input coupling side. Behind the fiber an adjustable fraction of power is branched off to feed an autocorrelator for determination of the pulse duration Δt and an optical spectrum analyzer which measures the spectral width $\Delta\nu$.

4.3. Results

The only stable isotope ^{133}Cs exhibits a nuclear spin $I = 7/2$ which cause the ground and the excited state to split into hyperfine doublets with total atomic angular momenta $F = |I - J| = 3$ and $F = I + J = 4$. Following the two-photon selection rules (see section 2.2.3) only transitions with $\Delta F = 0$ and $\Delta m_F = 0$ are allowed resulting in two observable hyperfine transitions separated by 4.2 GHz. A typical spectrum is shown in figure 4.4. Using linearly polarized light a narrow Doppler-free signal superimposed on the Doppler-broadened background is obtained. This background is a superposition of

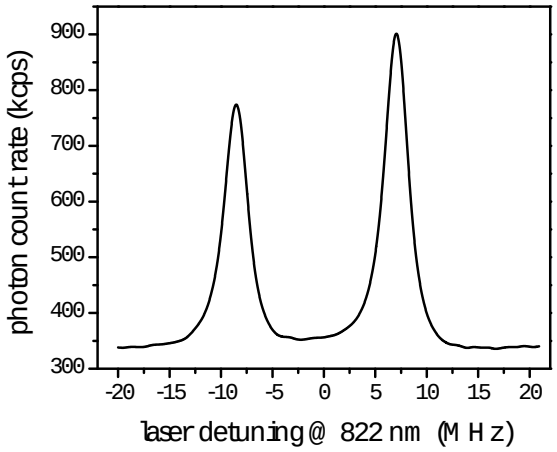

Figure 4.4.: *Typical Cs $6S-8S$ spectrum showing two allowed hyperfine transitions with $F = 3 \rightarrow F = 3$ and $F = 4 \rightarrow F = 4$. The Doppler-free signal is superimposed on the Doppler-broadened background.*

the two Doppler-broadened hyperfine components. This doublet is of approximately the same intensity so the background is enhanced by around a factor 2 reducing the contrast as defined by equation (2.7) by the same factor. Furthermore the around 0.7 mm long interaction region is imaged through an aperture of around 3 mm further reducing the contrast which finally results in $C_{\text{comb}} \approx 4$.

For every set of parameters up to 20 successive scans are recorded. Two Lorentzians are fitted to the hyperfine doublet accounting for Poissonian statistics only. The reduced χ^2 ranges between 1 and 2.4. The extracted signal strength is normalized to the squared average power, measured with 5 % uncertainty and smallest TBP. The results are then plotted as a function of the measured time bandwidth product.

4.3.1. Detuning of spectral envelope

To analyze the impact of a non-centered pulse spectrum the signal strength of the hyperfine doublet is measured as a function of detuning with respect to the transition frequency. To make the particular runs comparable the signal strengths are normalized to the squared incident intensity. The envelope shift is measured by an optical spectrum analyzer, which was calibrated using a cw laser diode running at around 820 nm. The results are shown in the left plot in figure 4.5. A Gaussian according to equation (2.28) is fitted to the experimental data represented by the symbols revealing good agreement between theory and experiment.

Although the intermediate $6P_J$ states are off resonant, they are close enough to cause a strong AC Stark shift of around -10 MHz at 1 W laser power. While tuning the spectral envelope with respect to the transition frequency the effective laser power used for the spectroscopy decreases exponentially with $(\tau_\omega \mu \omega_r)^2/2$ where $\tau_\omega = \Delta t_\omega / \sqrt{2\ln(2)}$. This intensity decrease results in a reduced AC-Stark effect shifting the line center, as shown in the right plot in figure 4.5.

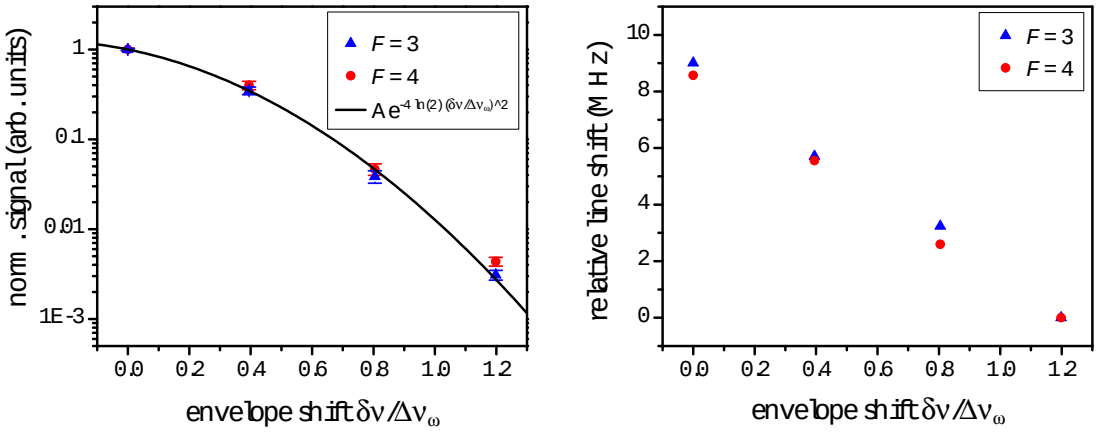

Figure 4.5.: *Left: Normalized signal plotted as a function of spectral detuning in units of the spectral FWHM $\Delta\nu_\omega$ (symbols). An exponential function as defined in equation (2.28) is fitted to the data (solid line). Right: Shift of the line positions as a function of the envelope detuning.*

4.3.2. Chirp investigation

In order to investigate the impact of chirped pulses on the transition rates, a chirp is introduces by sending the pulses through an optical fiber. The amount of chirp may be variated either by sending the pulses through fibers of variable length while leaving the laser power level constant (analyzing GVD) or by changing the power level coupled through a fiber of constant length (analyzing SPM). In the following the results of the measurements are presented.

PCF: 5 m

In a first set of measurements the pulses are chirped using a 5 m long photonic crystal fiber (PCF) (CrystalFiber, LMA-20, 15 μm mode field diameter). In order to vary the amount of chirp, different power levels are coupled through the fiber. For present experimental parameters, GVD is negligible and SPM dominates. To characterize the chirped pulses, their pulse durations and spectral widths are measured for every power setting and the time bandwidth products are calculated. The normalized signal amplitudes of the two hyperfine components as functions of the TBP are plotted in the bottom plot in figure 4.6. Variating the power level coupled through the fiber between 7 mW and 355 mW allows the TBP to vary over one order of magnitude. The top-left and top right plots show the corresponding autocorrelation curves and spectral envelopes respectively. While the autocorralation traces indicate a constant pulse duration the spectra show, as expected, a significant broadening with increasing average power.

For comparison of the experimental data with the theoretical model derived in sec-

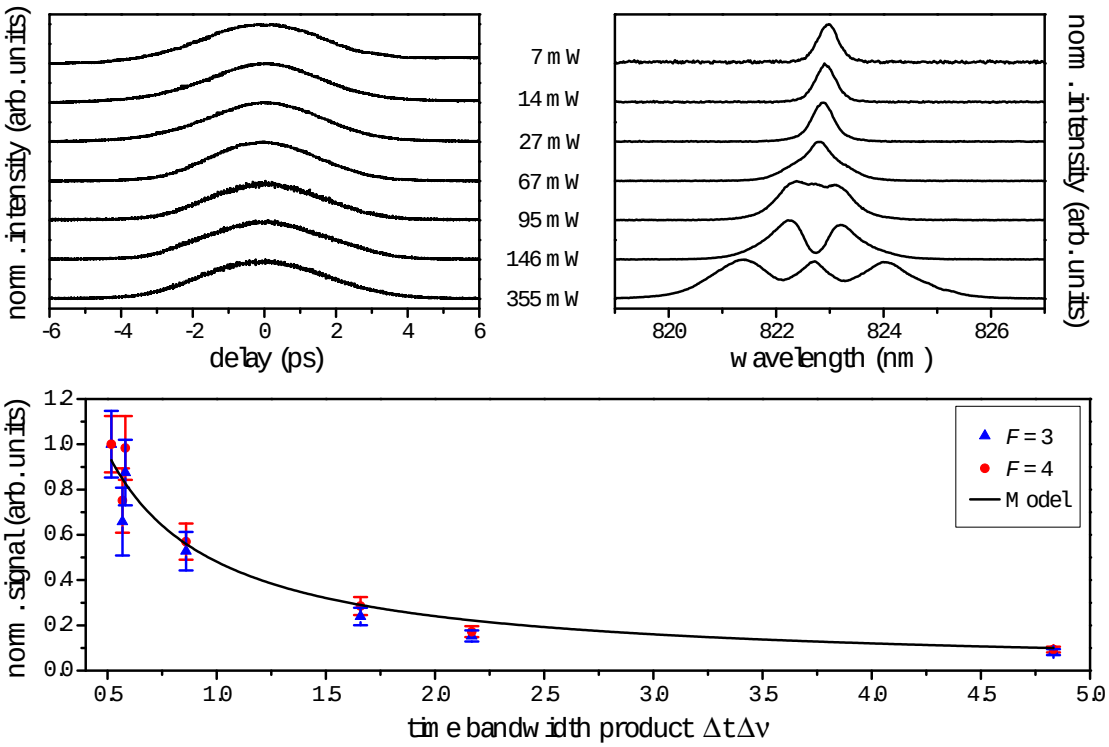

Figure 4.6.: *Top-left: autocorrelation traces, top-right: pulse spectra measured after chirping the pulses in a 5 m long PCF (curves are off-set for clarity). Bottom: Normalized transition rate as a function of the TBP. The solid line shows the theoretical model according to equation* (4.2)*, normalized to the transition rate with unchirped pulses.*

tion 2.3 equation (2.27) is integrated with respect to the propagation direction z. The resulting expression is independent of the excitation volume and for zero detuning ($\Delta\omega_{eg} = 0$) simplifies to

$$\Re_{ge} = \frac{G}{\Delta t\, \Delta\nu}\,. \tag{4.2}$$

This expression is fitted to the experimental data in figure 4.6 with G as the only varying parameter showing good agreement with theory.

PSM: 1 m

To reach even larger time bandwidth products, in a second set of measurements the pulses are chirped using a 1 m long polarization maintaining single mode fiber (PSM) (Newport, F-SPF, 4.2 μm mode field diameter). Due to its smaller mode field diameter compared to the PCF fiber the SPM contribution is enhanced and the TBP can vary

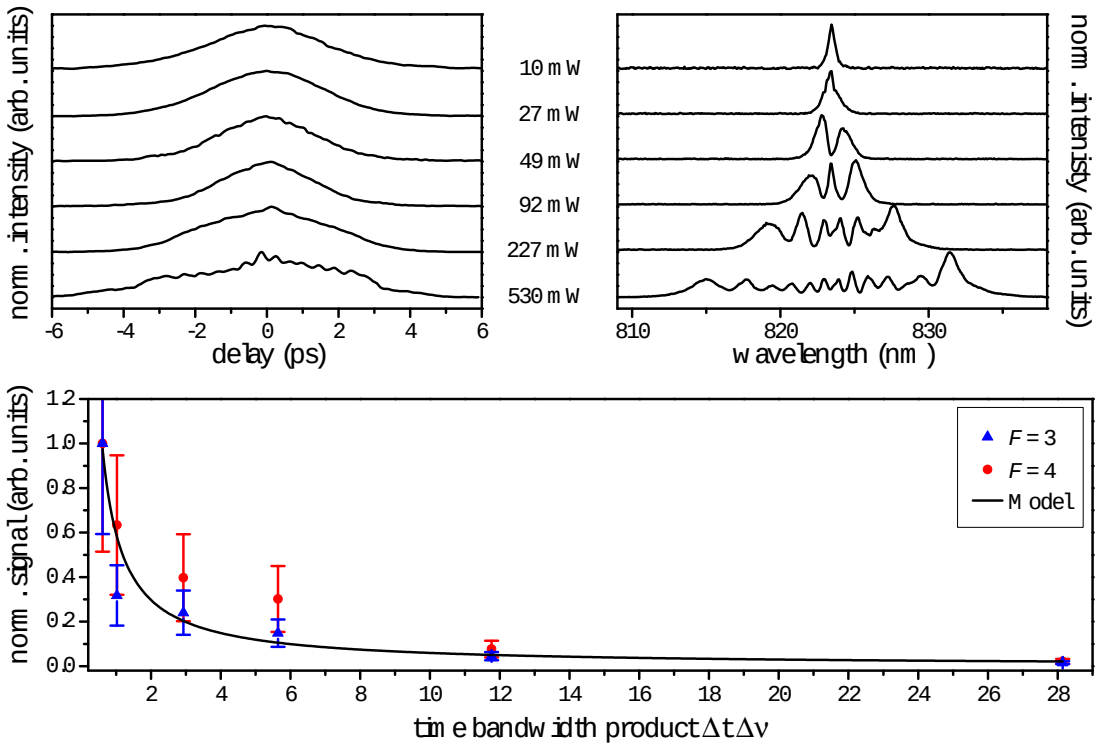

Figure 4.7.: *Top-left: autocorrelation traces, top-right: pulse spectra measured after chirping the pulses in a 1 m long PSM (curves are off-set for clarity). Bottom: Normalized transition rate as a function of the TBP. The solid line shows the theoretical model according to equation* (4.2)*, normalized to the transition rate with unchirped pulses.*

by two orders of magnitude for power levels ranging between 10 mW and 530 mW. The results for the 1 m long PSM fiber are shown in figure 4.7. The top-left and top-right plots show the autocorrelation and spectral envelope curves for power levels ranging between 10 mW and 530 mW. In this case not only the spectrum but also the temporal pulse profile becomes broader with increasing power levels. Fitting equation (4.2) to the experimental data shows good agreement with theory.

PCF: constant intensity

To analyze the influence of GVD the average power coupled through the PCF is kept approximately constant (81 . . . 115 mW) while the fiber length is varied between 10 m and 0.3 m. At this power levels the nonlinear length L_{NL} varies between 1.24 m and 0.87 m. The normalized transition rates and the corresponding autocorrelation traces and pulse spectra are shown in figure 4.8. Here the strong temporal broadening indicates an

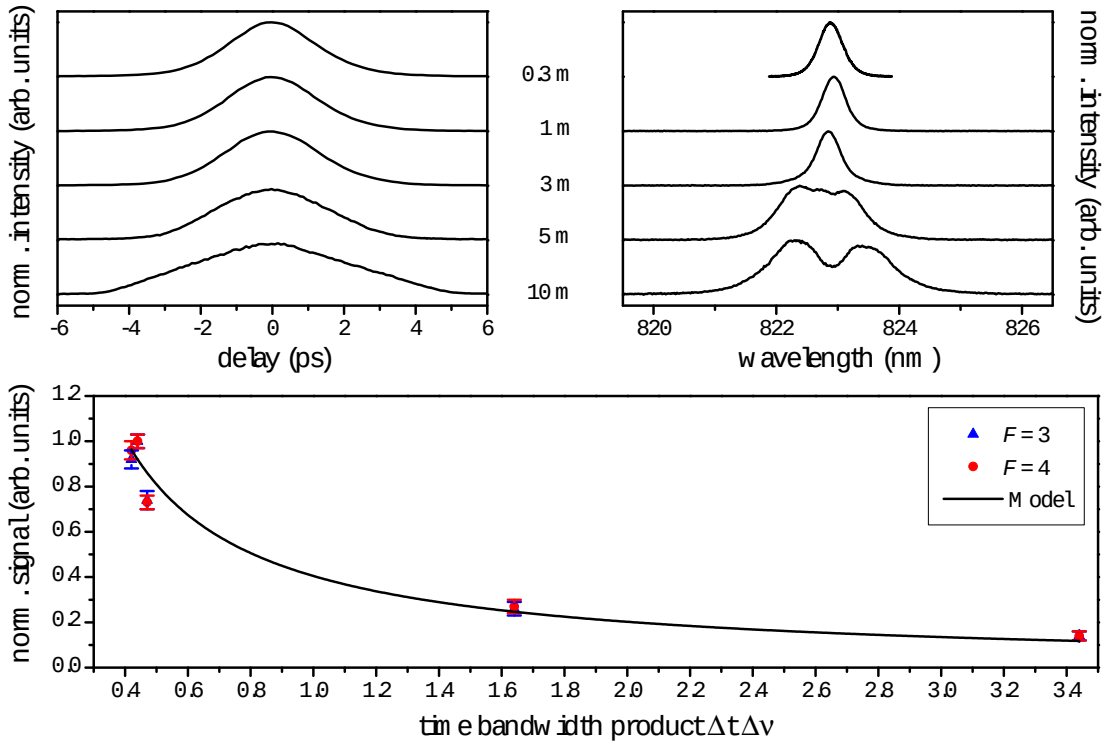

Figure 4.8.: *Top-left: autocorrelation traces, top-right: pulse spectra, both measured after chirping the pulses in a PCF fiber of different length (curves off-set for clarity) at constant average power. Bottom: Normalized transition rate as a function of the time bandwidth product. The solid line shows the theoretical model according equation* (4.2)*, normalized to the transition rate with unchirped pulses.*

increased GVD contribution, but it is accompanied by a moderate spectral broadening, i.e. SPM is still present.

The theoretical model to describe the decay of the transition rate in DFCS with chirped pulses was developed assuming pulses with a Gaussian envelope. However, measuring the temporal and spectral profile of the initial, unchirped pulses reveals that they are best described by a sech^2 function. After chirping the pulses the spectral envelopes as well as the autocorrelation curves show significant deviations from a Gaussian shape under some of the experimental conditions investigated. Nevertheless the decrease of the transition rate with respect to the TBP is well described by the model developed in section 2.3. For pulse shapes that largely differ from a Gaussian the simple theory will not hold. Even though the transition rate decay with the chirp parameter is similar, it may not increase the time bandwidth product accordingly [43].

5. Spectroscopy at the second harmonic: Mg $3S - 3D$

In this chapter the suitability of a frequency doubled comb for DFCS is demonstrated by measuring the absolute frequency of the $^1S_0(3s^2) - {}^1D_2(3s3d)$ two-photon transition in ^{24}Mg and the isotope shift between ^{26}Mg and ^{24}Mg. The measurements serve as a proof of principle and test of the laser system. These measurements reduce the uncertainties of the frequencies in Mg by more than two orders of magnitude.

5.1. Motivation

In the previous section direct two-photon frequency comb spectroscopy using a mode-locked ps Ti:sapphire laser was demonstrated. The method was examined with respect to spectral envelope alignment and impact of chirped pulses on the transition rate. Most of the envisioned applications invoke spectroscopy with nonlinear converted combs. The application of a nonlinearly converted mode-locked laser for spectroscopy in the DUV was demonstrated by S. Witte on a two-photon transition at 212 nm in krypton [44] and by R. Th. Zinkstok on a transition in xenon at 125 nm [45] using a Ramsey-type quantum interference scheme. In their approach the transition is probed by a train of multiple pulses, which strictly speaking do not form a frequency comb.

The experiments presented in this thesis, therefore, demonstrate for the first time the capability of a nonlinear converted comb for DFCS. A frequency doubled comb at 431 nm is used to probe the $^1S_0(3s^2) - {}^1D_2(3s3d)$ two-photon interval in ^{24}Mg. The features of this transition are:

- The laser system described in chapter 3 is designed to generate i.a. a frequency comb at 410 nm. The two-photon transition wavelength in Mg of 431 nm is close enough to 410 nm, so it can be generated using the same setup with only small modifications.

- The transition takes place from the ground state of the neutral atom where the state population is very high.

- An atomic beam is easily generated using a Mg-oven. By adjusting the oven temperature the particle density can be varied.

- The laser pulses cross the atomic beam perpendicularly, so the excitation geometry is very similar to hydrogen spectroscopy in the DUV wavelength region, which will be discussed in the next chapter.

The $^1S_0(3s^2) - {}^1D_2(3s3d)$ two-photon interval in ^{24}Mg is thus an excellent candidate to test the laser setup after resonant SHG and to prove its suitability for Doppler-free two-photon DFCS. Its natural line width amounts to 2 MHz.

5.2. Setup

The measurements are carried out using the Ti:sapphire laser (s. section 3.2.1) tuned to 862 nm to match the transition frequency and its output is frequency doubled in the resonant SHG cavity described in section 3.2.3. A schematic drawing of the setup is shown in figure 5.1. The spectroscopy takes place in an enhancement resonator for the

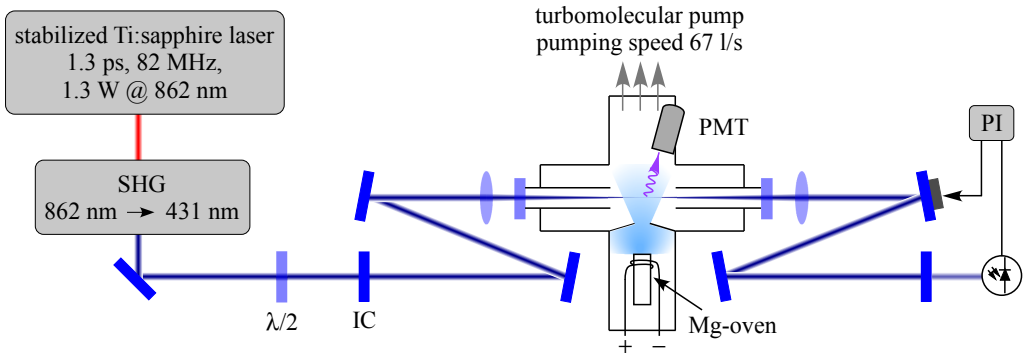

Figure 5.1.: *Schematic drawing of the setup for Mg spectroscopy. The Ti:sapphire laser and the resonant SHG cavity are described in section 3.2.1 and 3.2.3. Spectroscopy is carried out in an enhancement resonator for 431 nm built around the spectrometer. The length of the resonator ensures a pulse collision volume at the center of the spectrometer. IC: input coupler.*

generated 431 nm pulses built around a small vacuum chamber containing the Mg-oven. A level diagram for Mg with its relevant states and transitions is shown in figure 5.2. The emitted fluorescence is detected by a PMT placed outside the chamber through a CaF_2 detection window. In the following the modifications of the laser system to drive the transition, the reference fs comb and the spectrometer will be described in more detail.

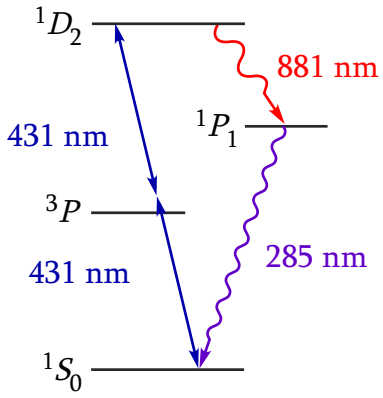

Figure 5.2.: *Magnesium level diagram with relevant states and transitions. The two-photon interval is accessible by two photons at 431 nm and the excited state decays via the $^1P_1$ state back into the ground state emitting two subsequent fluorescence photons. The natural line width amounts to 2 MHz. Transitions to the ^3P state are forbidden by intersystem crossing and do not contribute to the spectrum.*

5.2.1. Laser system

The wide tuning range of a Ti:sapphire laser allows to set the output wavelength to 862 nm. The angle of the built-in birefringent filter (BiFi) for wavelength selection is adjusted for maximum output power at 862 nm providing 1.3 W usable for SHG. The laser is stabilized and referenced as described in section 3.2.1 and its output is mode-matched into a SHG cavity resonating at 862 nm. The HR mirrors of the resonator described in section 3.2.3 provide an adequate high reflectivity at this wavelength and the conversion still exceeds all other losses. For proper phase matching for SHG at 431 nm the LBO crystal is tilted by $\approx 4°$ with respect to the original position for SHG at 410 nm to $\theta = 25.6°$ providing an effective nonlinearity of $d_{\text{eff}} = 0.785$ pm/V. This crystal tilt gives rise to total Fresnel losses of 11 % at the fundamental wavelength on the crystals surfaces. Accounting for these Fresnel losses the theoretical single pass conversion efficiency is calculated using the SNLO software to be 17 %. Setting now $1 - \mathcal{V} = \eta_d + 0.11$, equation (3.11) modifies to

$$\frac{1}{\mathcal{R}_{\text{IC}} - 0.11} = 1 + \frac{1}{1 - \mathcal{R}_{\text{IC}}}\,\eta_{nd}\,,$$

resulting in $\mathcal{R}_{\text{IC}} = 73$ %. With an input coupler of 75 % reflectivity the enhancement resonator is not exactly impedance matched in case of SHG at 431 nm, however a conversion efficiency of 33 % is achieved experimentally, providing 430 mW output power at 431 nm while pumped by 1.3 W at 862 nm.

Due to its dimensions the SHG resonators are subject to fluctuations and perturbations arising e.g. from beam pointing, air turbulences or acoustics which cannot completely be suppressed by the feedback control of the stabilization. The sensitivity of resonators to such fluctuations gets worse for shorter wavelengths. While the first SHG cavity is still robust, small perturbations are enough to drop the following resonators out of lock. For this reason it is favorable to shorten their lengths. With an e.g. doubled FSR the resonator acts as a filter cavity with every other pulse resonantly coupled into the cavity

(or in the frequency domain picture every other mode). That reduces the power inside the resonator and thus the conversion efficiency. Indeed, after shortening the first SHG cavity the effective conversion efficiency dropped to 17 % providing around 230 mW output power at 431 nm.

For Mg-spectroscopy the 431 nm beam is mode-matched into a linear resonator built around the spectrometer. AR coated windows allow the laser to pass the chamber. Two $f = 750$ mm lenses generate a rather weak focus of $w_0 = 132$ μm at the center of the vacuum chamber, to reduce time of flight broadening. The transmitted power through the lenses and windows is measured to be $\mathcal{T} = 87$ % and with a HR mirror reflectivity of $\mathcal{R} = 99.2$ % at 431 nm the round trip losses amount to $1 - \mathcal{V} = 71.6$ %. The most adequate input coupler at hand ($\mathcal{R}_{\mathrm{IC}} = 88$ % at 431 nm) yields a theoretical enhancement of 2.8 and experimentally an enhancement of 2 is achieved. The free spectral range FSR $= \nu_{\mathrm{rep}}/2$ of the spectroscopy resonator ensures that two counter propagating pulses overlap at its center.

In order to lock the linear resonator, an error signal is generated by modulating a piezo mounted mirror. The transmitted light is detected by a photo diode and its output is sent to a lock-in amplifier.

5.2.2. Spectrometer

The spectrometer housing the Mg-oven is evacuated to around 10^{-5} mbar. The atomic beam is created by heating a Mg-oven consisting of a 2 mm diameter tantalum tube by applying an electrical current to a single winding of tantalum wire. The oven is loaded with a 1.6 mm in diameter and 5 to 7 mm long magnesium wire of 99.9 % purity and natural isotopic composition.

The highly reactive magnesium forms an oxide layer (MgO) which has a much higher boiling temperature (3600°C) than magnesium (1091°C) at atmospheric pressure. By heating the oven the inner part might melt while held together by the oxide layer and at some point this layer breaks up and the magnesium bursts out of the oven. Treating the magnesium rod with citric acid replaces the oxide layer by a magnesium citrate layer ($C_6H_6O_7Mg$) whose boiling temperature is far below the one of magnesium. So while heating the oven first the magnesium citrate evaporates and then by further increasing the temperature a magnesium atomic beam is created. The atom emission distribution in front of the oven can be approximated by a cosine function, so the atoms leave the oven in an solid angle of 2π. A shield with an aperture of 4 mm in diameter and 5 mm distance reduces the beam spread and prevents coating the laser- and detection-windows. Each of the two laser-windows is glued (using Torr Seal) to a 10 cm long metal tube of 8 mm inner diameter for further protection against coating (see figure 5.1).

The fluorescence signal emitted upon decay of the $^1P_1$ state to the ground state at 285 nm is monitored by imaging the pulse collision volume onto the photo cathode of a photomultiplier tube (Hamamatsu, R6358) located outside the vacuum chamber. A

$f = 100$ mm lens with 22 mm clear aperture collects the fluorescence light coming from the excitation volume, 80 mm below the detection window, which is then focused through an aperture of 3 mm in diameter to reject Doppler-broadened background light. Light coming e.g. from the laser is suppressed by a combination of a color glass filter (Schott, UG11, $\mathcal{T} = 65 \pm 5$ %) and an interference filter (Asahi Spectra, MC28J3, $\mathcal{T} = 19 \pm 1$ %). With 12 ± 1 % total transmissivity of the filter combination, 23 ± 2 % quantum efficiency of the PMT at 285 nm and a solid angle of 0.04 ± 0.005 of 4π the detection efficiency amounts to $\sim 10^{-4}$.

5.2.3. Reference fs frequency comb

The ps laser system as described above provides not the whole information for an absolute frequency measurement. Only the repetition rate can directly be measured and referenced to a radio-frequency Cs clock. The spectrum of ps pulses cannot be extended to an octave, so the well established $f - 2f$ interferometer is not applicable here for the determination of the CE-frequency. For its measurement a reference fs frequency comb is used. In order to reference the ps laser a cw transfer laser oscillator (TLO), which is a cw diode laser running at around 862 nm, is phase locked to a mode of this laser while the heterodyne signal between the fs comb and the TLO is continuously measured.

The fs comb used for this purpose was described by R. Holzwarth [46]. The main part of the laser is a Kerr lens mode-locked Ti:sapphire laser emitting a pulse train at 800 MHz repetition frequency. The output of the laser is coupled into a nonlinear photonic crystal fiber to extend the spectral bandwidth to an octave. The infrared part of the spectrum is split by a dichroic mirror, frequency doubled and recombined with the blue one on a photodiode for heterodyne detection. This $f - 2f$ interferometer measures the carrier-envelope-offset frequency. A fused silica wedge at Brewster's angle inside the laser resonator is used to preset the carrier-envelope-offset frequency which is then fine tuned and stabilized via an acousto-optic modulator (AOM) by adjusting the pump power.

5.3. Results

Natural magnesium consists of a mixture of three stable isotopes ^{24}Mg, ^{25}Mg and ^{26}Mg with their natural abundances of 79 % : 10 % : 11 %. Due to the high spectral bandwidth of the pulses (several hundred GHz) all three isotopes are addressed by the laser while scanning its offset frequency. A sample spectrum is shown in figure 5.3. The two lines correspond to ^{24}Mg (right strong peak) and ^{26}Mg (left small peak). In contrast to these two isotopes ^{25}Mg exhibits a nuclear spin $I = 5/2$ which causes the excited state to split into 5 hyperfine states. All five components with their relative amplitudes of 1/3, 4/15, 1/5, 2/15 and 1/15 with respect to the unsplit FS transition are compatible with

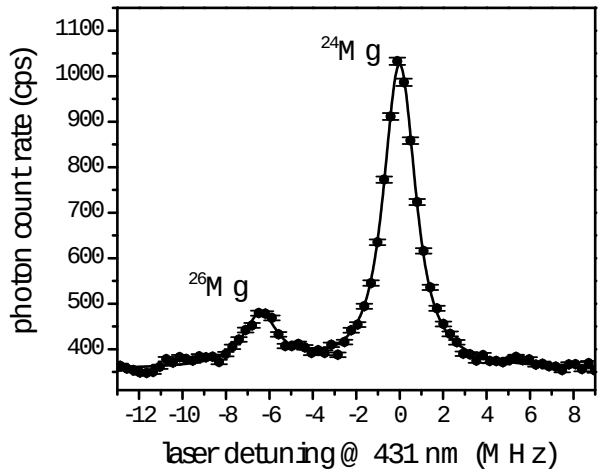

Figure 5.3.: Sample Mg spectrum showing two narrow resonances superimposed on a Doppler-broadened background. The two narrow spectral lines correspond to the isotope components ^{24}Mg and ^{26}Mg. Two Lorentzians are fitted to the data. The total acquisition times is about 23 minutes.

the two-photon selection rules (section 2.2.3). Accounting the low natural abundance of ^{25}Mg these hyperfine components fall below the detection limit and thus do not appear in the spectrum.

For the spectroscopy the laser frequency was scanned over the Mg $^1S_0(3s^2) - {}^1D_2(3s3d)$ resonance by tuning the frequency of the double pass AOM between the laser and the reference resonator. At every frequency detuning the detected count rate was integrated over 1 s. Up to 43 such successive scans over the Mg resonance constitute a measurement run with a total acquisition time of up to 1 hour. Between the runs the laser system was maintained and the Mg oven was refilled.

Prior to analyzing the data, all scans where the laser or the spectroscopy cavity dropped out of lock were discarded. Furthermore during the operation fluctuations in the atomic flux could be observed in form of bursts and drops in the recorded spectrum, which did not average out within the limited amount of scans and distorted the spectral lines. Scans containing the largest of these fluctuations were also excluded from the analysis. The remaining scans in one run were concatenated and Lorentzian functions with uniform weights were fitted to the spectrum.

5.3.1. Isotope shift ^{26}Mg - ^{24}Mg

For this measurement the FSR of the SHG cavity was set to twice the lasers repetition frequency. In this way the laser stability could be improved, as discussed above. To determine the isotope shift the frequency interval between ^{26}Mg and ^{24}Mg is expressed in terms of experimental parameters

$$\nu_{^{26}\mathrm{Mg}-^{24}\mathrm{Mg}} = (\mu_{^{26}\mathrm{Mg}} - \mu_{^{24}\mathrm{Mg}})\, 2\nu_{\mathrm{rep}} + 8\,(\nu_{\mathrm{AOM},^{26}\mathrm{Mg}} - \nu_{\mathrm{AOM},^{24}\mathrm{Mg}})\,, \tag{5.1}$$

where $\mu_{^{26}\mathrm{Mg}}$, $\mu_{^{24}\mathrm{Mg}}$ are the mode sums for the respective isotopes. The factor 8 in front of the AOM frequencies is a consequence of the double pass configuration of the AOM, SHG and two-photon absorption (each of them gives a factor 2). The difference of the mode sums $\Delta\mu = \mu_{^{26}\mathrm{Mg}} - \mu_{^{24}\mathrm{Mg}}$ can be determined either by using a theoretical or experimental reference value, which is known to better than ν_{rep} or by measuring the isotope shift with different repetition rates. The latter provides an independent measurement and is applied here. In order to use the locking system described in section 3.2.1 the repetition frequency of the ps laser should be close to a commensurate value of the FSR of the reference resonator ν_{FSR}. For this reason the isotope shift was measured with the repetition frequencies $\nu_{\mathrm{rep}}^{\mathrm{ps}} = 81.023$ MHz, $\nu_{\mathrm{rep}}^{\mathrm{ps}} = 81.834$ MHz and $\nu_{\mathrm{rep}}^{\mathrm{ps}} = 82.660$ MHz, corresponding to $\nu_{\mathrm{FSR}}/10.1$, $\nu_{\mathrm{FSR}}/10$ and $\nu_{\mathrm{FSR}}/9.9$ respectively. The mode sum difference $\Delta\mu$ was found by minimizing the difference of the calculated isotope shifts at different repetitions rates

$$\Delta\nu_{^{26}\mathrm{Mg}-^{24}\mathrm{Mg}} = \nu_{^{26}\mathrm{Mg}-^{24}\mathrm{Mg}}(\nu_{\mathrm{rep1}}) - \nu_{^{26}\mathrm{Mg}-^{24}\mathrm{Mg}}(\nu_{\mathrm{rep2}})\,. \tag{5.2}$$

The results of the isotope shift measurements are shown in figure 5.4. Every data

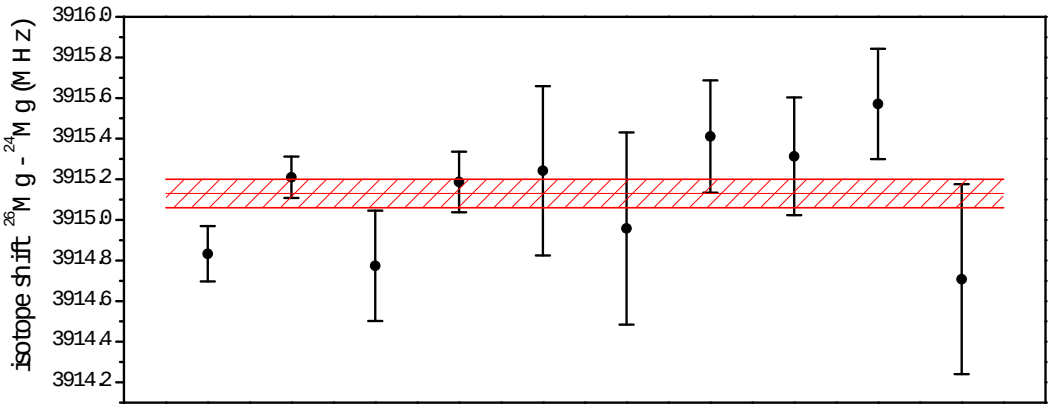

Figure 5.4.: *Isotope shifts between* ^{26}Mg *and* ^{24}Mg *for the individual runs (symbols) and wighted average with its confidence interval (striated area).*

point represents a run containing the accepted scans, as described above. Calculating a weighted average (full square in figure 5.4) yields a statistical uncertainty of 70 kHz with a reduced χ^2 per degree of freedom of 1.3. Systematic effects like the AC Stark and Zeeman shift affect both lines in the same way and thus cancel in the difference frequency measurement. The final result for the isotope shift between ^{26}Mg and ^{24}Mg is

$$\Delta\nu_{26\mathrm{Mg}-24\mathrm{Mg}} = 3915.13(7)\ \mathrm{MHz}\,.$$

This is the first reported measurement of the isotope shift of the $^1S_0(3s^2) - {}^1D_2(3s3d)$ two-photon interval in Mg. The resulting value is in agreement with the calculated theoretical value of 3.96(3) GHz as reported in [47, 48].

5.3.2. ^{24}Mg absolute frequency

For the absolute frequency determination of the $^1S_0(3s^2) - {}^1D_2(3s3d)$ two photon transition in ^{24}Mg the FSR of the SHG cavity was set to match the laser repetition frequency. The offset frequency of the spectroscopy laser was measured using the fs reference comb, as discussed above. Expressed in experimental parameters, with the mode numbers n and m of the spectroscopy and reference comb respectively, the CE-frequency reads

$$\pm\,\nu_{\mathrm{ceo}}^{\mathrm{ps}} = n \cdot \nu_{\mathrm{rep}}^{\mathrm{fs}} + \nu_{\mathrm{ceo}}^{\mathrm{fs}} \pm \nu_{\mathrm{TLO-fs}} - m \cdot \nu_{\mathrm{rep}}^{\mathrm{ps}} - \nu_{\mathrm{TLO-ps}}\,. \tag{5.3}$$

With the offset frequency given by equation (5.3) the two-photon transition frequency reads

$$\nu_\mu = \mu \cdot \nu_{\mathrm{rep}}^{\mathrm{ps}} \pm 4\nu_{\mathrm{ceo}}^{\mathrm{ps}} + 8\nu_{\mathrm{AOM}}\,. \tag{5.4}$$

Analogous to $\Delta\mu$ in section 5.3.1 the mode sum μ in equation (5.4) was determined by measuring at different repetition frequencies. The measurements were carried out in several runs containing a number of scans and the accepted scans are selected, as described above.

The spectroscopy laser was locked to the stable reference cavity but limited thermal stability may have caused this cavity to drift. On the time scale of one run (up to 1 h) this drift could be approximated by a linear function in time which was then used for absolute frequency determination. Using redundant frequency counters to monitor beat note signals, as described in [49], cycle slip events were detected and removed. For an adequate cavity drift measurement at least 50 valid reference points distributed over the whole run should be recorded. Runs which were below this threshold were discarded for absolute frequency determination.

The results for absolute frequency measurement of ^{24}Mg are summarized in figure 5.5 where every data point represents a run containing the accepted scans. The error bars are derived from the residuals of the Lorentzian functions fitted to the spectra. The scattering of the data points exceeds the statistical uncertainty obtained by calculating a weighted average ($\chi^2/\mathrm{dof} = 3.8$), what may be attributed to residual fluctuations of the Mg oven. Although the scans with the largest spikes and dips are manually rejected, some smaller ones are still present and may distort the spectral lines. This behavior changes after reloading the oven and cannot be easily quantified.

Systematic effects

A variety of effects can shift and broaden the spectral lines. While analyzing the transition line shapes these effects have to be taken into account. In the following the relevant systematics for the absolute frequency determination in Mg are discussed.

Zeeman effect In a small external magnetic field $\mathfrak{B}$ the degeneracy with respect to the magnetic quantum number m_J is lifted resulting in a splitting of the state into $2J+1$

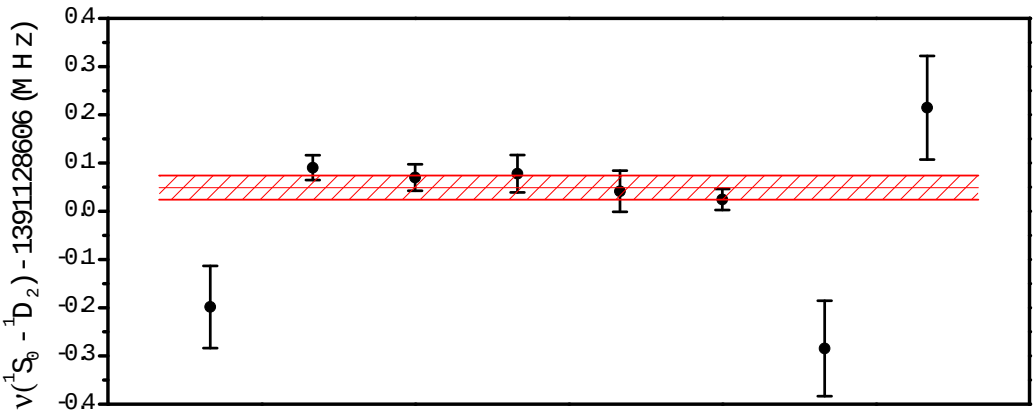

Figure 5.5.: *Absolute frequencies of the* $^1S_0(3s^2) - ^1D_2(3s3d)$ *two-photon transition in* ^{24}Mg *(full circles) and wighted average value (fullsquare).*

equidistant levels. For a field along the z-axis the frequency shift of the Zeeman levels can be written

$$\Delta\nu = m_J \mu_B g_J \mathfrak{B}/h\,, \tag{5.5}$$

where μ_B is the Bohr magnetron and g_J the Landé g-factor.

In contrast to the ground state the exited state with $J = 2$ is degenerate in m_J. In an external magnetic field the degeneracy is broken resulting in five Zeeman states corresponding to the quantum number $m_J = -2, -1, 0, 1, 2$ which appear symmetrically with respect to the non shifted line with $m_J = 0$. Setting $\mu_B = 9.3 \times 10^{-24}$ J/T and $g = 1$ the Zeeman shift calculates to ± 14 MHz/mT for $|m| = 1$ and ± 28 MHz/mT for $|m| = 2$. The left plot in figure 5.6 shows the ^{24}Mg and ^{26}Mg peaks split into two lines respectively shifted by around ± 2 MHz. This shift corresponds to a magnetic field of 71 μT for $m_J = 2$.

In the experiment there are at least two known sources for stray fields: earth's magnetic field with approximately 48 μT and the heating wire around the magnesium oven which can be approximated to 4 μT by a magnetic field of a conductor loop in 10 mm distance. The latter is by one order of magnitude smaller than earth's magnetic field. To get an accurate value for the stray fields at the excitation volume including sources beyond the two mentioned above, they are measured using a fluxgate magnetometer to ≈ 65 μT in the atomic beam direction and ≈ 20 μT in the perpendicular directions respectively. Pairs of coils are installed outside the vacuum chamber to compensate the magnetic field in all three directions. By applying a current to the coils the fields can be compensated to better than 20 μT, so an upper limit for the residual Zeeman shift can be given by ± 560 kHz.

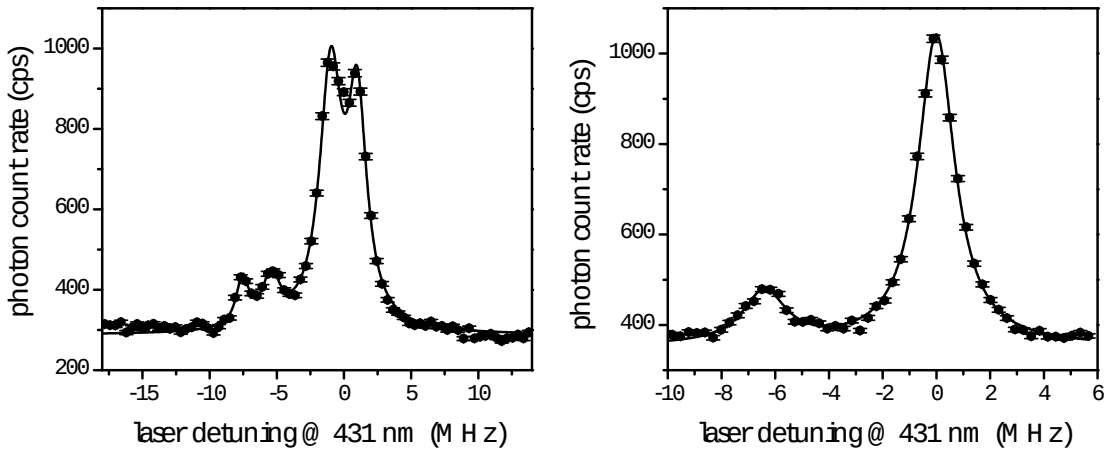

Figure 5.6.: *Magnesium spectrum before (left) and after (right) magnetic field compensation.*

Asymmetry of the spectra In general the reflectivity of mirrors is wavelength dependent. Over the small laser bandwidth of 0.2 nm the reflectivity can be approximated by a linear function. After being reflected the spectral intensity peak of the frequency comb is shifted and its intensity profile becomes asymmetric. While the asymmetry results in an asymmetric transition line, the shift of the peak of the spectral intensity profile leads to a shift of the transition line by at most the same amount.

The wavelength dependent reflectivity function can be written in the form $(1 - 3 \times 10^{-19} \times \omega)^5$. The power of 5 results from five reflections on the HR mirrors before the back propagating pulse overlaps with the forth propagating one. The slope of the linear function is extracted from the reflectivity curve of the used HR mirrors. Multiplying the intensity profile by this linear function yields a spectral intensity profile which maximum is shifted by around -500 kHz. The two-photon transition line is shifted by the same amount.

AC Stark shift The electric field of the laser which is used to probe the atomic transition is also responsible for a shift of the energy levels $\hbar\omega_i$. If all intermediate levels are off resonant with respect to a one-photon transition, the AC Stark shift can be treated in the frame of time-dependent perturbation theory and the frequency shift of a level can be expressed as [14]

$$\Delta\omega_{\mathrm{AC}}(i) = 2\pi\beta_{\mathrm{AC}}(i)\big(\mathcal{I}_1(t) + \mathcal{I}_2(t)\big) \tag{5.6}$$

where $\beta_{\mathrm{AC}}(i)$ is the dynamic Stark shift coefficient. The AC Stark shift is directly proportional to the sum of the laser intensities and cannot be suppressed in the experiment. Using the off-resonant intermediate $^1P_1$ state and with two laser beams of equal intensity

driving the transition the AC stark shift can be approximated by

$$\Delta\nu_{\mathrm{AC}} = \frac{e^2 a_0^2}{8\pi\hbar^2 c\varepsilon_0}\left(\frac{\mathfrak{p}(^1S_0 - {}^1P_1)^2}{2\,\pi\,\Delta\nu} - \frac{\mathfrak{p}(^1P_1 - {}^1D_2)^2}{2\,\pi\,\Delta\nu}\right) 2\mathcal{I}\,. \tag{5.7}$$

With the matrix elements $\mathfrak{p}(^1S_0 - {}^1P_1) = 4.03(2)$ a.u. and $\mathfrak{p}(^1P_1 - {}^1D_2) = 4.62(5)$ a.u. [50], a laser detuning $\Delta\nu = \nu_{in} - \nu_L = 355$ THz and a laser power of 860 mW per direction inside the resonator focused to 264 μm waist diameter the AC Stark shift amounts to 51 kHz. Transitions to the $^3P_1$ state involve intersystem crossings and the corresponding matrix elements are by two orders of magnitude smaller providing a contribution of less than 1Hz to the shift.

Time of flight broadening In DFCS the interaction region is limited by the pulse collision volume, i.e. by the pulse length and waist diameter. Depending on the velocity of the atoms and the dimensions of this volume the interaction time of the atoms with the laser field may be short resulting in the so called time of flight broadening. This effect can be approximated by the relation [15]

$$\omega_{\mathrm{tof}} = \sqrt{2\ln(2)}\,\frac{4v}{d}\,, \tag{5.8}$$

with d being the interaction length. In a weak focusing regime when the confocal parameter b is longer than the pulse length $l_{\mathrm{p}} = 4c\sqrt{2\,\ln(2)}/\Delta\omega$ (for Fourier limited pulses), the excitation volume can be approximated by a cylinder of diameter $2w_0$ and length l_{p}.

For collinear excitation geometry the interaction length is given by the pulse length l_{p}. Setting $\Delta\omega = \Delta k\,c$ results in a time-of-flight width $\omega_{\mathrm{tof}} = \Delta k\,v_z$, which is equal to the residual first order Doppler effect.

In perpendicular excitation geometry, however, the interaction length is given by the waist diameter and the time-of-flight width reads $\omega_{\mathrm{tof}} = \sqrt{8\ln(2)}\,v_x/w_0$ (for atoms flying in the x-direction). In the Mg measurements, with a weak focus of 264 μm waist diameter, the interaction time amounts to 0.36 μs. This causes a time of flight broadening of 2 MHz which is of same order as the natural line width.

First and second order Doppler effect During the interaction of laser radiation with the target atoms momentum and energy conservation laws must be fulfilled. Expanding the relativistic energy conservation equation to second order in $\Delta k = (k_{1,z} - k_{2,z})$ and v_z results in

$$\omega_1 + \omega_2 \approx \omega_{eg} \pm \Delta k\,v_z - \omega_{eg}\,\frac{v^2}{2c^2}\,. \tag{5.9}$$

The first term corresponds to the transition frequency $\omega_e - \omega_g$ for an atom at rest and the last two terms describe the first and second order Doppler-effect respectively, while higher order contributions are neglected.

Using two counter-propagating photons of equal frequency ($k_{1,z} = k_{2,z}$) to drive the transition, the first order Doppler shift cancels exactly. However, in frequency comb spectroscopy two photons of somewhat different frequency add up to drive the transition with $k_{1,z} \neq k_{2,z}$ resulting in a residual first order Doppler effect. Integrated over all velocities this results in a pure line broadening provided the left and right propagating combs spectra are identical. This Doppler broadening can be approximated by $\omega_{1st}^{D} = \Delta k\, v_z$. To generate an atomic beam, the Mg oven is heated to around 600 K by running 6 A through the tantalum wire. Assuming a Maxwellian velocity distribution a mean velocity of $v = \sqrt{8k_{\mathrm{B}}T/(\pi M)} = 725$ m/s can be attributed to the atoms. Due to the beam spread, the velocity in the z direction can be estimated by $v \sin\theta \sin\phi$ where $\theta = 31°$ is the maximum spread angle allowed by the aperture in front of the oven (s. figure 5.1 and $\phi = 90°$. With the laser bandwidth of 0.32 THz the residual first order Doppler broadening amounts to 63 kHz.

The second order Doppler effect is independent of the direction of the motion and shifts the line center by $\omega_{2nd}^{D} = \omega_{eg}\, v^2/(2c^2)$. With a mean velocity $v = 725$ m/s the second order Doppler shift calculates to 4 kHz. It does not cancel in two-photon spectroscopy but is proportional to v^2 and vanishes for an atom at rest.

Modulation shift In order to stabilize the spectroscopy cavity, a modulation is applied to a piezo mounted mirror. The error signal is generated by analyzing the transmitted signal in a lock-in-amplifier allowing for a small modulation amplitude. Applying a sinusoidal modulation with of 96 kHz frequency and a maximum displacement of the mirror of 0.35 nm the Doppler shift amounts to 2 kHz.

Final result

For given experimental conditions systematic effects discussed in the previous paragraphs exceed the statistical uncertainty from the average calculation by far yielding an overall uncertainty of ≈ 0.59 MHz. That is by three orders of magnitude smaller than previous measurements [51]. After correcting the value for the AC Stark shift and the asymmetry shift the final result for the absolute frequency of the ${}^1S_0 - {}^1D_2$ two-photon transition in ^{24}Mg is

$$\nu_{{}^1S_0 \to {}^1D_2} = 1391128606.50(59)\ \mathrm{MHz}\,.$$

This value is in excellent agreement with the one from ref. [51] of 1391128.9(6) GHz, but 1000 times more accurate.

6. Prospects for spectroscopy at the fourth harmonic: H $1S-3S$

This chapter reports on the prospects to measure the $1S-3S$ two-photon interval in H at 205 nm. This measurement will extend Doppler-free DFCS into the DUV wavelength region and pave the way for spectroscopy in the XUV.

The $1S-3S$ interval in combination with the well known $1S-2S$ frequency is a promising candidate for tests of bound state QED. Furthermore using this combination a value for the proton charge radius can be extracted. As will be discussed below, recent measurements of the Lamb shift in muonic hydrogen [10] led to a value for the proton charge radius which is 10 times more accurate but 5 standard deviations away from the recommended value by CODATA. The origin of this deviation is not clear yet and further investigations are needed. DFCS of the $1S-3S$ two-photon transition in hydrogen may contribute to the clarification of the discrepancy in the proton charge radius.

6.1. The hydrogen atom and the Rydberg constant

Hydrogen has a particular significance in testing and improving fundamental theories. Due to its simplicity elaborate calculations can be carried out providing very precise predictions while its experimental accessibility allows for measurements with very high accuracies. Accurate measurements in hydrogen carried out by W. E. Lamb and R. Retherford, for example, revealed a small deviation between theory and experiment, which is today known as the Lamb shift. This finding led to a paradigm shift in the physics and in its course to a development of the today well established quantum electrodynamics (QED), which is one of the best tested theories at present.

Since a theory can never be proven to be right, but one experiment is enough to disprove it, experiments with even higher accuracies are required. Since decades the narrow $1S-2S$ resonance in hydrogen is analyzed in our group. Its value has been measured with an astounding accuracy of 1.4 parts in 10^{14} [52] allowing to test QED at a very high level.

6.1.1. Energy levels

One of the simplest approaches to calculate the energy levels is the non relativistic Schrödinger equation for an electron in a Coulomb potential of an infinitely heavy nucleus. For hydrogen and hydrogen-like atoms this equation can be solved exactly giving the eigenvalues

$$\mathfrak{E}_{\mathrm{S}}(n) = R_\infty hc\,\frac{Z^2}{n^2}\,. \tag{6.1}$$

This energy spectrum scales with the Rydberg constant $R_\infty = m_e e^4/(8\varepsilon_0^2 h^3 c)$, where m_e is the electron mass, e the elementary charge, and $Z = 1$ (for H) the nuclear charge and the inverse principal quantum number n. Precise experimental results soon revealed deviations from the simple theoretical model in equation (6.1) in form of level shifts and splittings. The Dirac theory was able to explain the fine structure (FS) splitting which is due to the relativistic nature of electrons and the spin-orbit interactions providing the Dirac energies $\mathfrak{E}_{\mathrm{DR}}$. After the proposal of the existence of a small nuclear magnetic moment also the hyperfine structure (HFS) could be explained providing a correction term $\mathfrak{E}_{\mathrm{HFS}}$ to the Dirac energies. Finally, with the development of QED the previously observed Lamb shifts $\mathfrak{E}_{\mathrm{LS}}$ could be explained and calculated. With this findings the energy levels of an atom can be written as a sum of three terms:

$$\mathfrak{E} = \mathfrak{E}_{\mathrm{DR}}(n,j) + \mathfrak{E}_{\mathrm{HFS}}(n,l,j) + \mathfrak{E}_{\mathrm{LS}}(n,l,j)\,. \tag{6.2}$$

In figure 6.1 the energy levels for hydrogen according to the simple Bohr model (as given by equation (6.1)), the Dirac theory, including the Lamb shift and HFS, are shown.
In the following the several energy components in equation (6.2) will be discussed in more detail.

Dirac-Coulomb energies

The fully relativistic Dirac wave equation for particles with spin 1/2 in the approximation of a particle in the field of an infinitely heavy Coulomb center is given by

$$\left[\frac{p^2}{2m_e} - \frac{p^4}{8m_e^3c^2} + V - \frac{\hbar^2}{8m_e^2c^2}\left(\frac{2}{r}\frac{\mathrm{d}V}{\mathrm{d}r} - \frac{\mathrm{d}^2V}{\mathrm{d}r^2}\right) + \frac{\hbar^2}{2m_e^2c^2}\frac{1}{r}\frac{\mathrm{d}V}{\mathrm{d}r}\boldsymbol{L}\cdot\boldsymbol{S}\right]\psi = \mathfrak{E}\psi\,, \tag{6.3}$$

where $V = Ze^2/r$ and $\boldsymbol{L}$, $\boldsymbol{S}$ the angular momentum and the spin operator respectively. This Dirac equation can be solved exactly providing an energy spectrum for hydrogen and hydrogen-like atoms including the fine structure splitting [53]

$$\mathfrak{E}(n,j) = m_e c^2\left[f(n,j) - 1\right]\,, \tag{6.4}$$

$$f(n,j) = \left[1 + \frac{(Z\,\alpha)^2}{\left(n - j - (1/2) + \sqrt{(j+1/2)^2 - (Z\,\alpha)^2}\,\right)^2}\right]^{-1/2}\,,$$

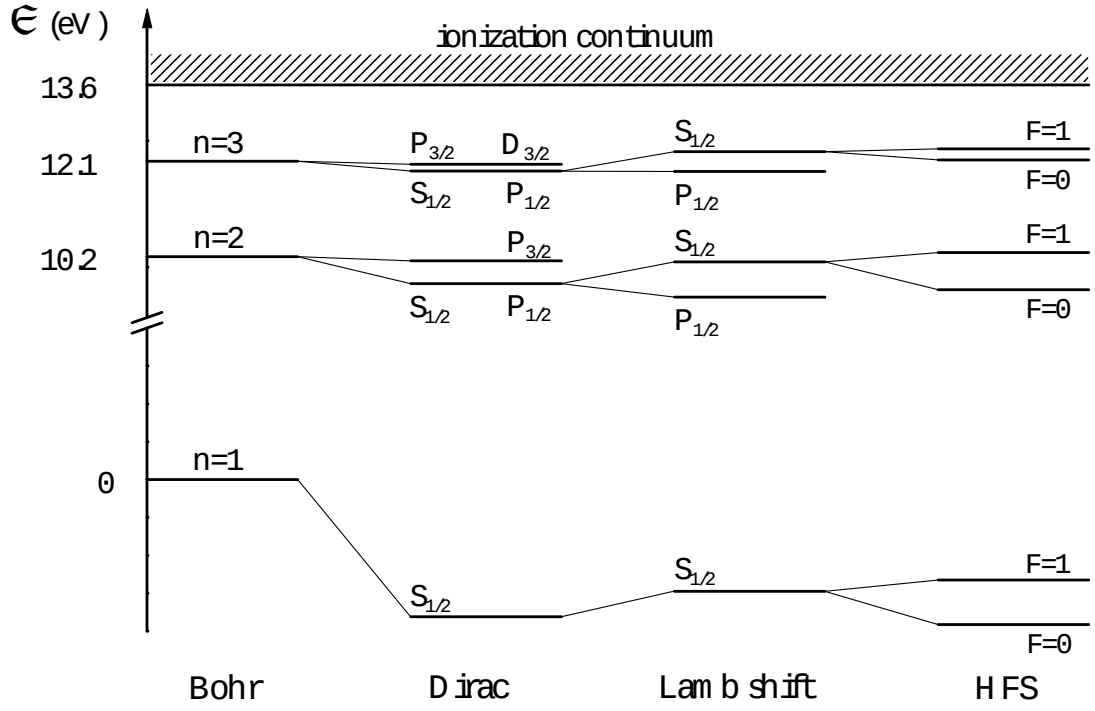

Figure 6.1.: *Hydrogen level diagram for states $n \leq 3$ according to Bohr and Dirac theory, including Lamb shift and hyperfine structure. For the sake of clarity the Lamb shift is only plotted for states with $j = 1/2$ and HFS only for S states. The energy states are drawn not to scale.*

where α is the fine structure constant. Due to the dependence of the energies on the total angular momentum j, the levels with the same principal quantum number n but different j split into n components, corresponding to the fine structure splitting.

To take the finite mass m_N of the nucleus and its motion into account, the Schrödinger theory can be modified by simply substituting the electron mass by the reduced mass $m_r = m_e\, m_N/(m_e + m_N)$. In the Dirac theory a closed solution with correct mass dependence cannot be given, but can be approximated. Based on the Breit equation for two spin 1/2 particles of different mass and charge the Hamiltonian can be written in the form [53]

$$(H_0 + H_1 + H_2 + H_3 + H_4 + H_5)\,\psi = \mathfrak{E}\psi\,, \tag{6.5}$$

where H_0 is the ordinary non relativistic Hamiltonian, H_1 is the relativistic correction to the kinetic energy, H_2 is the correction to the interaction between the particles, H_3 is the spin-orbit interaction term, H_4 is the so-called Darwin term and H_5 comprises the spin of the nucleus. Expanding the Hamiltonian in equation (6.5) to first order of the

small parameter m_e/m_N results in the simplified Hamiltonian [53]

$$(H_a + H_b + H_c)\,\psi = \mathfrak{E}\psi \tag{6.6}$$

with

$$H_a = \frac{p^2}{2m_r} + V - \frac{p^4}{8m_r^3c^2} - \frac{\hbar^2}{8m_r^2c^2}\left(\frac{2}{r}\frac{\mathrm{d}V}{\mathrm{d}r} - \frac{\mathrm{d}^2V}{\mathrm{d}r^2}\right) + \frac{\hbar^2}{2m_r^2c^2}\frac{1}{r}\frac{\mathrm{d}V}{\mathrm{d}r}\boldsymbol{L}\cdot\boldsymbol{S}_1\,,$$
$$H_b = \frac{1}{m_Nc^2}\left[\frac{3p^4}{8m_e^2} - \frac{(p^2+p_r^2)}{2m_e}V + \frac{\hbar^2}{8m_e^2c^2}\left(\frac{2}{r}\frac{\mathrm{d}V}{\mathrm{d}r} - \frac{\mathrm{d}^2V}{\mathrm{d}r^2}\right)\right]\,,$$

$$H_c = \frac{Ze^2\hbar^2}{m_em_Nc^2}\left[\frac{8\pi}{3}(\boldsymbol{S}_1\cdot\boldsymbol{S}_2)\delta^{(3)}(\boldsymbol{r}) - \frac{1}{r^3}\left(\boldsymbol{S}_1\cdot\boldsymbol{S}_2 - \frac{3\,(\boldsymbol{S}_1\cdot\boldsymbol{r})(\boldsymbol{S}_2\cdot\boldsymbol{r})}{r^2}\right)\right] - \frac{\hbar^2}{m_em_Nc^2}\frac{Ze^2}{r^3}\boldsymbol{L}\cdot\boldsymbol{S}_2\,,$$

where $\boldsymbol{S}_1$ and $\boldsymbol{S}_2$ are the spin operators of the two particles, separated by the distance r, p is the momentum and $\delta^{(3)}(\boldsymbol{r})$ is the three-dimensional Dirac delta function. H_a is exactly the same as in equation (6.3) but with the reduced mass instead of the electron mass. H_b is a correction term to the non relativistic energies and acts only on n but not on l or j and hence shifts only the energy levels but does not contribute to the fine structure splitting. H_c contains all the terms which involve the nuclear spin. It explains the hyperfine splitting of the energy levels and will be treated in the next paragraph. The expectation value of the Hamiltonian (6.6), while setting $H_c = 0$, corresponds to the Dirac energies of the hydrogen and hydrogen like atoms that approximately take into account the finite mass of the nucleus

$$\mathfrak{E}_{\mathrm{DR}}(n,j) = R_\infty\frac{2h}{\alpha^2}\left[\frac{m_r}{m_e}\,c\left(f(n,j)-1\right) - \frac{m_r^2\,c}{2m_e\,(m_e+m_N)}\left(f(n,j)-1\right)^2\right]. \tag{6.7}$$

Hyperfine structure

The degeneracy of the energy states with respect to the direction of the total angular momentum j, which is present in the Dirac theory, is lifted for an atom in an external field or if the nucleus exhibits a magnetic moment $\boldsymbol{\mu}$, and indeed many nuclei do have a non-zero magnetic moment. Because of its inverse mass dependence $\boldsymbol{\mu} \propto m_N^{-1}$, the nuclear magnetic moment is roughly three orders of magnitude smaller than the magnetic moment of the electron, consequently the hyperfine splitting is by the same order of magnitude smaller than the fine structure and can be treated as a small perturbation. The splitting of the ground state for example amounts to 1.42 GHz, corresponding to the well known 21 cm line which is important for radio astronomy.

To calculate the splitting of the energy levels due to the nuclear magnetic moment the expectation values of the Hamiltonian in equation (6.6) are calculated. These values provide the zero order contributions to the HFS

$$\mathfrak{E}_{\mathrm{HFS}}(n,l,j) = R_\infty \frac{Z^3\alpha^2 g\, c}{n^3}\,\frac{m_e}{m_N}\,\frac{F(F+1)-I(I+1)-j(j+1)}{j(j+1)(2l+1)}\,, \tag{6.8}$$

and depend on the orbital l and total angular momentum j, nuclear spin I, the total atomic angular momentum $F = \{(j+I), \ldots, |j-I|\}$ and the Landé factor g. Higher order QED correction terms to equation (6.8) can be included in form of a multiplying factor $(1 + Q_{\mathrm{QED}})$. For the ground state the QED correction terms Q_{QED} can be found e.g. in ref. [54].

Lamb shift

Contributions to the atomic energy levels beyond the Dirac energy and hyperfine splitting belong to the Lamb shift. They can be classified into basically three categories, radiative, recoil, and nuclear size and structure correction terms which can be expressed as power series expansions in the three small parameters α, $Z\alpha$ ($Z \ll 1/\alpha$) and m_e/m_N.

Radiative corrections Radiative correction terms yield by far the largest contribution to the Lamb shift and scale with the parameters α and $Z\alpha$. They are made up of the electron self-energy, describing the effect of emission and re-absorption of virtual photons, and vacuum polarization, describing a creation and annihilation of a virtual electron-positron pair by the background electromagnetic field. Considering up to three-loop corrections the energy shift for the S states reads [55]

$$\begin{aligned}\Delta\mathfrak{E}_{\mathrm{radiative}} = \frac{(Z\alpha)^4\, m_e c^2}{n^3}\left(\frac{m_r}{m_e}\right)^3 \Bigg[&\left(\frac{\alpha}{\pi}\right) F_1(Z\alpha) + \left(\frac{\alpha}{\pi}\right) H(Z\alpha) \\ &+ \left(\frac{\alpha}{\pi}\right)^2 F_2(Z\alpha) + \left(\frac{\alpha}{\pi}\right)^3 F_3(Z\alpha) - \frac{4}{15}\left(\frac{\alpha}{\pi}\right)\left(\frac{m_e}{m_\mu}\right)^2 - 0.179\left(\frac{\alpha}{\pi}\right)\left(\frac{m_e}{m_\mu}\right)^2\Bigg],\end{aligned} \tag{6.9}$$

with

$$\begin{aligned}F_1(Z\alpha) &= A_{41}L + A_{40} + (Z\alpha)\,A_{50} + (Z\alpha)^2\left(A_{62}L^2 + A_{61}L + G_{\mathrm{SE}}(Z\alpha)\right),\\ H(Z\alpha) &= V_{40} + (Z\alpha)\,V_{50} + (Z\alpha)^2\left(V_{61}L + G^{(1)}_{\mathrm{VP}}(Z\alpha) + G^{(R)}_{\mathrm{VP}}(Z\alpha)\right),\\ F_2(Z\alpha) &= B_{40} + (Z\alpha)\,B_{50} + (Z\alpha)^2\left(B_{63}L^3 + B_{62}L^2 + B_{61}L + B_{60}\right) + \ldots,\\ F_3(Z\alpha) &= C_{40} + (Z\alpha)\,C_{50} + \ldots,\\ L &= \ln\left(\frac{m_e}{m_r}(Z\alpha)^{-2}\right).\end{aligned}$$

The coefficients A_{xy}/V_{xy}, B_{xy} and C_{xy} stand for one-, two- and three-loop corrections respectively, where the index x gives the order of the parameter $(Z\alpha)$ and y the order of L. The functions $G_{\mathrm{SE}}(Z\alpha)$, $G^{(1)}_{\mathrm{VP}}(Z\alpha)$ and $G^{(R)}_{\mathrm{VP}}(Z\alpha)$ comprise higher order contributions and are listed in [55]. For the ground state $(1S)$ the radiative corrections sum up to an energy shift of $\sim 8\,169.2$ MHz.

Recoil corrections In the framework of the effective Dirac equation (6.6) an approximative solution for the energies with exact mass dependence was given by means of the reduced mass factor. Additional contributions which cannot be expressed with the help of the reduced mass are the so called recoil corrections and scale with the parameters $Z\alpha$ and m_e/m_N. Recoil corrections of order $(Z\alpha)^4$ resulting from the effective Dirac equation and omitted in the solution (6.7) provide an energy shift for $l \neq 0$ states

$$\frac{(Z\alpha)^4 m_r^3 c^2}{2n^3 m_N^2} \left(\frac{1}{j+1/2} - \frac{1}{l+1/2}\right) (1-\delta_{l0})\,. \tag{6.10}$$

Higher order corrections for the S states reflect the truly relativistic two-body nature of the system and sum up to [56]

$$\begin{aligned}\Delta\mathfrak{E}_{\mathrm{recoil}} = \frac{m_r^3}{m_e m_N}\frac{(Z\alpha)^5 c^2}{\pi n^3}\Bigg\{&\frac{1}{3}\delta_{l0}\ln\left((Z\alpha)^{-2}\right) - \frac{8}{3}\ln\left(k_0(n,l)\right) - \frac{1}{9}\,\delta_{l0} \\ &+ \frac{7}{3}\left[2\left(\ln\left(\frac{2}{n}\right) + \sum_{k=1}^{n}\frac{1}{k} - \frac{1}{2\,n} + 1\right)\delta_{l0} - \frac{1-\delta_{l0}}{l(l+1)(2l+1)}\right] \\ &- \frac{2}{m_N^2 - m_e^2}\,\delta_{l0}\left[m_N^2\ln\left(\frac{m_e}{m_r}\right) - m_e^2\ln\left(\frac{m_N}{m_r}\right)\right]\Bigg\} \\ &+ \frac{(Z\alpha)^6 c^2}{n^3}\frac{m_e^2}{m_N}\left(4\ln(2) - \frac{7}{2}\right) - \frac{11}{15}\frac{(Z\alpha)^7 c^2}{\pi n^3}\frac{m_e^2}{m_N}\left(\ln(Z\alpha)\right)^2\,.\end{aligned} \tag{6.11}$$

The total energy shift of the ground state due to recoil effects amount to ~ 2.4 MHz and is by three orders of magnitude smaller than the radiative correction term.

Nuclear size and structure corrections Effects of weak and strong interactions are subsumed in the nuclear size and structure correction terms that depends on the proton charge radius. The corresponding energy shift is [55]

$$\begin{aligned}\Delta\mathfrak{E}_{\mathrm{Nucleus}} = \frac{2}{3}\frac{(Z\alpha)^4\,c^4}{n^3\,\hbar^2}\,m_r^3\,r_p^2\Bigg\{&1 - C_\eta\,\frac{Z\alpha\,c}{\hbar}\,m_r\,r_p + \left(4\,\ln(2) - \frac{23}{4} + \frac{3}{4}\right)\alpha\,(Z\alpha) \\ &- \left[\ln\left(\frac{Z\alpha\,c}{n\,\hbar}\,m_r\,r_p\right) + \psi(n) + \gamma - \frac{(5n+9)(n-1)}{4n^2} - C_\theta\right](Z\alpha)^2\Bigg\}\,.\end{aligned} \tag{6.12}$$

where r_p is the root-mean-square (rms) proton charge radius and the values for the constants C_η and C_θ for hydrogen are $C_\eta = 1.7(1)$ and $C_\theta = 0.47(4)$. The corresponding shift amounts to ~ 1.2 MHz. The uncertainty of this correction limits the comparison between experiment and theory to about 10^{-12}.

6.1.2. Determination of fundamental constants

The energies given by the Dirac theory in equation (6.7) and the HFS splitting given by equation (6.8) scale with the Rydberg constant R_∞. The value for this constant can be obtained experimentally by high resolution spectroscopy in hydrogen and hydrogen like atoms. The most precise spectroscopic measurement is carried out on the $1S - 2S$ two-photon transition in hydrogen. This dipole forbidden transition with a natural line width of 1.3 Hz has been measured with an accuracy of 1.4 parts in 10^{14} [57]. To extract the value for the Rydberg constant from this measurement, equation (6.2) can be rewritten in the form

$$\nu_{1S-2S} = R_\infty \left[\mathfrak{e}\left(2, 1/2, \alpha, \frac{m_N}{m_e}\right) - \mathfrak{e}\left(1, 1/2, \alpha, \frac{m_N}{m_e}\right) \right] + \mathfrak{E}_{\mathrm{LS}}(2S) - \mathfrak{E}_{\mathrm{LS}}(1S)\,, \quad (6.13)$$

where $\mathfrak{e}(n, j, \alpha, m_N/m_e)$ is the Dirac term, scaling with R_∞ and ν_{1S-2S} is the centroid frequency, so the HFS is included here. Using calculated values for the $1S$ and $2S$ Lamb shifts, $\mathfrak{E}_{\mathrm{LS}}(1S) = 8\,172.816(10)(32)$ MHz [58] and $\mathfrak{E}_{\mathrm{LS}}(2S) = 1\,045.005(1)(4)$ MHz respectively, the accuracy of the Rydberg constant is limited by the uncertainties of the computed Lamb shifts rather than by the 34 Hz uncertainty of the $1S - 2S$ transition. Using a combination of different frequency intervals in hydrogen and deuterium and utilizing the $1/n^3$ scaling law for the nS Lamb shifts the value for the Rydberg constant and the ground state Lamb shift can be calculated. With all available measured frequencies summarized by the CODATA (Committee on Data for Science and Technology) the value for the Rydberg constant and the ground state Lamb shift calculate to [55, 59]:

$$R_\infty = 10\,973\,731.568\,527(73)\ \mathrm{m}^{-1}\,,$$
$$\mathfrak{E}_{\mathrm{LS}}(1S)/h = 8\,172.837(26)\ \mathrm{MHz}$$

The largest contributions to the nuclear size and structure corrections of S states which depend on the rms proton charge radius scale with $1/n^3$. Utilizing this law the rms proton charge radius cancels and the difference $\Delta_n = n^3\,\mathfrak{E}_{\mathrm{LS}}(nS) - \mathfrak{E}_{\mathrm{LS}}(1S)$ can be calculated with a high precision. The accuracy of the values for the Rydberg constant and the ground state Lamb shift are thus limited by the complementary measurements whose relative uncertainties are of order 10^{-11}.

From the measured Lamb shift, finally, the rms proton charge radius can be calculated to $r_p = 0.8765(80)$ fm [59] with a relative uncertainty of 1 %. Figure 6.2 shows an

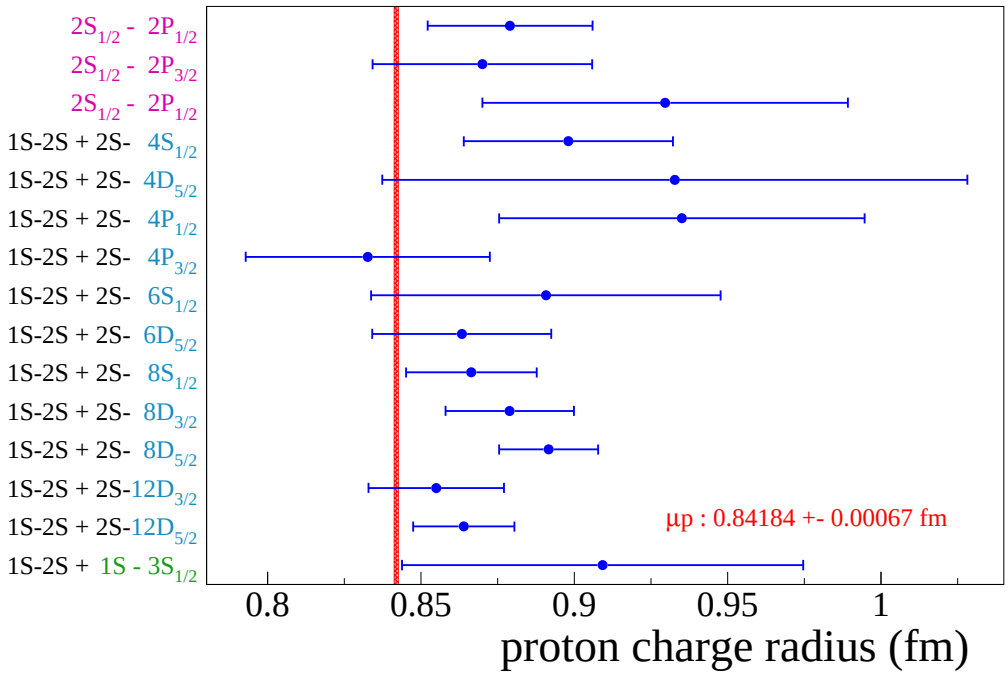

Figure 6.2.: *Overview of the proton charge radii extracted from different measured frequency intervals in hydrogen (blue data points). The red line indicates the proton charge radius extracted from Lamb shift measurements in muonic hydrogen. Courtesy of F. Biraben [60].*

overview of proton charge radii extracted from different measured frequency intervals in hydrogen. The red line indicates the proton charge radius obtained from Lamb shift measurements in muonic hydrogen $r_p = 0.84184(67)$ fm [10], while the width of the line reflects the uncertainty of the value. This value is 10 times more precise than the recommended value by CODATA ($r_p = 0.8768(69)$ fm) but 5 standard deviations smaller and the origin of this discrepancy is not clarified yet. The CODATA value is obtained from adjustment calculations taking all measured frequency intervals in hydrogen and deuterium into account and is basically an averaged value. This procedure assumes, however, that the uncertainties of the measured values are statistical and no systematic errors are present. All frequency intervals from the $2S$ state to higher S, P and D states and the $1S - 3S$ interval are measured by the same group using basically the same apparatus. Thus unknown systematic uncertainties may be present throughout in all this measurements and may probably explain the discrepancy in the proton charge radius.

To clarify the discrepancy, independent high precision measurements in hydrogen are required. Transitions from the ground state, as e.g. the $1S - 3S$ interval, benefit from the high particle density and lower systematic effects compared to transitions from the

Table 6.1.: *Quantities for the least squares calculation of the values for the Rydberg constant and the ground state Lamb shift considering only the $1S-2S$ and $1S-3S$ intervals in hydrogen.*

constant	value
speed of light c (m/s) [55]	299 792 458
fine-structure constant α [55]	$7.297\,352\,537\,6(50)\times10^{-3}$
proton-electron mass ratio m_p/m_e [55]	1 836.152 672 47(80)
frequency interval	**value**
ν_{1S-2S} (Hz) [57]	2 466 061 413 187 074(34)
ν_{1S-3S} (Hz) [62]	2 922 743 278 678 000
Lamb shift relations	**value**
$\Delta_2 = 8\,\mathfrak{E}_{\mathrm{LS}}(2S)/h - \mathfrak{E}_{\mathrm{LS}}(1S)/h$ (Hz) [63]	187 225 700(50)
$\Delta_3 = 27\,\mathfrak{E}_{\mathrm{LS}}(2S)/h - \mathfrak{E}_{\mathrm{LS}}(1S)/h$ (Hz) [63]	235 070 900(70)
$\mathfrak{E}_{\mathrm{LS}}(2S-2P)$ (kHz) [58]	1 057 842(4)
$\mathfrak{E}_{\mathrm{LS}}(2P)$ (kHz) [64]	−12 835 990(80)

metastable $2S$ state. Thus H $1S-3S$ emerges to be a good candidate for this purpose and for further test of bound state QED.

To calculate the impact of a H $1S-3S$ measurement in combination with the $1S-2S$ value on the accuracy of the Rydberg constant and the ground state Lamb shift, the method of least-squares [61] is used. For reasons discussed above, all other measured transitions to higher states are omitted. This calculation provides the actually required accuracy of the $1S-3S$ transition frequency for a significant improvement in the values of the Rydberg constant and the ground state Lamb-shift with respect to the accuracies obtained accounting for all measured frequency intervals in H and D. In table 6.1 the relevant quantities for the adjustment are summarized. The transition frequencies are given as centroid frequencies so the HFS is accounted for. While the values of the $1S-2S$ and $1S-3S$ interval are measured ones, the Lamb shifts $\mathfrak{E}_{\mathrm{LS}}(2S-2P)$, $\mathfrak{E}_{\mathrm{LS}}(2P)$ and differences Δ_2, Δ_3 are all calculated values.

Starting with a set of linear equations written in the form $\mathcal{A}\times\mathcal{X}=\mathcal{B}$ with

$$\mathcal{A}=\begin{pmatrix} -1 & 1 & 0 & \mathfrak{e}(2,1/2,\alpha,m_N/m_e)-\mathfrak{e}(1,1/2,\alpha,m_N/m_e)\\ -1 & 0 & 1 & \mathfrak{e}(3,1/2,\alpha,m_N/m_e)-\mathfrak{e}(1,1/2,\alpha,m_N/m_e)\\ -1 & 8 & 0 & 0\\ -1 & 0 & 27 & 0\\ 0 & 1 & 0 & 0 \end{pmatrix},$$

$$\mathcal{X} = \begin{pmatrix} \mathfrak{E}_{\mathrm{LS}}(1S) \\ \mathfrak{E}_{\mathrm{LS}}(2S) \\ \mathfrak{E}_{\mathrm{LS}}(3S) \\ R_\infty \end{pmatrix} \qquad \text{and} \qquad \mathcal{B} = \begin{pmatrix} \nu_{1S-2S} \\ \nu_{1S-3S} \\ \Delta_2 \\ \Delta_3 \\ \mathfrak{E}_{\mathrm{LS}}(2S-2P) + \mathfrak{E}_{\mathrm{LS}}(2S) \end{pmatrix},$$

the values for the Rydberg constant and the $1S$, $2S$ and $3S$ Lamb shifts are obtained by solving the normal equations

$$\mathcal{D}^{-1} \times \mathcal{G} = \mathcal{X}\,.$$

The components of $\mathcal{D}$ and $\mathcal{G}$ are defined by $d_{jj'} = \sum_i a_{ij}a_{ij'}/\sigma_i$ and $g_j = \sum_i a_{ij}b_i/\sigma_i$ with $i = \{1,\ldots,5\}$ and $j,j' = \{1,\ldots,4\}$, where a_{ij} and b_i are the components of $\mathcal{A}$ and $\mathcal{B}$ respectively and σ_i are the uncertainties of b_i. The uncertainties of the calculated values of R_∞, $\mathfrak{E}_{\mathrm{LS}}(1S)$, $\mathfrak{E}_{\mathrm{LS}}(2S)$ and $\mathfrak{E}_{\mathrm{LS}}(3S)$ are given by the square root of the diagonal elements of matrix $\mathcal{D}^{-1}$.

To explore the influence of the $1S-3S$ measurement, the uncertainties of the adjusted values are calculated as functions of $\Delta\nu_{1S-3S}$. Figure 6.3 shows the results for the ground state Lamb shift (left plot) and the Rydberg constant (right plot). The

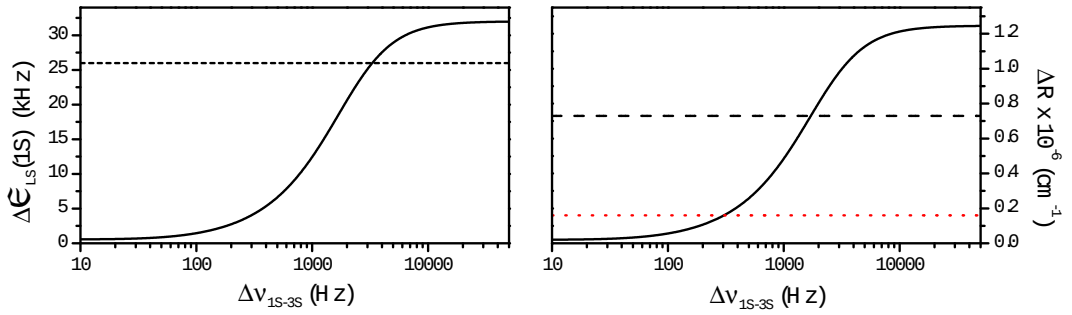

Figure 6.3.: *Solid lines: Impact of a $1S-3S$ measurement on the accuracy of the values for $\mathfrak{E}_{\mathrm{LS}}(1S)$ (left plot) and R_∞ (right plot). Calculations are carried out accounting only for the $1S-2S$ and $1S-3S$ two-photon intervals in H. Dashed lines: Current uncertainties in the $1S$ Lamb shift [59] and the Rydberg constant value [55] accounting for all measured frequency intervals in H and D. Dotted line: Uncertainty of the Rydberg constant value calculated using the more accurate proton charge radius obtained from the Lamb shift measurements in muonic hydrogen [10].*

uncertainty for R_∞ of 0.73×10^{-6} cm^{-1} [55], and for $\mathfrak{E}_{\mathrm{LS}}(1S)$ of 26 kHz, obtained from an adjustment calculation accounting for all available measured frequency intervals in hydrogen and deuterium, are indicated by dashed lines. The dotted line indicates the uncertainty of 0.16×10^{-6} cm^{-1} of the Rydberg constant values calculated using $r_p = 0.84184(67)$ fm [10]. From figure 6.3 it appears that for a significant improvement

in the accuracy of at least the ground state Lamb shift the $1S-3S$ two-photon interval must be measured within 1 kHz or better. This means that the line center must be measured at least with an accuracy of 0.1 % of the natural line width of 1 MHz. This is a very ambitious goal and demands an excellent understanding of the line shape. Up to now the best reported value for this frequency interval is $\nu_{1S-3S} = 2\,922\,743\,278.678(13)$ MHz [62] but the achieved accuracy is not sufficient for this purpose.

A successful measurement of the $1S-3S$ interval in hydrogen will provide an independent high precision measurement which, in combination with the $1S-2S$ transition frequency, will probably shed light on the origin of the discrepancy in the proton charge radius.

6.2. Design of the apparatus

DFCS on H $1S-3S$ is carried out using the laser system described in chapter 3. The fourth harmonic of the stabilized Ti:sapphire laser is directed into a spectrometer shown in figure 6.4. The vacuum chamber consists of three parts connected via tubes, which

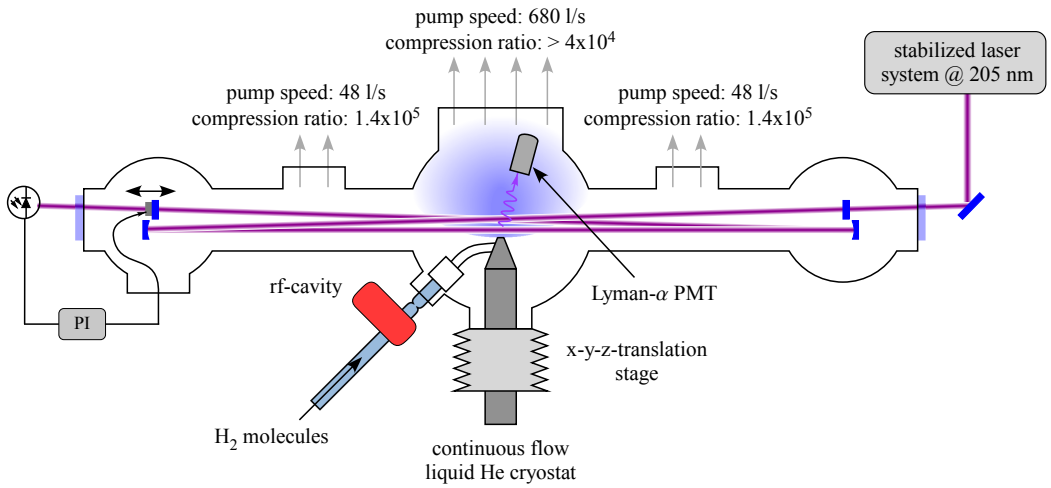

Figure 6.4.: *Spectrometer for hydrogen $1S-3S$ spectroscopy. It contains the enhancement resonator for 205 nm wavelength, the atomic hydrogen gas feed through, the copper nozzle attached to a cryostat to form a cold atomic hydrogen beam and to direct the atoms through the excitation volume perpendicular to the laser propagation direction, and the detection scheme. The compression ratios are given for H_2 molecules.*

allow to attach two additional small pumps for differential pumping and is evacuated to 10^{-6} mbar during operation. All three chambers have a breadboard inside to hold the linear enhancement resonator for the spectroscopy. These breadboards are directly

connected to the optical table and via bellows to the surrounding vacuum chamber to attenuate vibrations coming e.g. from the pumps. The central chamber features a gas feed through to supply the hydrogen atoms to the interaction volume, a cryostat holding a copper nozzle to form a cold atomic beam, and the detection optics for the Lyman- and Balmer-α fluorescence photons (see figure 6.4). In the following the spectroscopy cavity, cold atomic hydrogen beam and detection apparatus are described in detail.

6.2.1. Linear spectroscopy cavity

For spectroscopy a linear enhancement resonator is built around the hydrogen beam inside the spectrometer. Its free spectral range FSR $= \nu_{\mathrm{rep}}/2$ ensures that two counter-propagating photons overlap at the center of the cavity. Two focusing mirrors with 900 mm radius of curvature generate an almost spherical 91 μm focus. The maximum possible enhancement is limited by the best available mirrors with 98.5 % reflectivity and the 1 % absorption and scattering losses of the input coupler. Figure 6.5 shows

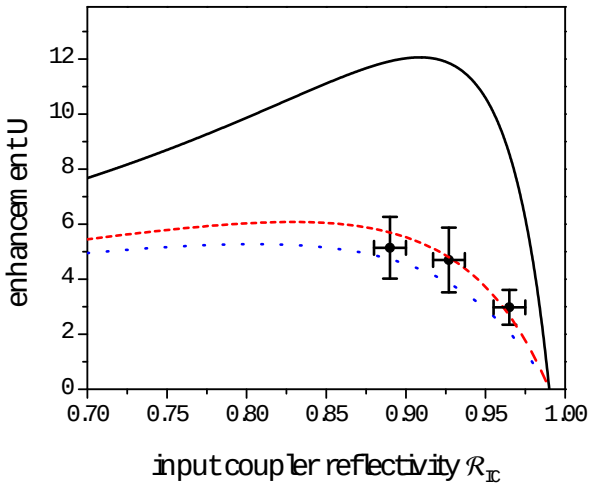

Figure 6.5.: *Enhancement of the linear spectroscopy cavity at 205 nm as a function of the input coupler reflectivity. (Solid line): theoretical enhancement for a resonator in vacuum ($\tau_{\mathrm{vac}} = 1$); (dotted blue line): theoretical enhancement of a resonator in air ($\tau_{\mathrm{air}} = 0.89$); (symbols) measured enhancement of the resonator in air for the particular input coupler; (dashed red line): fit to measured data according equation* (3.10) *providing* $\tau_{\mathrm{air}} = 91$ %.

the calculated and measured enhancement as a function of the input coupler reflectivity. For a resonator in vacuum (solid black line) the maximum theoretical enhancement is $U = 12$ with an input coupler reflectivity of 91 %.

In air the 205 nm light experiences additional losses caused by absorption of the UV light by oxygen and water vapor. With the absorption coefficients $\alpha(O_2) = 3.2 \times 10^{-4}$ cm^{-1} and $\alpha(H_2O) = 5 \times 10^{-4}$ cm^{-1} [65] and a fractional amount of 21 % and 1.3 % of oxygen and water vapor respectively, the maximum enhancement is reduced to $U = 5.5$ with an input coupler reflectivity of 84 % (dotted blue line in figure 6.5). By measuring the enhancement for three particular input couplers (plotted as symbols in figure 6.5) the air transmissivity is determined experimentally to be $\tau_{\mathrm{air}} = 91(1)$ % which is in good agreement with the theoretical value. The optimum input coupler

for the resonator in vacuum is found to have ≈ 92 % reflectivity. Since the resonator at 205 nm is pre-aligned in air, one has to keep in mind that absorption reduces the enhancement of the cavity. Evacuating the chamber provide the right conditions for an optimal impedance matched cavity maximizing its enhancement.

While operating the spectroscopy resonator under vacuum conditions a degradation of the mirrors could be observed as described in section 3.4. As a result the enhancement and thus the intra cavity power decreased over time. This effect is much stronger for a tight focus and high intensity on the mirrors. Using for example focusing mirrors with 200 mm radius of curvature ($w_0 = 28$ μm) which are placed inside the central chamber close to the focus, the laser intensity on the mirrors is increased. In this case the resonator could be operated only for around 20 min before the power dropped by a factor of 2. In the current configuration the mirrors are placed in the small side chambers and are around 60 cm away from the rather weak focus of 91 μm waist radius. Due to the larger beam size on the mirrors, compared to tighter focusing, the intensity is reduced allowing to operate the cavity for around one hour with an enhancement decrease of less than 10 %.

6.2.2. Cold atomic hydrogen beam

At standard temperature and pressure hydrogen is a diatomic gas. To obtain atomic hydrogen it is dissociated in a rf discharge. Before dissociation it is purified using a palladium membrane hydrogen purifier (Johnson Matthey, HP-2). The pure gas is guided by stainless steel tubes to a glass tube of 6 mm inner diameter. A 1 mm constriction in the glass tube causes the hydrogen to accumulate. Around this region a radio frequency (rf) cavity is built up. After starting the discharge by a spark from a Tesla coil, it operates stable and self-contained if the rf power, temperature, and hydrogen pressure in front of the rf cavity are set properly. To reduce thermal stress in the glass tube, the cavity is operated with 10 to 20 W rf power allowing a gas pressure around 1 mbar. Increasing the gas pressure would require higher rf power to drive the discharge. For stable operation the heat is dissipated by water cooling of the glass tube in front of and behind the rf cavity and by a constant nitrogen gas flow inside the cavity. Operating the gas discharge in this way a dissociation degree of 80 to 90 % could be measured behind the glas tube using a mass spectrometer.

During dissociation highly excited hydrogen atoms are generated which decay into the ground state while emitting a cascade of photons. Figure 6.6 shows the visible part of the emitted spectrum which causes the typical pink color of the discharge. The strong lines in the spectrum correspond to the Balmer transitions revealing the appearance of atomic hydrogen while the pedestal is formed by the background light, gas impurities, and molecular hydrogen. The color and the brightness of the discharge is used as a rough indicator for the dissociation efficiency.

A PTFE tube is an excellent material to guide the hydrogen atoms from the gas feed

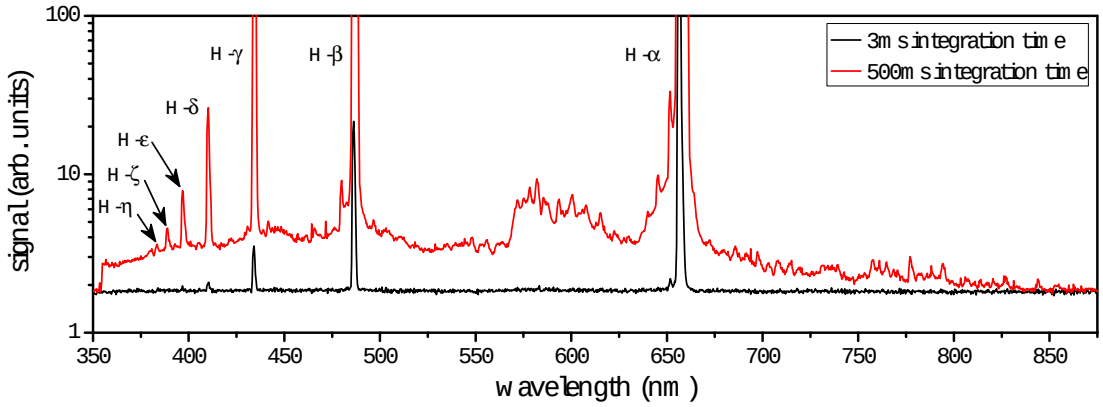

Figure 6.6.: *Typical spectrum of the gas discharge transmitted by the glass tube. The narrow peaks in the spectrum correspond to the Balmer lines in atomic hydrogen. Black line: spectrum obtained with 3 ms integration time. Red line: spectrum obtained with 500 ms integration time.*

through to a cold copper nozzle inside the vacuum chamber. Because of its chemical inertness recombination rates of hydrogen atoms to H_2 molecules are low. Nevertheless the PTFE guiding tubes should be kept short.

The nozzle is attached to a continuous flow cryostat operated with liquid helium and is cooled to around 5.8 K. At lower temperatures the nozzle freezes up within a couple of minutes. Inside the copper nozzle the hydrogen atoms thermalize by collisions with the walls and are then directed to the excitation volume. Inside the copper nozzle the recombination rate of atomic hydrogen may be enhanced. An overall fraction of dissociated H_2 molecules coming out of the nozzle is measured to be around 40 %.

The cryostat is mounted to a x-y-z translation stage allowing to adjust the nozzle position with respect to the interaction volume.

6.2.3. Detection apparatus

The excited hydrogen atoms decay via the $2P$ state emitting two subsequent fluorescence photons, a Balmer H-α at 656.3 nm and a Lyman Ly-α at 121.6 nm, which can be detected by a PMT.

A disadvantage of detecting the Balmer-α photons is the sensitivity of the PMT in the visible wavelength region. It must be carefully shielded against background light coming e.g. from the scattered laser light, gas discharge and environment. The environment and the scattered laser light can be strongly suppressed by using an apropriate narrow bandwidth and colored glas filters. However, Balmer-α photons generated in the gas discharge are efficiently guided by the PTFE tube and leak into the vacuum chamber. Hence the Balmer-α PMT shows a larger background. Despite careful shielding of the

gas discharge a background of around 200 cps is detected by the PMT. Using a Balmer-α PMT (Hamamatsu, R6358) with a quantum efficiency of 10(2) %, a filter combination (colored glass filter with $\mathcal{T} = 91(1)$ % and interference filter with $\mathcal{T} = 94(1)$ %) with a total transmission of 86(1) % at 656.3 nm and a detected solid angle of 4(2) % the overall detection efficiency amounts to 0.3(2) %.

The Lyman-α PMT (Hamamatsu, R7511) is a "solar blind" detector and insensitive above 200 nm, so the environmental light is not an issue here. Also the Lyman-α photons generated in the gas discharge get absorbed as soon as they hit any surface and do not reach the vacuum chamber. The scattered laser light is the only relevant background here which can partly be suppressed by a narrow bandwidth Lyman-α filter. The detected background here amounts to around 30 cps. To avoid additional Fresnel and absorption losses by the imaging optics, they are omitted and the PMT is mounted as close as possible to the interaction region giving a detected solid angle of 0.13(7) of 4π. With a quantum efficiency of 26(2) % and a filter transmissivity of 20(1) % at 121.6 nm the overall detection efficiency amounts to 0.05(3) %.

6.2.4. Simulated spectrum

Using a mode-locked laser for two-photon DFCS all allowed transitions within the lasers bandwidth are addressed. For atomic hydrogen this means that beside the $1S-3S$ doublet four allowed transitions to the $3D$ state shown in figure 6.7 are excited. A spectrum

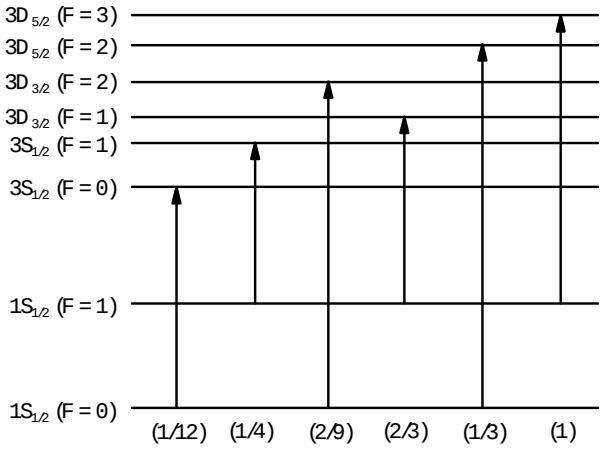

Figure 6.7.: *Transition lines addressed by the laser with a spectral bandwidth of 140 GHz. According to the two-photon transition selection rules for linear polarized light in section 2.2.3 six transitions are excited by the laser. Their relative line strengths with respect to the* $1S_{1/2}(F=1) - 3D_{5/2}(F=3)$ *transition are given at the bottom.*

containing six lines folded into half of the repetition rate seems to be complicated. However, the additional spectral lines provide additional information. The detected count rate is a function of the repetition rate of the laser and the laser detuning providing a 3D structure which can easily be modeled. Hence analyzing spectra at different settings for ω_r allows to extract an accurate value for the $1S-3S$ transition frequency.

Figure 6.8 shows simulated Doppler-free hydrogen spectra for four different repetition rates as functions of detuning. The Doppler-broadened pedestal is omitted. The single

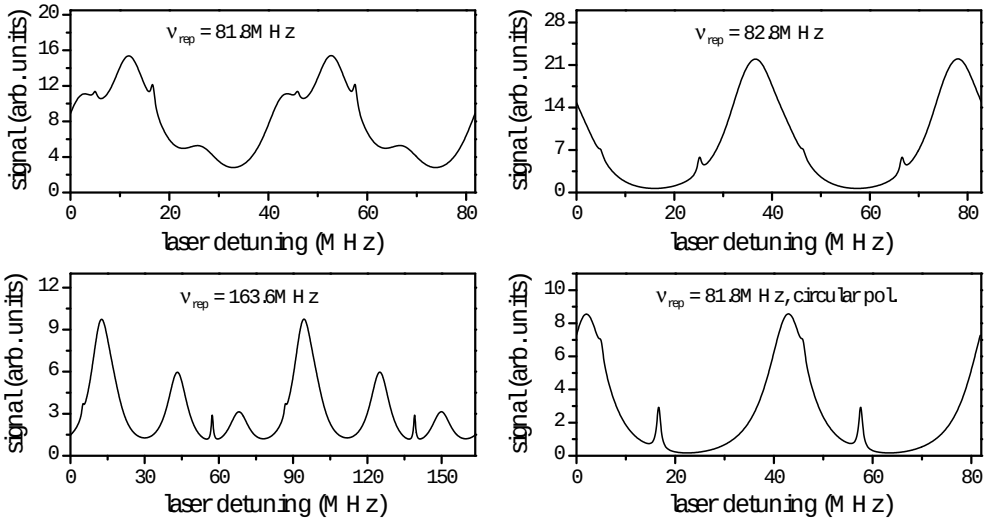

Figure 6.8.: *Expected spectra for different repetition rates. Top left and right and bottom left show six lines folded into a frequency range of* $\nu_{\mathrm{rep}}/2$ *(linear polarization), the Doppler-background is omited. By changing the repetition frequency the six lines may appear at the same laser detuning (top right) or be pulled apart (bottom left). For circularly polarized light only three transitions are allowed (bottom left).*

lines may overlap such that they are hardly resolved, as e.g. in the upper two plots in figure 6.8. This feature can be used while searching for the signal. Choosing the repetition rate such that all the lines appear at almost the same detuning (upper right plot in figure 6.8) and add up to basically one single line in the spectrum, provides a much stronger signal. This enhanced signal can be used to optimize the system with respect to the envelope position, gas discharge, alignment of the atomic beam with respect to the pulse collision point and the imaging system. Increasing the free spectral range by a factor 2 (lower left plot in figure 6.8) pulls the spectral lines apart. In this regime small variations in the repetition rate change the structure of the spectrum which may be analyzed by fitting simulated curves to the spectrum.

Large variations of the FSR cannot be done arbitrarily. In order to use the stabilization scheme described in section 3.2.1 the lasers repetition frequency ν_{rep} should be close to an commensurate value of the free spectral range of the reference resonator ν_{FSR}. Changing the FSR of the SHG or the spectroscopy cavity is only possible by a factor of n or $(2n-1)/2$ respectively, where n is an integer. The latter factor is a consequence of the condition, that two counter propagating pulses must overlap at the center of the resonator. Increasing the FSR goes along with a decrease of the available laser power for the spectroscopy because only every nth mode is resonantly coupled into the cavity.

Using circularly polarized light excludes all transitions with $\Delta F > 0$, according to the two-photon selection rules, leaving three allowed transitions. In this case the relative amplitudes of the $1S-3S$ HFS components remain the same as shown in figure 6.7, while the relative amplitude of the only allowed $3D$ component amounts to 14/25 with respect to the $1S_{1/2}(F=1)-3D_{5/2}(F=3)$ transition with linearly polarized light. Hence, using circular polarization the maximum count rate will fall by around a factor two. A sample spectrum showing the three allowed transition lines is plotted in figure 6.8 (bottom right). In this case the spectrum may be analyzed also at lower repetition rates. Additionally using circular polarization, the Doppler-background is suppressed improving the signal to background ratio.

6.3. Feasibility and lessons learned from Cs and Mg

In order to analyze the feasibility of $1S-3S$ two-photon spectroscopy in hydrogen the expected transition rates are calculated using Monte Carlo simulations. Similar simulations are carried out for cesium and magnesium, where the results can be compared with experimental values. In the end the simulation results and their consequences for H spectroscopy are discussed.

6.3.1. Monte-Carlo simulation

The experimental parameters described in the previous section provide the input for the calculation of the expected count rate by solving the optical Bloch equations (2.10). For constant light intensity this equations of motion can be solved analytically. A solution including decay terms (spontaneous decay and ionization) can be found in e.g. M. Haas *et al.* [14].

For the $1S-3S$ two-photon transition in hydrogen there are two possible decay channels: ionization from the excited state into the continuum ($\gamma_{\mathrm{i}} = 2\pi\, 2.02241 \times 10^{-5}(\mathcal{I}_1(t)+\mathcal{I}_2(t))\ \mathrm{s}^{-1}$), which is negligible for the intensities available in the experiment, and spontaneous decay back to the ground state via the real intermediate $2P$ state ($\gamma_s = 6.32\times10^6\ \mathrm{s}^{-1}$) [14]. The spontaneous two-photon decay to the ground state is negligible. The transition is probed by a mode-locked laser, so the laser intensity is time dependent. In this case an analytic solution for the Bloch equations is very difficult or impossible to find, but they can be integrated numerically for given experimental parameters using, for example, Runge-Kutta methods. In Doppler-free DFCS the two-photon interval is probed by two counter propagating pulse trains. Their temporal and spatial intensity profile can be written in the form

$$\mathcal{I}_{l,r}(x,y,z,t) = \left(\frac{2}{\pi}\right)^{3/2} \frac{\mathcal{P}_{\mathrm{av}}}{\Delta t_{4\omega}\nu_{\mathrm{rep}} w(z)^2}\, \exp\left[-\frac{2\,(x^2+y^2)}{w(z)^2} - \frac{(t\pm z/c - n/\nu_{\mathrm{rep}})^2}{\Delta t_{4\omega}^2}\right], \tag{6.14}$$

where $\mathcal{P}_{\mathrm{av}}$ is the average laser power in one direction, ν_{rep} the pulse repetition frequency, $\Delta t_{4\omega}$ the FH pulse duration, $w(z) = w_0\sqrt{1+(2z)^2/(kw_0^2)^2}$ the laser beam radius with the waist w_0 and wavenumber k and m the pulse number.

Figure 6.9 shows a sample curve for the $3S$ population ρ_{ee} as a function of the atom position with respect to the laser axis for a given velocity and zero detuning. The

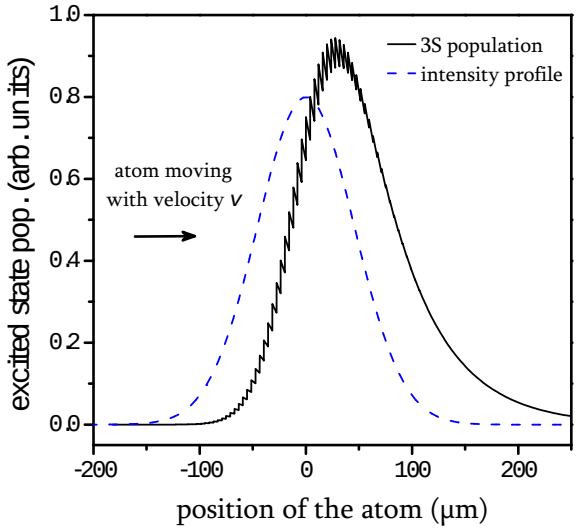

Figure 6.9.: *Solid line: 3S population as a function of the atom position with respect to the laser axis for zero detuning. Dashed line: transverse laser intensity profile. When an atom traveling from left to right enters the laser beam, pulse-wise excitations take place (sawtooth structure). When the atom leaves the intensity profile the excitation probability decreases and at some point the spontaneous decay dominates.*

transverse laser intensity profile is indicated by the dashed line. As the atom enters the laser beam two-photon transitions can take place during the light period. Between the pulses the intensity is zero and the excited state decays via the $2P$ state. This pulse-wise excitation appears as a sawtooth structure in the $3S$ population. Depending on the interaction time the atoms can interact with several tens of pulses while crossing the excitation region. On the trailing edge of the intensity profile the excitation probability decreases and at some point the spontaneous decay dominates the interaction dynamics.

The number of emitted photons per atom is calculated by integrating the transition rate over time. The result strongly depends on the velocity of the atoms and their trajectory through the interaction volume. An arbitrary trajectory of an atoms is defined by $a_{i,0}+v_i t$ $(i=x,y,z)$ with the starting point $(a_{x,0},a_{y,0},a_{z,0})$ located at the exit of the nozzle. While $a_{x,0}=-d$ is the distance of the nozzle from the interaction region, $a_{y,0}$ and $a_{z,0}$ satisfy the condition $(a_{y,0}^2+a_{z,0}^2)\leq r_{\mathrm{nozzle}}$, with r_{nozzle} the radius of the nozzle. The atoms are assumed to be uniformly distributed across the cross sectional area of the nozzle and the emission pattern outside the nozzle follows a $\cos(\theta)$ distribution. The velocity $v=\sqrt{v_x^2+v_y^2+v_z^2}$ of the atoms is supposed to be Maxwellian distributed and

its components are calculated as follows:

$$
\begin{aligned}
v_x &= v\cos(\theta)\,,\\
v_y &= v\sin(\theta)\cos(\phi)\,,\\
v_z &= v\sin(\theta)\sin(\phi)\,,
\end{aligned}
$$

where θ varies between 0 and $\pi/2$ and ϕ varies between 0 and 2π. The velocity vector $\boldsymbol{v} = (v_x, v_y, v_z)$ defines the propagation direction of the atoms.

Only atoms passing the interaction region can contribute to the signal. For a pulse length shorter than the confocal parameter ($l_p < b$) this region corresponds to an ellipsoid which principal axes are given by the pulse length (in z direction) and the waist diameter (in x and y direction). To get a representative average value per atom leaving the nozzle, $\mathfrak{R}_{ge}^{\mathrm{av}}$/atom, the transition rate is averaged over a sufficient number of randomly chosen trajectories and velocities.

6.3.2. Simulation results for H, Cs and Mg

Monte Carlo simulations as described above are carried out for hydrogen as well as for cesium and magnesium. For the latter two the results are compared with the experimental values, which gives information about the feasibility of hydrogen spectroscopy. The relevant parameters entering the simulations and the simulation results for Cs, Mg and H are summarized in table 6.2.

The expected count rate is calculated by multiplying the number of photons per atom by the atom flow rate out of the nozzle and the detection efficiency. The atom flow rate and the detection efficiency are determined from actual experimental parameters.

For H the atom flow rate is determined from the H_2 flow rate and degree of dissociation. The molecular flow rate is measured by monitoring the pressure change in a reservoir of known volume placed between the purifier and the discharge tube, while the pressure inside the discharge tube is set to 0.8 mbar. Due to the large spread angle of the atomic beam leaving the nozzle and the distance of the nozzle to the laser axis, only around 1 % of the hydrogen atoms pass the interaction volume. This is accounted for in the simulations by averaging over a large number (50 000) of random trajectories.

The spectral lines in H and Cs split into two hyperfine components with reduced amplitudes. This splitting is not taken into account in the Monte Carlo simulations. The relative amplitudes of the two hyperfine components in H amount to 3/4 and 1/4 respectively. The count rate of the strongest of the hyperfine components $\mathfrak{R}_{ge}^{\mathrm{sim.}}$(HFS) is listed in table 6.2.

The excitation geometry in Mg spectroscopy is very similar to the geometry in H spectroscopy. Hence definition of trajectories of the atoms is the same as described above. An atomic beam is generated using a Mg-oven described in section 5.2. Heated to around 600 K the vapor pressure inside the oven amounts to $1.6(7) \times 10^{-2}$ Pa. At

Table 6.2.: *Comparison between Cs, Mg and H. Listed are the relevant parameters entering the MC simulation and the simulation results. The count rates for cesium and hydrogen are given for the strongest hyperfine component respectively.*

	^{133}Cs $6S-8S$	^{24}Mg $^1S_0-{}^1D_2$	H $1S-3S$
β_{ge} (Hz (W/m^2)$^{-1}$)	0.99×10^{-2} (1)	1.62×10^{-3} (2)	1.00333×10^{-5} (3)
$\beta_{\mathrm{AC}}(g)$ (Hz (W/m^2)$^{-1}$)	1.73×10^{-2} (1)	-0.7×10^{-3} (2)	-3.02104×10^{-5} (3)
$\beta_{\mathrm{AC}}(e)$ (Hz (W/m^2)$^{-1}$)	-0.61×10^{-2} (1)	-0.93×10^{-3} (2)	9.80847×10^{-5} (3)
β_{ioni} (Hz (W/m^2)$^{-1}$)	2.64×10^{-4} (4)	1.2×10^{-3} (5)	2.02241×10^{-5} (3)
γ_s (s^{-1})	$2\pi\times1.53$ MHz	$2\pi\times2$ MHz	$2\pi\times1$ MHz
λ_L (nm)	822.46	430.87	205.14
Δt (ps)	1.3	1.1	2.4
$\mathcal{P}_{\mathrm{av}}$ (W)	0.1	0.43	0.1
w_0 (μm)	26	132	91
$\mathcal{I}_{\mathrm{av}}$ (MW/m^2)	47	7.9	3.8
T (K)	295	600	5.8
nozzle radius r (mm)	vapor cell	1	1
photons per atom	3.5×10^{-3}	2.8×10^{-6}	3.5×10^{-9}
atom flow rate (1/s)	$9.7(1)\times10^{12}$	$4(2)\times10^{15}$	$8(1)\times10^{16}$
detection efficiency (%)	0.5(1)	0.009(1)	0.05(3)
$\mathfrak{R}_{ge}^{\mathrm{sim.}}$ (cps)	$17(3)\times10^7$	$1.0(4)\times10^6$	$1.4(9)\times10^5$
$\mathfrak{R}_{ge}^{\mathrm{sim.}}$(HFS / isotope) (cps)	$10(2)\times10^7$	$8(3)\times10^5$	$1.1(7)\times10^5$
$\mathfrak{R}_{ge}^{\mathrm{meas.}}$ (cps)	1.1×10^4	2×10^3	

(1) calculated using dipole matrix elements tabulated by Sieradzan *et al.* [66]

(2) calculated using dipole matrix elements tabulated by Porsev *et al.* [50]

(3) tabulated by Haas *et al.* [14]

(4) calculated using the ionization cross section given by Lahiri *et al.* [67]

(5) calculated using the ionization cross section given by Uitenbroek *et al.* [68]

this temperature the atoms move with a mean velocity of 725 m/s. Here the oven is around 10 mm away from the laser axis, so only 0.4 % of the atoms leaving the oven pass the interaction region. The calculated count rate $\mathfrak{R}_{ge}^{\mathrm{sim.}}$(isotope) for ^{24}Mg, which has the highest natural abundance of 79 % of the three stable Mg isotopes, is listed in table 6.2.

Cs spectroscopy is carried out in a gas-cell. For the simulations the interaction volume, which is actually an ellipsoid, is approximated by a sphere which radius is given by the semi-major axis of the ellipsoid ($r = 2\,c\,\Delta t_\omega/\sqrt{2\ln(2)}$). Two random points which define a trajectory of an atom are chosen on the surface of the sphere. The flow rate of Cs atoms through the cross sectional area $A = \pi\,(2\,c\,\Delta t_\omega/\sqrt{2\ln(2)})^2$ is calculated

from the vapor pressure in the cell at room temperature of 1.33×10^{-4} Pa and the mean velocity of the atoms. Averaging over 50 000 random trajectories through this sphere provides the average transition rate per atom passing the sphere around the excitation volume. The relative amplitudes of the HFS components in Cs amount to 9/16 and 7/16, the strongest of these components is listed in 6.2.

6.3.3. Comparison of simulation with experiment

A comparison of the count rates for Cs and Mg reveals a difference of up to four orders of magnitude between the experiment and the simulation. The reason for this difference may be attributed to over estimated experimental parameters entering the calculations and systematic effects which are not taken into account, but reduce the count rate. Possible effects are discussed in the following.

Excitation geometry and alignment

Misalignments in the pulse overlap in form of phase front tilting result in destructive interference of the back and forth propagating electric fields. To get an expression for the associated signal decrease consider the two-photon transition rate which is proportional to the squared absolute value of the product of the forth and back propagating electric field

$$\mathfrak{R}_{ge} \propto |E_1(t,\boldsymbol{r})E_2(t,\boldsymbol{r})|^2 \tag{6.15}$$

Assuming two plane waves of same frequency and amplitude but with different phases $\varphi_1(\boldsymbol{r})$ and $\varphi_2(\boldsymbol{r})$, $E_{1,2}(t,\boldsymbol{r}) = E(t)\exp\left[-i\varphi_{1,2}(\boldsymbol{r})\right]$, equation (6.15) can be rewritten to

$$\mathfrak{R}_{ge} \propto \mathcal{I}^2(t)\cos^4\left(\frac{\varphi_1(\boldsymbol{r}) + \varphi_2(\boldsymbol{r})}{2}\right) , \tag{6.16}$$

where $\mathcal{I}(t) = (1/2)\varepsilon_0 cE(t)$ is the time dependent intensity in one beam and $\varphi_{1,2}(\boldsymbol{r}) = \boldsymbol{k}_{1,2}\boldsymbol{r}$ is a real spatial phase. The wave vectors may be written in spherical coordinates

$$\begin{aligned}\boldsymbol{k}_1 &= (k_1\sin(\theta_1)\cos(\phi_1), k_1\sin(\theta_1)\sin(\phi_1), k_1\cos(\theta_1)) ,\\ \boldsymbol{k}_2 &= (-k_2\sin(\theta_2)\cos(\phi_2), -k_2\sin(\theta_2)\sin(\phi_2), -k_2\cos(\theta_2)) .\end{aligned}$$

and $\boldsymbol{r} = (x,y,z)$. Assume a by an angle θ_2 tilted back propagating wave ($\phi_2 = 0$) while the forth propagating beam travels along the z direction ($\theta_1 = \phi_1 = 0$). On laser axis ($x = y = 0$) the total phase amounts to $\varphi_1(\boldsymbol{r}) + \varphi_2(\boldsymbol{r}) = -kz(1-\cos(\theta_2))$ setting $z = c/(2\nu_r)$ yields

$$\mathfrak{R}_{ge} \propto \mathcal{I}^2(t)\cos^4\left(-\frac{\pi c}{2\nu_r\lambda_{2\omega}}(1-\cos(\theta_2))\right) \tag{6.17}$$

According to this relation a small angle detuning of 0.5 mrad results in a signal decrease by two orders of magnitude. Furthermore a misalignment in the position of the pulse

overlap with respect to the focus position results in a reduced laser intensity due to larger beam diameter. This will further reduce the count rate. These effects may partially explain the strong deviation between the simulation and the experiment in table 6.2.

Using a symmetrical spectroscopy resonator of appropriate length, as is the case in Mg and H spectroscopy, the counter propagating pulses overlap at the center of the cavity. However, while propagating in the cavity the two laser beams acquire a spatial phase. The corresponding maximum tilt angle of the laser beam can be approximated by $\theta_{\max} = \lambda_{2\omega}\pi/(2w\mathcal{F})$ where $2w$ is the beam diameter assuming a collimated beam and $\mathcal{F}$ is the cavity finesse which can be approximated by $\mathcal{F} = 2\pi U$ with U the enhancement of the cavity. With a measured enhancement of $U = 2$ the maximum tilt angle amounts to $\theta_{\max} = 0.1$ mrad resulting in a signal decrease according to equation (6.17) by only 1 %.

Number of atoms

Uncertainties in the calculation of the number of atoms interacting with the laser also affect the calculated count rates. Magnesium, for example, is heated in an oven to generate an atomic beam (see chapter 5), so only the temperature of the oven is accessible here, while the actual temperature of the Mg atoms might be somewhat different. Depending on the quality of the contacts different temperatures are measured while the heating current is the same. Here variations in the temperature by only 1.6 % result in particle density variations by around 60 %.

For hydrogen a big uncertainty arises from fluctuations in the degree of dissociation which strongly depend on the treatment of the copper nozzle and the PTFE tube. Imperceptive differences in the handling have big impact on the recombination rate. But once cleaned properly the parts can be used for weeks of measurements until they are exposed to air for a longer time.

Envelope position and fluctuations

As discussed in section 2.4 and 4.3.1 the count rate is maximized for a centered spectral pulse envelope. Detuning the spectrum with respect to the transition frequency results in an exponential decrease of the signal with squared detuning. Using an OSA the spectral envelope at the fundamental wavelength can be adjusted within 0.003 nm. This small uncertainty results in a signal decrease by less than 1 % at the fundamental as well as at the second and fourth harmonic and thus can be neglected.

By monitoring the position of the spectral pulse envelope at 820 nm small jumps and drifts of the envelope could be observed from time to time during the operation. These effects may probably be attributed to atmospheric turbulences and convections inside the laser resonator. Albeit one can manually compensate for the drift, the jumps cannot be compensated and could cause additional statistical fluctuations in the signal.

Another serious problem comes along with the SHG in the BBO crystal. Due to the high GVM of 6.5 ps in a 5 mm long crystal only a part of the incident spectrum at 410 nm can be frequency doubled. Approaching the phase matching cut-off of the nonlinear crystal, which is at 204.7 nm for BBO, the nonlinear coefficient decreases rapidly. Thus, while maximizing the output power of the UV pulses by adjusting the phase matching angle of the crystal their spectrum might be shifted to somewhat higher wavelengths. This effect can be avoided by using a UV spectrometer while aligning the resonator.

Residual chirp

As discussed in section 2.3 and 4.3.2 the signal strength drops with the inverse time bandwidth product if the pulses posses a symmetric phase shift around the two-photon transition frequency. A characterization of the fundamental, SH and FH pulses in section 3.3 revealed close to transform limited pulses. A residual chirp of the SH and FH pulses may be approximated by an upper limit for the TBP of 0.34 resulting in a signal decrease by around 8 % for Mg and H.

Fresnel losses

The detection efficiency given in table 6.2 accounts only for the quantum efficiency, transmissivity of the filters and detected solid angle while Fresnel, scattering and absorption losses of the imaging optics, the gas cell and the detection windows are neglected. In Cs and Mg spectroscopy the interaction region is focused onto the cathode of the PMT using two AR coated focusing lenses. Due to the AR coating the Fresnel reflections at their surfaces are below 0.5% resulting in a maximum loss of around 2 %.

A much higher contribution is expected to come from the vapor-cell / detection window of the spectrometer. Cs spectroscopy is carried out in a gas-cell at room temperature. Cs depositions can be observed at the inner surface of the cell which reduce the transmissivity of the cell for the fluorescence light at 456 nm. In Mg spectroscopy the emitted fluorescence light is detected through a CaF_2 window in the vacuum chamber. After some time a thin Mg layer appears on this window reducing continuously its transmissivity during a measurement run. Between the runs this window is cleaned. In contrast, in H spectroscopy the PMT's are placed inside the vacuum chamber and the imaging optics are omitted to avoid additional losses.

In Cs and Mg spectroscopy the laser beam suffers losses through focusing lenses and laser windows of the vapor-cell and the vacuum chamber. Due to these losses the back and forth reflected beams are of unequal intensity. To avoid these losses the $1S - 3S$ spectroscopy resonator is built inside the vacuum chamber and only reflective optics are used.

6.3.4. Conclusion for H spectroscopy

While Cs spectroscopy is carried out in a cell without a resonator, in magnesium and hydrogen spectroscopy an enhancement cavity is built around an atomic beam which crosses the interaction volume perpendicular to the laser axis. Thus the comparison of simulation and experiment for Mg seems more applicable to H. However the detection and the laser windows of the Mg spectrometer may be coated by a thin layer of Mg reducing their transmission. This easily can reduce the theoretical count rate by one order of magnitude. In hydrogen spectroscopy, systematic effects as the envelope shift and residual chirp, which do not affect Mg spectroscopy that much, reduce the signal by at least 10 %. In total we can assume that the expected count rate in $1S-3S$ spectroscopy in H amounts to around 1000 cps.

On the other hand, due to its high bandwidth (0.14 THz) also two-photon transitions to the $3D$ state are addressed by the laser (see section 6.2.4). According to the transition matrix elements listed in [14] $1S-3S$ is 6 times weaker than the $1S-3D$ transition. This interval splits into two FS components which then further split up into two HFS components respectively. Following the two-photon selection rules four allowed transitions to the $3D$ are addressed by the laser. Calculating the matrix elements for these HFS components reveals that $\beta_{ge}(1S_{1/2}(F=1)-3D_{5/2}(F=3))$ is still 5 times stronger than $\beta_{ge}(1S-3S)$. With the lasers repetition rate of around 82 MHz the six spectral lines will partly overlap providing a stronger signal (see figure 6.8).

The Doppler-free spectrum (see simulated curves in figure 6.8) originates only from the pulse collision volume. Due to coarse misalignments of this interaction region with respect to the atomic beam or of the detector position the spectroscopy may fail. However as soon as the atoms cross the laser beam at least the Doppler-background should appear for linearly polarized light. In H spectroscopy the Doppler pedestal is a superposition of six Doppler broadened lines and is thus strongly enhanced. Calculating the contrast between the strong $1S-3S$ hyperfine component and the Doppler background according to equation (2.7) while taking the FS and HFS components in H into account which are addressed by the laser (see figure 6.7) results in a contrast of 0.39. That means that the Doppler pedestal is expected to be 2.6 times higher than the narrow $1S-3S$ signal. The appearance of this pedestal will be an indicator for the interaction of H atoms with the laser field and will serve as a starting point for the search of the narrow Doppler-free signal. In the next step circularly polarized light will be used to suppress this Doppler background and to analyze the $1S-3S$ doublet.

As discussed above, the expected count rate amounts to around 10^3 cps while the background originating from scattered light could be reduced to around 200 cps and 30 cps for Balmer-α and Lyman-α PMT respectively. To rate the detectability of the expected signal in table 6.3 the calculated count rate, the detection efficiency, the background count rate and the signal to background ratios S/B are listed for different detection schemes. For all three detection schemes the signal is well above the detection limit of 1.

Table 6.3.: *Signal to background ratios for detection of Balmer-α and Lyman-α photons and for coincidence measurements.*

	signal (Hz)	detection efficiency	background (Hz)	S/B ratio
Balmer-α detector	6.3×10^3	3×10^{-3}	200	4.2×10^3
Lyman-α detector	1.1×10^3	5×10^{-4}	30	4.7×10^3
coincidence	3.2	1.5×10^{-6}	6×10^{-13}	5.2×10^{12}

However, the actual count rates may be well below the calculated ones and fall below the detection limit. The much higher signal to background ratio of the coincidence method allows to detect very small signals but that requires longer integration times. Additionally, statistical fluctuations need some times to average out and thus a good laser and atomic beam stability over this time. Due to the UV degradation effects (see section 3.4) the long-term stability of the laser is poor. The operation time over which the power decrease is less than 10 % ranges between 30 and 60 minutes. The operation time is also limited by the time it takes the nozzle to freeze up. The speed of this process depends on the purity of the hydrogen gas, the vacuum chamber pressure and the nozzle design. During the operation the particle flow may continuously decrease due to an appearing restriction.

The amount of atoms leaving the nozzle strongly depends on the treatment of the copper nozzle and the PTFE tube. Under some conditions the recombination rate is almost 100 % and only molecular hydrogen leaves the nozzle. The design of the nozzle gives a limit on the time it takes until the nozzle freezes up. An analysis of our nozzle using a mass spectrometer showed that it froze up within a couple of minutes and during the measurements no hydrogen was present at the interaction volume. Also after switching to a nozzle which was tested in the $1S - 2S$ experiment no signal could be detected yet.

6.4. Future directions

Despite all improvements achieved and experience during this thesis it was not possible to detect any signal from hydrogen. Possible reasons for that were discussed in the previous section. Possible solutions for the problems encountered during my work are discussed in the following.

Laser stability

The stability of the laser system can be further improved by increasing the FSR of the enhancement and spectroscopy resonators making them less sensitive to perturbations. Starting right at the beginning with a laser emitting pulses at a higher repetition rate means a new fundamental laser or at least substantial replacements and probably a new reference cavity for laser stabilization. Increasing the repetition rate of the laser while the average output power remains the same will reduce the pulse peak power and thus make the nonlinear conversion less efficient. Tuning the Ti:sapphire laser for higher output power (see section 3.2.1) and using one of the SHG cavities as a filter cavity the FSR can be increased with only a small power loss. The first conversion stage is quite efficient and provides a stable output power of up to 1 W at 410 nm (with a 5 mm long plane AR coated LBO crystal and modified Ti:sapphire laser), whereas the second one is operated at the edge of the phase matching which reduces the efficiency. As described in section 3.2.4 only an output power of 50 to 60 mW can be generated stable for around 30 min, but the transmission fringes, while scanning the cavity, indicate a higher possible power. From this can be concluded that the SHG process in the BBO is running in a saturated regime. So setting this cavity up as a filter cavity with a free spectral range of $\mathrm{FSR} = 2\,\nu_{\mathrm{rep}}$ (i.e. every second comb mode is coupled into the resonator) the coupled power into the resonator will drop by a factor 2 but the output power will probably remain the same or drop only by a small amount. In this way the short and long-term stability of the laser can be improved.

UV degradation (see section 3.4) and absorption in BBO and its unfavorable close cut-off angle limit the maximum output power at 205 nm. These effects are also responsible for the power loss over time during the SHG process. Cooling the crystal to lower temperatures shifts the cut-off angle to shorter wavelengths increasing the nonlinearity. Currently the crystal is cooled to $-10°\mathrm{C}$. Going to lower temperatures using e.g. a cryostat may increase its nonlinearity even further providing a higher output power at 205 nm.

Using another NLO crystal for SHG at 205 nm some of the limiting effects may be reduced or removed. KBBF is a suitable nonlinear crystal for SHG at 205 nm (see section 3.2.3). Although it has a comparable nonlinearity a lower output power is expected with the same pump intensity. However, due to the much lower cut-off wavelength an appreciably better long-term stability of the SHG power is expected.

Envelope position

As described above shifting the spectral envelope with respect to the transition frequency leads to an exponential signal decrease with squared detuning. There are two major sources for such a shift: jumps of the spectral envelope at the fundamental wavelength and GVM in the BBO crystal. The first of them may probably be reduced by purging

the laser with a dry gas. To reduce the effect of GVM a shorter BBO crystal can be used but that goes at the expense of the output power. Another possibility would be to monitor the spectral envelope using e.g. a monochromator and align the spectral envelope at 205 nm rather than at 820 nm.

Detection efficiency

To improve the efficiency a large-solid-angle-detector can be used. Such a detector consists of a sphere or simply a box with the inner side coated with a suitable material and a channeltron to detect the photoelectrons. The work function $\mathfrak{E}_{\mathrm{W}}$ of this material should be below the energy of the detected photons. To detect Lyman-α photons, with a photon energy of 10.2 eV, emitted upon decay of the $2P$ state, e.g. graphite ($\mathfrak{E}_{\mathrm{W}} = 5$ eV) or potassium bromide (KBr, $\mathfrak{E}_{\mathrm{W}} \approx 8.2$ eV) can be used as coating material. Such a detector coated with graphite was recently build and successfully tested by our colleagues working on the $1S - 2S$ spectroscopy in hydrogen.

Using graphite the detector can easily be spray coated and the coating is very robust against atmospheric conditions. However its work function is below the photon energy of 6 eV of our laser, so the scattered laser light will also be efficiently detected, causing a high background. KBr instead has a work function which is above the photon energy of our laser but at atmospheric conditions it must be kept at low humidity and it is deposited by evaporation [69].

Longer interaction time

An improved laser stability will only facilitate the detection of the low signal, but increasing the signal itself would be more helpful. A possibility to do that would be to increase the interaction length and the average laser intensity. Blowing up the waist radius by a factor 2, in transverse excitation arrangement, will require a power enhancement of at least a factor 4 to maintain the intensity, but in longitudinal excitation arrangement the interaction length can be increased by working with longer pulses. However starting with longer pulses at the fundamental wavelength while leaving the average output power the same, means lower peak intensities for the SHGs and thus lower output power at 205 nm. But driving the nonlinear mixing processes with short pulses and lengthen them after the FHG will maintain high conversion efficiencies while providing a longer interaction length. This can be achieved by reducing the spectral bandwidth, as occurs in the BBO during the SHG, or by lengthening the pulses by chirping. As pointed out in section 2.3 only a symmetric phase shift will reduce the transition rate, while an antisymmetric phase shift will leave the signal unaffected.

Flux of atomic hydrogen

Another possibility to raise the count rate is to increase the flux of atomic hydrogen. By improving e.g. the parameters of the gas discharge and using different material than a glass tube for the discharge the degree of dissociation can be enhanced. Using different tubing and nozzle materials may reduce the recombination rate while guiding the hydrogen atoms to the interaction region.

Optimizing the nozzle geometry a more directional emission pattern may be generated, rather than the $\cos(\theta)$ distribution, resulting in a higher flux of atomic hydrogen through the interaction volume.

Hydrogen beam detector

There are several possibilities to prove and monitor the presence of hydrogen atoms, the most common of them are a mass spectrometer and a calorimeter. A mass spectrometer would provide directly the particle flow and degree of dissociation as was demonstrated e.g. by J. T. M. Walraven and I. F. Silvera [70], but would require a complex vacuum chamber with differential pumping, allowing a higher pressure region around the gas feed through and providing an ultra high vacuum (UHV) region for the quadrupole. To obtain reliable results, the UHV region should be evacuated to around 10^{-9} mbar. A calorimeter instead measures the energy upon recombination of hydrogen atoms. As a detector a 5 μm thin gold plated tungsten/rhenium wire can be used as described by V. A. Trofimov *et al.* [71]. The recombination heat on the surface of the wire cause its resistance to increase which can be detected by applying a small current and measuring the voltage. The advantage of this method is that the detector can be placed right in front of the nozzle without impairing the hydrogen flow and it does not have such tight requirements on the vacuum conditions as is the case for a mass spectrometer. But this detection scheme only provides a relative measure for the atomic hydrogen. However such a thin wire detector will be installed in the spectrometer as an indicator for atomic hydrogen.

Different approaches

All the findings add up to the fact, that a much higher average power at 205 nm will be essential. Using SHG in a BBO crystal to generate the UV light seems to be associated with some fundamental difficulties, which cannot be easily circumvented. Another approach would be sum frequency generation in a CLBO or a BBO crystal. By mixing the output of an optical parametric oscillator (OPO) at 942 nm (400 mW) with the fourth harmonic of a mode-locked Nd:YLF laser at 262 nm (600 mW) in a CLBO crystal ($d_{\text{eff}} = 1.04$ pm/V), an output power as high as 225 mW can be generated, as demonstrated by K. F. Wall *et al.* [72]. But therefore a completely different laser system would be necessary. However using SFG a tunable laser system capable of generating

194.5 nm wavelength and below will be suitable for spectroscopy of the $1S - 4S$ and higher S levels in hydrogen. This will allow a more precise determination of the ground state Lamb shift.

A. Resulting publications

A deep-UV optical frequency comb at 205 nm

E. Peters[1], S. A. Diddams[1,2], P. Fendel[1], S. Reinhardt[1], T. W. Hänsch[1], Th. Udem[1]

[1]*Max Planck Institute of Quantum Optics, Hans-Kopfermann-Str. 1, D-85748 Garching, Germany*
[2]*On leave from the National Institute of Standards and Technology, 325 Broadway, Boulder, Colorado 80305, USA*

elisabeth.peters@mpq.mpg.de

Abstract: By frequency quadrupling a picosecond pulse train from a Ti:sapphire laser at 820 nm we generate a frequency comb at 205 nm with nearly bandwidth-limited pulses. The nonlinear frequency conversion is accomplished by two successive frequency doubling stages that take place in resonant cavities that are matched to the pulse repetition rate of 82 MHz. This allows for an overall efficiency of 4.5 % and produces an output power of up to 70 mW for a few minutes and 25 mW with continuous operation for hours. Such a deep UV frequency comb may be employed for direct frequency comb spectroscopy in cases where it is less efficient to convert to these short wavelengths with continuous wave lasers.

OCIS codes: (140.3610) Lasers, ultraviolet; (190.2620) Harmonic generation and mixing

References and links

1. A. Dubietis, G. Tamošauskas, A. Varanavičius, G. Valiulis, and R. Danielius, "Highly efficient subpicosecond pulse generation at 211 nm," J. Opt. Soc. Am. B **17**, 48-52 (2000).
2. A. Nebel and R. Beigang, "External frequency conversion of cw mode-locked Ti : Al_2O_3 laser radiation," Opt. Lett. **16**, 1729-1731 (1991); "Tunable picosecond pulses below 200 nm by external frequency conversion of cw modelocked Ti : Al_2O_3 laser radiation," Opt. Commun. **94**, 369-372 (1992).
3. K.F. Wall, J.S. Smucz, B. Pati, Y. Isyanova, P.F. Moulton, and J.G. Manni, "A quasi-continuous-wave deep ultraviolet laser source," IEEE J. Quantum Electron. **39**, 1160-1169 (2003).
4. F. Rotermund, and V. Petrov, "Generation of the fourth harmonic of a femtosecond Ti:sapphire laser," Opt. Lett. **23** 1040-1042 (1998).
5. J. Ringling, O. Kittelmann, F. Noack, G. Korn and J. Squier, "Tunable femtosecond pulses in the near vacuum ultraviolet generated by frequency conversion of amplified Ti:sapphire laser pulses," Opt. Lett. **18** 2035-2037 (1993).
6. S. Bourzeix, B. de Beauvoir, F. Nez, F. de Tomasi, L. Julien, and F. Biraben, "Ultra-violet light generation at 205 nm by two frequency doubling steps of a cw titanium-sapphire laser," Opt. Commun. **133**, 239-244 (1997).
7. O. Arnoult, F. Nez, C. Schwob, L. Julien, and F. Biraben, "Towards an absolute measurement of the 1S-3S line in atomic hydrogen," Can. J. Phys. **83**, 273-281 (2005).
8. B. de Beauvoir, C. Schwob, O. Acef, L. Jozefowski, L. Hilico, F. Nez, L. Julien, A. Clairon, and F. Biraben, "Metrology of the hydrogen and deuterium atoms: Determination of the Rydberg constant and Lamb shifts," Eur. Phys. J. D **12**, 61-93 (2000).
9. G. Hagel, F. Nez, and F. Biraben, "Analysis and observation, on an atomic resonance, of the frequency shift due to the length modulation of an optical cavity," Appl. Opt. **41**, 7702-7706 (2002).
10. J. Sakuma, Y. Asakawa, T. Sumiyoshi, and H. Sekita, "High-power cw deep-UV coherent light sources around 200 nm based on external resonant sum-frequency mixing," IEEE J. Sel. Top. Quantum Electron. **10**, 1244-1251 (2004).
11. Th. Udem, R. Holzwarth, and T.W. Hänsch, "Optical frequency metrology." Nature **416**, 233-237 (2002).
12. Ye.V. Baklanov, and V.P. Chebotayev, "Narrow resonances of two-photon absorption of super-narrow pulses in a gas," Appl. Phys. **12**, 97-99 (1977).

#108584 - $15.00 USD Received 10 Mar 2009; revised 22 Apr 2009; accepted 22 Apr 2009; published 15 May 2009

13. A. Marian, M.C. Stowe, D. Felinto, and J. Ye, "Direct frequency comb measurements of absolute optical frequencies and population transfer dynamics," Phys. Rev. Lett. **95**, 023001/1-4 (2005).
14. P. Fendel, S.D. Bergeson, Th. Udem, and T.W. Hänsch, "Two-photon frequency comb spectroscopy of the 6s-8s transition in cesium," Opt. Lett. **32**, 701-703 (2007).
15. M.J. Snadden, A.S. Bell, E. Riis, and A.I. Ferguson, "Two-photon spectroscopy of laser-cooled Rb using a mode-locked laser," Opt. Commun. **125**, 70-76 (1996).
16. R.W.P. Drever, J.L. Hall, F.V. Kowalski, J. Hough, G.M. Ford, A.J. Munley, and H. Ward, "Laser phase and frequency stabilization using an optical-resonator," Appl. Phys. B **31**, 97-105 (1983).
17. H.W. Kogelnik, E.P. Ippen, A. Dienes, and C.V. Shank, "Astigmatically compensated cavities for cw dye lasers," IEEE J. Quantum Electron. **8**, 373-379 (1972).
18. G.D. Boyd, and D.A. Kleinman, "Parametric interaction of focused Gaussian light beams," J. Appl. Phys. **39**, 3597-3639 (1968).
19. T.W. Hänsch and B. Couillaud "Laser frequency stabilization by polarization spectroscopy of a reflecting reference cavity," Opt. Commun. **35**, 441-444 (1980).
20. C. Chen, "Recent advances in deep and vacuum-UV harmonic generation with KBBF crystal," Opt. Mater. **26**, 425-429 (2004).
21. C. Chen, Y. Wang, B. Wu, K. Wu, W. Zeng, and L. Yu, "Design and synthesis of an ultraviolet-transparent nonlinear optical crystal $Sr_2Be_2B_2O_7$," Nature **373**, 322-324 (1995).
22. A.V. Smith, "How to select nonlinear crystals and model their performance using SNLO software," Proc. SPIE **3928**, 62-69 (2000).
23. Z. Min, R.W. Quandt, R. Bersohn and H.L. Kim "Extended range of second harmonic generation in $\beta - BaB_2O_4$," IEEE J. Quantum Electron. **34**, 2409 (1998).
24. J.C. Diels and W. Rudolph *Ultrashort Laser Pulse Phenomena*, (Academic, 2006).
25. A.P. Baronavski, H.D. Ladouceur, and J.K. Shaw, "Analysis of cross correlation, phase velocity mismatch, and group velocity mismatches in sum-frequency generation," IEEE J. Quantum Electron. **29**, 580-589 (1993).

1. Introduction

Frequency conversion in nonlinear crystals has been used for a long time to convert laser radiation to shorter wavelengths that is difficult, or impossible to generate directly with existing laser systems. In fact the shortest wavelengths of continuous wave (cw) radiation are generated in this way. The limit for this method is set by the phase matching and transparency range of available nonlinear crystals. Among the known crystals β-barium borate BaB_2O_4 (BBO) is transparent down to 185 nm while it can be phase matched for frequency doubling (SHG) to about 205 nm. Other crystals like lithium triborate LiB_3O_5 (LBO) are transparent to even shorter wavelengths (160 nm) but the phase matching cut-off for SHG occurs at a longer wavelength than for BBO. Sum frequency generation can be used for both crystals to reach the transparency cut-off. While previous authors have used this strategy with ps [1, 2, 3] and fs [4, 5] pulses, the required temporal and spatial overlap of two different color pulses adds further complications that may compromise performance, particularly when one desires the enhancement provided by a resonant optical cavity. This seems to be unnecessary if one is interested in wavelengths above the shortest phase matchable for SHG, which is 205 nm in BBO. This is the subject of this work.

A pulsed laser system at this wavelength will be useful for 2-photon excitation of the $1S-3S$ transition in atomic hydrogen [6, 7]. An improved value of this transition frequency can be used to further test quantum electrodynamics and to reduce the uncertainty of the Rydberg constant [8]. So far the use of cw lasers for spectroscopy of this transition has been plagued by unwanted nonlinearities, such as photo refractivity, that sets in preferably at shorter wavelengths. A cw laser system for 205 nm that has been used by G. Hagel and co-workers [9], developed a strong counter propagating wave at 410 nm within the last doubling cavity in a very short time after locking. Unfortunately this effect has thus far limited the operation to a scanning or pulsed mode of operation. The resulting 4 μs pulses are subject to periodic Doppler shifts arising from the forward and backward motion of the cavity mirror, which yields a double-peaked $1S-3S$ line shape. Due to nonlinear frequency chirps caused by an intensity dependence of the refractive index of BBO (thermal and Kerr-effect), the average of the two apparent lines does not necessarily agree with the unshifted transition frequency.

#108584 - $15.00 USD Received 10 Mar 2009; revised 22 Apr 2009; accepted 22 Apr 2009; published 15 May 2009

While there are other schemes to generate cw 205 nm light that avoid UV enhancement cavities [10], a mode locked pulsed laser might also provide a solution to this problem. Typically nonlinear frequency conversions are very efficient in the ps regime because large peak intensities can be exploited while phase matching bandwidth limitations are not a serious issue. This relaxes the requirements on the enhancement cavity quality. In addition, nonlinear frequency chirps are stationary in a stationary pulse train and should not shift the observed transition frequency in subsequent spectroscopy, although they may reduce the excitation rate. In the frequency domain such a pulse train is described by a frequency comb [11] and a frequency chirp imposed on the pulses is expressed by a phase change of the modes rather than by a frequency change of these modes. Strictly speaking, the non-linear process discussed here is mostly sum frequency generation among the laser modes explaining why the repetition rate is not doubled along with the carrier frequency. Nevertheless we are referring to it as second harmonic generation (SHG).

Using a frequency comb for high resolution 2-photon spectroscopy the modes add pair wise to the energy difference between the ground and excited levels as pointed out by E.V. Baklanov and co-workers a long time ago [12]. Ideally the full set of modes contribute to the excitation rate while the width of an individual mode sets the laser line width. Thus, for 2-photon spectroscopy, a frequency comb can therefore be entirely equivalent to cw excitation [13, 14, 15].

2. Experimental set up

Our frequency quadrupling system starts with 1.6 W of 820 nm from a mode-locked Ti:sapphire laser (Spectra Physics, Tsunami) with a repetition rate of 82 MHz that is pumped by a frequency doubled Nd:vanadate laser (Coherent, Verdi V10). Its pulse duration was determined with a background-free auto correlation (Femtoscope, MC2) to $\tau_\omega = 1.3$ ps. Using an optical spectrum analyzer (Ando, AQ-6315A) we find that the spectrum is best described by a sech^2 function with a bandwidth of $\Delta\nu_\omega = 0.24$ THz indicating a time bandwidth product at the Fourier limited of 0.315.

As shown in Fig. 1 we stabilize this laser to an external reference cavity that is well isolated from acoustics and temperature variations. The required error signal is generated with the Pound-Drever-Hall method [16] while feeding back on a piezo driven folding mirror of the laser. The spectral width of the laser is sufficiently narrow to operate this servo system exactly as in the cw case when the free spectral range of the reference cavity and the pulse repetition rate are at a (small) integer ratio (1:10 in our case). An acousto-optic modulator allows for tuning the laser relative to the reference cavity. Its moderate finesse (≈ 300) allows to additionally lock the repetition rate of the laser to a precise radio frequency reference without impairing the first lock. The built in Gires-Tournois interferometer, which is used to adjust the round trip group delay, can be utilized for this purpose. In this way this laser is frequency stabilized for high resolution spectroscopy [14].

For the first frequency doubling stage (820 nm $\rightarrow$ 410 nm), both LBO and BBO are suitable as they have good transparency and resistance to damage at high average power. While BBO has a 2.6-times larger nonlinear coefficient, we instead choose LBO because of its lower dispersion and smaller walk-off angle ($\delta_{\text{LBO}} = 15.6$ mrad versus $\delta_{\text{BBO}} = 66.8$ mrad). This provides a longer interaction length for better spatial mode profile of the second harmonic. The 10 mm long crystal is Brewster cut with $\theta = 90^\circ$ and $\phi = 29.6^\circ$ for type I phase matching. It is placed in an aluminum mount which is attached to a Peltier element to heat the crystal to 45°C. Even though the temperature of the aluminum mount is measured (sensor AD590) and controlled within 0.1°C we don't have access to the temperature profile inside the crystal.

#108584 - $15.00 USD Received 10 Mar 2009; revised 22 Apr 2009; accepted 22 Apr 2009; published 15 May 2009

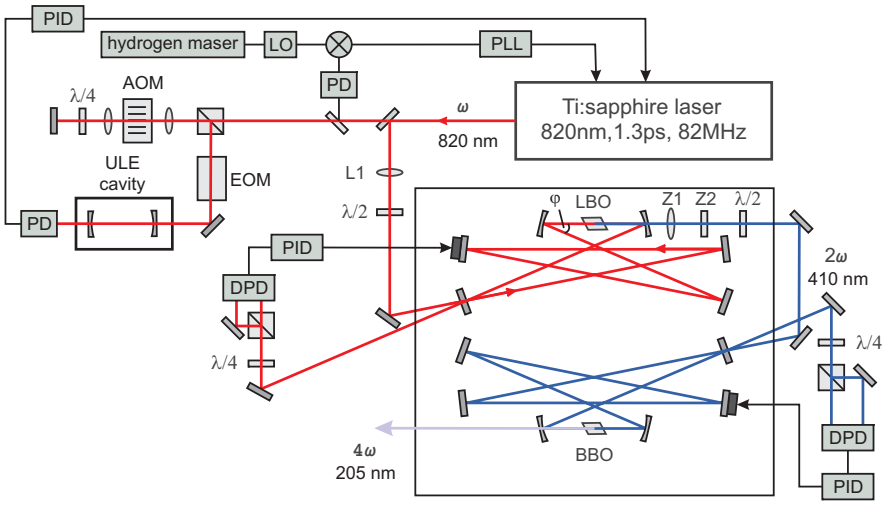

Fig. 1. Experimental setup for deep UV frequency comb generation. A 82 MHz ps mode locked Ti:sapphire laser is stabilized to an external reference cavity and frequency doubled twice with the help of resonant enhancement cavities. The first cavity houses an LBO (820 nm $\rightarrow$ 410 nm) and the second one a BBO crystal (410 nm $\rightarrow$ 205 nm), both of them are Brewster cut. L1: spherical mode matching lens ($f = 2000$ mm); Z1, Z2: cylindrical mode matching lenses ($f1 = 150$ mm and $f2 = 230$ mm focusing horizontally and vertically respectively); PD: photo diode; DPD: difference photo diode; EOM: electro-optic modulator; AOM: acousto-optic modulator; ULE: ultra-low-expansion glass; PID: proportional-integral-derivative controller; PLL: phase locked loop, LO: local oszillator.

As shown in Fig. 1 the crystal is placed in a 6 mirror cavity that is arranged to allow full folding angles of $\varphi = 16^\circ$ on the curved mirrors in order to compensate astigmatism [17]. The two focusing mirrors have a radius of curvature of r=200 mm, so that an almost spherical beam waist radius of $w_0 = 28\ \mu$m is obtained. This is somewhat below the optimum focusing condition [18] but helps to limit unwanted nonlinearities. In any case, the single pass conversion efficiency is large enough that the process is conversion loss dominated. In this case, the overall efficiency is independent of the single pass conversion efficiency, provided the proper impedance matching is worked out by picking the correct input coupler transmission. Experimentally we find that a 75 % reflectivity at 820 nm is close to optimum at the given power level of the driving laser, which means that the single pass conversion is around 25%. The remaining mirrors are high reflective at 820 nm ($R > 99.9$ %). The cavity is locked to resonate with the modes of the laser by using the polarization method [19] and feeding back on a piezo-mounted plane folding mirror. Despite Fresnel losses of 20 % for the s-polarized 2nd harmonic at the crystals end facet we obtain 600 mW average power (38 % conversion efficiency) at 410 nm through one of the curved mirrors ($T > 90$ %) uninterrupted for hours.

We are aware of three nonlinear crystals that can be used for the second doubling stage: BBO, $KBe_2BO_3F_2$ (KBBF) [20] and $Sr_2Be_2B_2O_7$ (SBBO) [21]. The nonlinear coefficient for KBBF is $d_{\mathrm{eff}}(\mathrm{KBBF}) = 0.36$ pm/V [22] and is comparable to the coefficient of BBO $d_{\mathrm{eff}}(\mathrm{BBO}) = 0.35$ pm/V. SBBO should have a comparable or even larger nonlinear coefficient than KBBF [21]. However both KBBF and SBBO are not commercially available, which leaves BBO (Type I: 410 nm (o) $\rightarrow$ 205 nm (e)) as the only present option for us. The phase matching

#108584 - $15.00 USD Received 10 Mar 2009; revised 22 Apr 2009; accepted 22 Apr 2009; published 15 May 2009

angle for SHG at 205 nm in BBO of $\theta_{\mathrm{BBO}} = 86.4^\circ$ is unfavorably close to the cut off. We cool the crystal down to -10°C which shifts the phase matching angle by about 1° and increases the effective nonlinearity to $d_{\mathrm{eff}}(\mathrm{BBO}) = 0.35$ pm/V as compared to $d_{\mathrm{eff}}(\mathrm{BBO}) = 0.31$ pm/V at room temperature. Even lower temperatures have been used to further enhance the efficiency [23].
In our set up the BBO crystal is held in a copper mount which is attached to a thermoelectric cooler to servo control its temperature in the same way as the LBO crystal. To prevent condensation and convection we use 32 mm tubes oriented along the laser that are purged with a steady flow of dry oxygen away from the crystal housing.

The 410 nm enhancement cavity is very similar to the first doubling cavity except that the curved mirrors have a radius of curvature of $r = 175$ mm arranged such that they give a 17 μm beam waist in the crystal. We find the optimum configuration for the 205 nm light employs an input coupler with 93 % reflectivity, all the other mirrors highly reflective at 410 nm ($R > 99$ %) and a 5 mm long Brewster-cut BBO crystal. Fresnel losses at the crystals end face amount to 23 %. Nevertheless we extract up to 70 mW of average power at 205 nm through one of the focusing mirrors ($T > 95\%$) albeit for a short period of time only (see below).

3. Results and discussions

There are several effects that can change the pulse duration upon second harmonic generation. For perfect phase matching of all wavelength components and a small input signal, the temporal pulse envelope is simply squared which gives rise to a temporal pulse narrowing by $\sqrt{2}$ for Gaussian pulses and by a factor of 1.45 for sech^2 pulses, without introducing a frequency chirp. However in a real crystal, phase matching can not be achieved for all wavelengths simultaneously so that the second harmonic spectrum $I_2(\Omega)$ is modified. In the plane wave limit we have [24]:

$$I_2(\Omega, L) \sim L^2 \,\mathrm{sinc}^2 \left\{ \left[\left(\frac{1}{v_2} - \frac{1}{v_1} \right) \Omega + \Delta k \right] \frac{L}{2} \right\} \times I_1^2(\Omega). \tag{1}$$

Here the spectrum of the fundamental wave is given by $I_1(\Omega)$ with the detuning from the carrier frequency Ω for which we can always adjust for proper phase matching, i.e. $\Delta k = 0$. The different frequency dependencies of the refractive indices expressed through the group velocities v_1 and v_2 are limiting the phase matching bandwidth by spectral filtering with the sinc^2-function. In the time domain the fundamental and SHG pulses separate upon propagation causing a pulse broadening of the latter. Interestingly this pulse broadening does not affect the time bandwidth product in the case of Fourier limited fundamental pulses.

Another pulse broadening effect shows up for larger conversion efficiencies that go beyond the quadratic approximation of Eq. (1). In this case the second harmonic saturates during the peak of the incoming pulse[24]. With no intensity dependent phases these effects do not introduce a chirp. Obtaining essentially chirp free pulses is important for the two photon excitation rate as discussed above.

At the first doubling stage the temporal walk-off of the 820 nm and 410 nm pulses in our 10 mm LBO crystal amounts to 1.1 ps corresponding to a phase matching bandwidth of 0.88 THz defined at the points where the argument of the sinc function in Eq. 1 varies between $\pm\pi$. In addition, due to the large single pass conversion efficiency, some saturation broadening is expected. To verify that these effects go along with a corresponding spectral narrowing, the spectrum at 410 nm was measured with an optical spectrum analyzer and found to posses a nearly sech^2 shape with a width of $\Delta\nu_{2\omega} = 0.32$ THz. The pulse duration was then measured by cross correlating the 410 nm pulses with the pulses from the laser by difference frequency generation in a 2.5 mm BBO crystal. Within this crystal the temporal walk-off between the 820 nm and the 410 nm pulses amounts to 0.45 ps with the crossing angle limiting the in-

#108584 - $15.00 USD Received 10 Mar 2009; revised 22 Apr 2009; accepted 22 Apr 2009; published 15 May 2009

teraction length to slightly shorter distances. This corresponds to a temporal broadening of the observed cross correlation by 0.315×0.45 ps $= 0.14$ ps assuming the sech^2 pulse shape is maintained. The duration of the cross correlation can then be calculated from the relation $\tau_{\mathrm{DF}} \approx (\tau_\omega^p + \tau_{2\omega}^p + (0.14\ \mathrm{ps})^p)^{(1/p)} = 1.9$ ps, with $p = 1.615$ [25] to $\tau_{2\omega} = 1.1$ ps. The generated 410 nm pulses are somewhat shorter than the seed pulses albeit not by a factor of 1.45 as expected for a perfect frequency doubler with infinite phase matching bandwidth. The small deviation of the time bandwidth product from the Fourier limit (0.35 rather than 0.315) may be attributed to alignment dependent properties of the laser pulses that causes the initial pulse duration to vary.

In the second doubling cavity the temporal walk-off between the 410 nm and 205 nm pulses is much larger. After the crystal length of $L = 5$ mm they separate by 6.5 ps, so we expect a pulse broadening by approximately 0.315×6.5 ps $= 2.1$ ps if all pulse shapes are again assumed to maintain their sech^2 envelope. This GVM corresponds to a phase matching bandwidth of 0.15 THz at 410 nm. The resulting spectral bandwidth at 205 nm is determined with a monochromator (Jobin Yvon, HR640) to $\delta\nu_{4\omega} = 0.14$ THz resulting in a Fourier limited pulse duration of 2.2 ps. The actual pulse duration is determined by cross correlating the 205 nm pulses with those at 820 nm. In this case however an even thinner BBO crystal of 0.1 mm thickness was used so that temporal walk-off in the cross correlation can be neglected. Assuming $\tau_\omega \ll \tau_{4\omega}$ we determine the pulse duration to be $\tau_{4\omega} = 2.4$ ps giving rise to a time bandwidth product of 0.34. This is close enough to the Fourier limit that it seems safe to assume un-chirped pulses at 205 nm. Figure 2 displays the cross correlations and spectra while Table 1 summarizes the average powers, pulse durations and spectral widths and time bandwidth products (TBP) for all three wavelengths.

Table 1. Overview about the characteristics of the laser system

λ [nm]	$\Delta\nu$ [THz]	NL crystal	output power	acceptance bandwidth	GVM	pulse duration	TBP
820.58	0.24		1.6 W			1.3 ps	0.31
410.29	0.32	LBO	600 mW	0.88 THz	1.1 ps	1.1 ps	0.35
205.15	0.14	BBO	25 mW	0.15 THz	6.5 ps	2.4 ps	0.34

As mentioned above, the maximum power in the deep UV was 70 mW achieved with a 5 mm long BBO crystal. Stability wise we observe several phenomena that prevents the use of the full power for a longer time: Within seconds after locking the second doubling cavity the power drops to about 10 %. Lowering the temperature and/or adjusting the angle of the crystal this output power can be restored. This behavior suggests that heating of the crystal after locking causes a phase mismatch [6]. In addition, after this readjustment a further slower decrease of the power takes place within about 20 minutes settling at around 25 mW. Shifting the crystal transversely regains the power which then drops again within several minutes. The power decrease on the longer time scale might be attributed to the photo chemical reactions at the surface of the crystal that may be reduced under an oxygen atmosphere [6] as described above. Besides we could not observe a counter propagating wave in the cavity, which would indicate photo refractivity. The observed time scales for the power decrease strongly depend on the crystal dimensions. For short crystals of 1 mm and 2 mm length and aperture of 5×5 mm^2 cooling is less efficient resulting in reduced stability.

Our Monte Carlo simulations show that a tightly focused beam at 205 nm of 25 mW should generate a $1S-3S$ excitation rate of 10^{-9} per atom in a thermal beam of 6K. However high resolution would require to work with a larger focus in order to reduce time of flight broadening. For this reason we are planning to use a third enhancement cavity at 205 nm which should

#108584 - $15.00 USD Received 10 Mar 2009; revised 22 Apr 2009; accepted 22 Apr 2009; published 15 May 2009

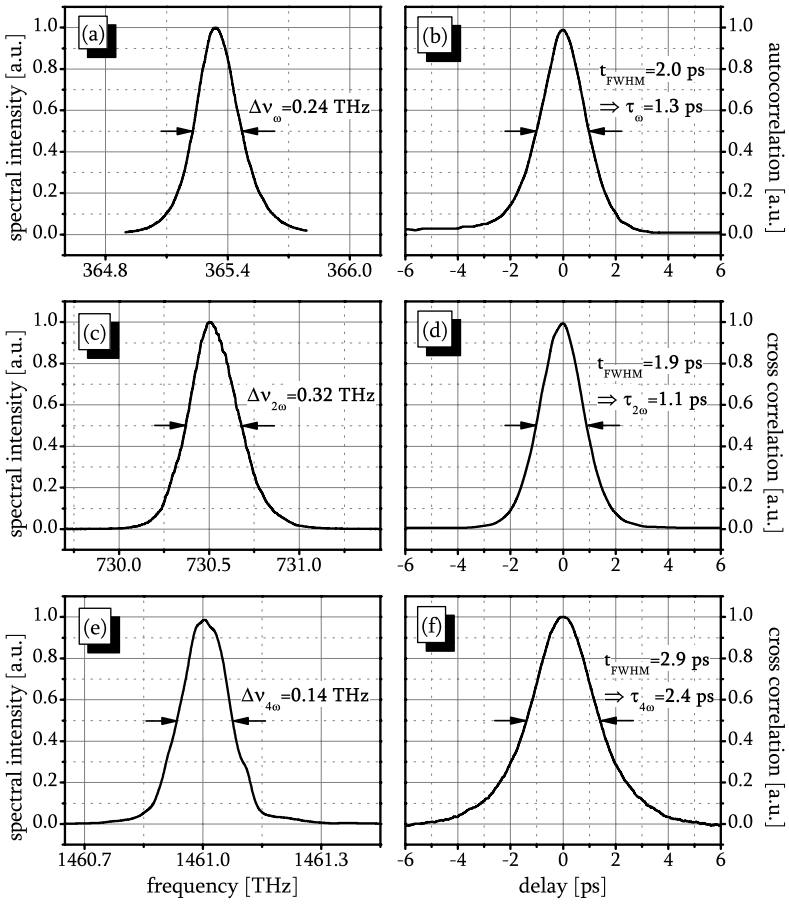

Fig. 2. Power spectra and correlation measurements for the fundamental, second harmonic and fourth harmonic pulses.(a) Power spectrum and (b) auto correlation trace of the fundamental pulses at 820 nm. (c) Power spectrum and (d) cross correlation trace of the second harmonic pulses at 410 nm. (e) Power spectrum and (f) cross correlation trace of the fourth harmonic pulses.

produce a detectable signal. In the future we might optimize the crystal dimensions for lengths and improved thermal contact in order to gain higher UV power with better long term stability. In addition longer pulses might be more efficient for our application, since direct comb spectroscopy is largely independent of pulse duration. Using longer pulses the whole spectrum can be frequency doubled without restrictions due to the phase matching bandwidth, as it is the case for the 1.1 ps pulses at 410 nm.

#108584 - $15.00 USD Received 10 Mar 2009; revised 22 Apr 2009; accepted 22 Apr 2009; published 15 May 2009

4. Conclusion

In summary we demonstrated an all solid state deep-UV laser operating at 205 nm suitable for driving the 1S – 3S 2-photon resonance in atomic hydrogen. Starting with an 82 MHz ps laser with 1.6 W at 820 nm a maximum output power of 70 mW at 205 nm is achieved by two resonant second harmonic generation stages with an overall efficiency of 4.5 %. Cross correlation measurements revealed temporal pulse broadening but the corresponding spectral narrowing suggests that essentially un-chirped 2.4 ps pulses at 205 nm are generated.

Acknowledgements

This research was partially supported by the DFG cluster of excellence "Munich Center for Advanced Photonics".

#108584 - $15.00 USD Received 10 Mar 2009; revised 22 Apr 2009; accepted 22 Apr 2009; published 15 May 2009

PHYSICAL REVIEW A **81**, 033427 (2010)

Two-photon direct frequency comb spectroscopy with chirped pulses

S. Reinhardt, E. Peters, T. W. Hänsch, and Th. Udem
Max-Planck-Institut für Quantenoptik, Hans-Kopfermann-Strasse 1, DE-85748 Garching, Germany
(Received 21 September 2009; published 31 March 2010)

Thanks to the high peak intensities of ultrashort pulse trains that make up an optical frequency comb, conversion to much shorter wavelengths is readily available. Therefore direct frequency comb spectroscopy may offer the possibility of extending high-resolution spectroscopy to spectral regions that are unexplored so far. In this work, we investigate the impact of a chirp, i.e., a varying frequency across the pulses, on the excitation rate obtainable with two-photon direct frequency comb spectroscopy. Using the cesium $6\,^2S_{1/2}$-$8\,^2S_{1/2}$ two-photon transition at 822 nm, we show that destructive interference of various quantum paths reduces the excitation rate with the inverse of the time bandwidth product of the exciting pulses.

DOI: 10.1103/PhysRevA.81.033427 PACS number(s): 32.80.Qk, 32.30.Jc, 32.70.Jz

I. INTRODUCTION

Since the introduction of optical frequency combs [1], several applications have emerged in various fields such as optical frequency measurements, optical atomic clocks [2], attosecond pulse generation [3], and uses in precision astronomy [4]. Yet another possibility is to use them for direct frequency comb spectroscopy (see [5] and references therein). This approach seems to have no real advantage for metrology at wavelength regions where continuous-wave lasers exists. However, thanks to the high peak power of short laser pulses, it might allow us to push high-resolution spectroscopy to thus far inaccessible regions such as the extreme ultraviolet (XUV). Many transitions of fundamental interest occur there such as the $1S$-$2S$ transition in He^+, which may be exited with two photons at 61 nm [6]. This wavelength would be available as the 13th harmonic of a femtosecond Ti:sapphire mode locked laser, for example. As the available XUV powers are currently at the brink of allowing useful transition rates [7], any reduction, for example, by possible frequency chirps of the pulses, is important. Such a chirp may be due to the frequency conversion process, the source laser, or beam handling. The purpose of this paper is to investigate its impact on the metrologically relevant two-level two-photon transition rate. We derive a compact expression that is valid for most laboratory situations and relates the achievable transition rate to the time bandwidth product of the exciting pulses. We then compare this result with experimentally determined transition rates in the infrared and find good agreement with a large set of different frequency chirps.

The practical cutoff for up conversion using nonlinear crystals is set by phase matching and transparency requirements. Currently the shortest wavelengths that can be phase matched for second harmonic generation with commercially available crystals such as β-barium borate (BBO) is around 205 nm, while other crystals such as lithium triborate (LBO) transmit down to 160 nm. Much shorter wavelengths can be generated in a spatially localized gas jet by the process of high harmonic generation (see [8], for example). In this case, pulsed lasers are required as a driver to provide the high peak intensity that is necessary. When using a coherent pulse train for that purpose, individual continuous-wave modes of the resulting comb structure might be used as narrow-band laser sources [7,9,10].

Direct frequency comb spectroscopy had already been proposed in 1977 by Y. V. Baklanov and V. P. Chebotayev [11] to solve a very similar problem. Lacking suitable crystals at that time, only pulsed generation of 243 nm laser radiation required for the $1S$-$2S$ two-photon transition in atomic hydrogen seemed possible. The invention of suitable nonlinear crystals like BBO has made that effort unnecessary. Nevertheless, the first direct frequency comb spectroscopy was performed shortly thereafter on the sodium $3\,^2S_{1/2}$-$4\,^2D$ transitions and obtained close to natural line width of 4 MHz with a 1 GHz wide frequency comb [12].

Much broader frequency combs generated by femtosecond pulses have been used by Meshulach and Silberberg [13] and by Stowe and co-workers [14,15]. By using a spatial light modulator, they investigated the influence on various spectral phases on the Cs $6\,^2S_{1/2}$-$8\,^2S_{1/2}$ and Rb $5\,^2S_{1/2}$-$5\,^2D_{3/2}$ excitation rates. Two cases have to be distinguished when investigating these transition rates. Because of the large spectral width of ultrashort pulses, intermediate levels may be involved in a competing stepwise single-photon excitation. In this case, the behavior is more complex and permits pulse chirping to enhance the transition rate relative to the excitation with transform-limited pulses [16,17]. In contrast to this, chirping of a pulse can only reduce the transition rate from the maximum transform-limited value when dealing with a two-photon transition where stepwise single-photon excitation via intermediate levels can be neglected.

II. DIRECT FREQUENCY COMB SPECTROSCOPY

A frequency comb is represented by a regular array of optical modes ω_n that are separated by the pulse repetition rate ω_r of the mode locked laser that generates them: $\omega_n = n\omega_r + \omega_0$. The integer n numbers the modes as $n = 0, \pm1, \pm2, \ldots$, while the combs center mode is defined to belong to $n = 0$ and is related to the carrier envelope offset frequency [1]. In the time domain, the pulse train that generates such a comb can reach peak powers that exceed the time-averaged power by the number of active modes. With further amplification [3] or enhancement in a matched optical cavity [18,19], high-order harmonics may be generated in a gas target. Soft x-rays have been produced this way albeit with a rather low repetition rate of 1 kHz [20]. In fact, the high-order harmonics are expected to be subject to frequency chirping which may be

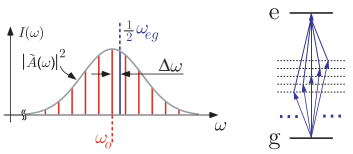

FIG. 1. (Color online) Left: direct two-photon frequency comb spectroscopy. If one of the modes (ω_0) is tuned on resonance ($\Delta\omega = \frac{1}{2}\omega_{eg} - \omega_0 = 0$), all other modes combine pairwise to deliver the transition energy $\hbar\omega_{eg}$. Right: for constructive interference of all excitation paths, the modes of the frequency comb must be properly phased.

precompensated by a suitable chirp of the fundamental laser pulses [21].

As sketched in Fig. 1, a narrow-band two-photon transition can be excited effectively by the combined action of all modes [22]. By tuning any of the modes ω_n to half the transition energy, all mode pairs m with $\omega_{n+m} + \omega_{n-m}$ can contribute to the transition rate [11]. The same pairwise addition of photon energies takes place if the comb is tuned such that the two-photon transition occurs exactly between two comb modes. According to Parseval's theorem, the combined power of all modes is identical to the time-averaged power of the pulse train. It can be shown that the ac Stark shift derives from the time-averaged intensity rather than from the peak intensity of ultrashort pulses [23]. In the ideal case, driving a two-photon transition with a frequency comb is therefore equivalent to the excitation with a continuous-wave laser of the same average intensity. It should be noted, however, that this type of pulsed excitation takes place only in a small volume, which may lead to significant time-of-flight broadening unless trapped ions or cold atoms are used.

The coherent addition of the quantum paths m as shown at the right-hand side of Fig. 1 leading from the ground state to the excited state is entirely constructive if all modes of the comb are in phase. This could be the case for a Fourier-limited pulse train. Deviations from this condition in terms of a spectral phase, which is symmetric relative to the atomic transition, will lead to a partial destructive interference. Hence the excitation rate is reduced. On the other hand, any antisymmetric phase perturbation does not reduce the transition rate as it cancels in the pairwise addition of modes. For applications in high-resolution spectroscopy, it is important to note that such a chirp does not lead to systematic shift of the observed transition frequencies as long as these phase shifts are constant in time.

As a model system, we use the cesium $6\,^2S_{1/2}$-$8\,^2S_{1/2}$ two-photon transition excited with a frequency comb which is generated by a picosecond Ti:sapphire mode locked laser tuned to 822 nm [23]. Under these conditions, no intermediate levels are addressed by the laser. Spectroscopy is performed by two counter-propagating pulse trains with the pulse collision point located in the center of a cesium gas cell. This arrangement allows the thermal cesium atoms to absorb two photons from opposing directions such that the Doppler effect cancels in first order. The Doppler-free signal sits on a Doppler-broadened background that is due to the absorption of both photons from either side [24]. The pulse collision point is imaged onto

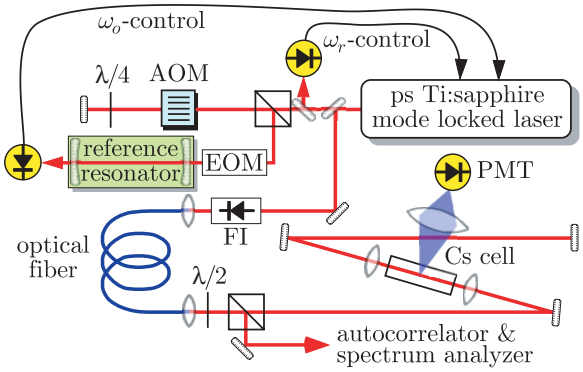

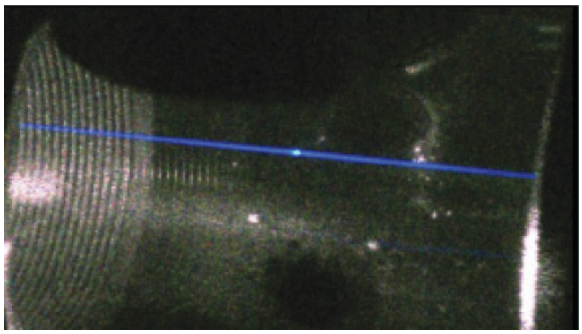

FIG. 2. (Color online) Top: Experimental setup. Two counter-propagating beams from a stabilized ps mode locked Ti:sapphire laser are superimposed in a 10 cm Cs vapor cell at room temperature. The pulses are chirped with a set of optical fibers (FI = Faraday isolator, AOM = acousto optic modulator, EOM = electro optic modulator, PMT = photomultiplier tube). Bottom: Image of the excitation volume with fluorescence at 456 nm from the decaying $8\,^2S_{1/2}$ via the $7\,^2P$ levels. The pulse collision volume, where the Doppler-free excitation takes place, appears as a bright spot in the center. Doppler-broadened excitation takes place all along the laser beam.

the cathode of a photomultiplier tube collecting the 456 nm photons emitted upon decay via the $7P$ states (see Fig. 2); a typical spectrum is shown in Fig. 3.

The only stable isotope of Cs possesses a nuclear spin of $7/2$ so that both the excited and the ground state are split into two hyperfine states with total angular momentum $F = 3$ and $F = 4$. The selection rules for two-photon transitions [25] allow only $\Delta F = 0$ for identical linear polarizations used here. As the frequency comb is scanned, this doublet repeats itself with half the repetition rate so that the separation of the hyperfine components of ~4.2 GHz appears modulo the repetition rate.

III. THEORETICAL MODEL

For practical purposes, there are two main mechanisms that usually chirp short pulses: Propagation through a medium with self phase modulation (SPM) via an intensity dependence of the refractive index and/or dispersive media with group velocity dispersion (GVD). While pure SPM causes the pulses to broaden in the frequency domain, GVD broadens the pulses

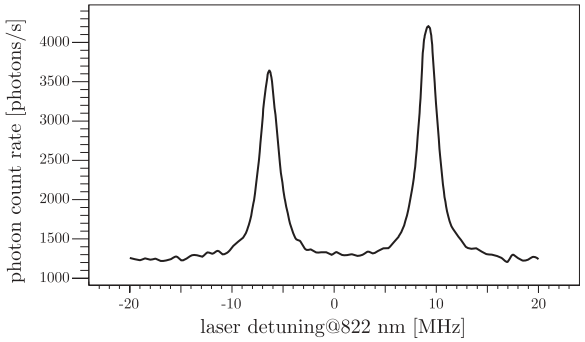

FIG. 3. Example of the Doppler-free signal (count rate up to several kHz) from the pulse collision point shows two allowed hyperfine components ($F = 3 \rightarrow F = 3$ and $F = 4 \rightarrow F = 4$) of the $6\,^2S_{1/2}$-$8\,^2S_{1/2}$ transition.

in the time domain without corresponding spectral broadening. In both cases, the time bandwidth product is larger than the Fourier limit. Often both SPM and GVD are contributing, for example, when launching a pulse train into an optical fiber. We restrict our analysis to these common chirp mechanisms and ignore more exotic spectral phases that can be generated with a spatial light modulator [13].

We model the electric field of a single pulse at the pulse collision point $z = 0$ as $E(t) = E_0 A(t) \exp(-i\omega_0 t)$ with a complex envelope function $A(t)$ and $\tilde{A}(\omega)$ in the time and frequency domains, respectively. The field at any other axial position will be obtained by replacing $t \rightarrow t \pm z/c$ with the sign defining the propagation direction. The pulse chirp is measured with a complex chirp parameter $a + ib$:

$$A(t) = \frac{(2a/\pi)^{1/4}}{\sqrt{\tau}}\; e^{-(a+ib)(t\pm z/c)^2/\tau^2}, \tag{1}$$

$$\tilde{A}(\omega) = \left(\frac{a}{2\pi}\right)^{1/4} \sqrt{\frac{\tau}{a+ib}}\; e^{-\frac{(\omega\tau)^2}{4(a+ib)} \pm i\omega z/c}. \tag{2}$$

While $a = 1$ and $b = 0$ correspond to the unchirped pulse of duration $\tau\sqrt{2\ln(2)}$, the normalization is chosen such that the pulse energy $\int |E(t)|^2 dt$ is independent of the chirp. In general the chirp parameter will be time dependent, causing frequency chirps that are nonlinear in time. In a medium with pure SPM, i.e., with an intensity-depending refractive index $n(I) = n_0 + n_2 I(t)$, the chirp will be proportional to the time derivative of the temporal pulse envelope, i.e., $\propto \partial |A(t)|^2/\partial t$. In the vicinity of the peak, the chirp may be approximated by a linear function. Only even-order dispersion leads to the reduction of the transition rate that is of interest here. Our choice of the chirp parameter excludes spectral phases that are antisymmetric with respect to the spectral envelope. This includes SPM by pulse envelopes that are symmetric in time, and GVD up to the third order and assumes that the atomic transition frequency is in the vicinity of the spectral center of the comb. The linear antisymmetric phase $\pm i\omega z/c$ does not reduce the excitation rate through destructive quantum interference. We show experimentally that these assumptions lead to reasonable agreement with observations for various chirp parameters and allow us to predict the transition rate for given experimental conditions.

With a constant chirp parameter, the Fourier transform pair (1) and (2) yield the time domain and frequency domain intensity full widths at half maximum as $\Delta t = \tau\sqrt{2\ln(2)/a}$ and $\Delta\nu = \sqrt{2\ln(2)(a + b^2/a)}/\pi\tau$, so the time bandwidth product (TBW) is given by

$$\Delta\nu\,\Delta t = \frac{2\ln(2)}{\pi}\sqrt{1 + \left(\frac{b}{a}\right)^2}. \tag{3}$$

Pure time domain broadening means that $b^2 = a(1 - a)$, whereas $a = 1$ must hold for pure frequency domain broadening.

The time domain description of the pulse train is given by

$$E(t) \propto \sum_{n=-\infty}^{\infty} \tilde{A}(n\omega_r) e^{-i(n\omega_r + \omega_0)t}, \tag{4}$$

where we assumed that the spectral envelope is centered at ω_0. Using standard second-order perturbation theory as in [26] for the amplitude of the excited state c_e of an atom at rest, we derive

$$\begin{aligned} |c_e|^2 &\propto \left| \sum_{n,m} \frac{\tilde{A}(n\omega_r)\tilde{A}(m\omega_r)}{i(\Delta\omega + (n+m)\omega_r) + \gamma/2} \right|^2 \\ &\propto \frac{1}{\Delta\omega^2 + \gamma^2/4}\,\frac{a\tau^2}{a^2 + b^2} \left| \sum_n e^{-\frac{(n\omega_r\tau)^2}{2(a+ib)} + 2in\omega_r z/c} \right|^2 \\ &\approx \frac{1}{\Delta\omega^2 + \gamma^2/4}\,\frac{1}{\Delta\nu\,\Delta t}\, e^{-\frac{8\ln(2)z^2}{c^2\Delta t^2}}, \end{aligned} \tag{5}$$

where $\Delta\omega$ is the detuning of ω_0 from the two-photon resonance. Off-resonance terms with $n \neq -m$ have been ignored, and the sum has been approximated by an integral assuming a sufficient number of modes (≈5000 in our case). The transition probability reduces as $(\Delta\nu\Delta t)^{-1}$ for any position z and any detuning. The reduction with z is merely due to a fall off of the laser power away from the pulse collision point. Very important for metrological applications is the fact that the chirp has no influence on the line shape of the transition, at least within this model. It should also be noted that the transition rate reduction may be stronger for more exotic pulse shapes such as pulses with a rectangular spectrum [27]. In this case, even a Fourier-limited pulse with a sinc temporal envelope has a nonconstant spectral phase, and a strong chirp has very little impact on the time bandwidth product but reduces the transition rate accordingly. A similar theoretical analysis that applies for single pulse excitation of multiphoton transitions in molecules has been presented earlier by Cao and co-workers [28].

IV. EXPERIMENTAL SETUP AND RESULTS

To verify this finding experimentally, we use the setup sketched in Fig. 2. Our mode locked laser (Tsunami, Spectra Physics) is pumped with 9 W at 532 nm (Verdi V-10, Coherent) and produces close to Fourier-limited Sech^2 pulses of 1.3 ps duration with a spectral width of 0.24 THz (TBW = 0.31) with a pulse repetition rate of $\omega_r = 2\pi \times$ 82 MHz. In the following, we assume that these pulses can be approximated to be Gaussian. Out of its 1.8 W of output power, 0.2 W

is used for stabilization and wavelength determination. We lock the pulse repetition frequency to a signal derived from a synthesizer by controlling the laser cavity length with a piezo-mounted mirror. At the same time, the combs center frequency is stabilized to reference cavity with the usual Pound-Drever-Hall method [29] that also works for pulsed lasers. The cavity's free spectral range and ω_r are at an integer ratio (10 in our case). An electro-optic modulator (EOM) in front of the cavity generates the required sidebands, while an acousto-optic modulator (AOM) is used to scan the comb across the Cs transition.

To impose a chirp on the pulses, two different optical fibers, a polarization-maintaining single-mode fiber (PSM) (F-SPF, Newport) and a photonic crystal fiber (PCF) (LMA-20, CrystalFiber) were used. The PCF has a larger mode field diameter (15 μm) than the PSM (4.2 μm) so that the SPM is reduced. To characterize the SPM and GVD of the fibers, two length scales, the nonlinear and dispersive lengths z_d and z_{nl}, have been introduced [30]:

$$z_d = \frac{\Delta t^2}{4\ln(2)|k_0''|}, \quad z_{nl} = \frac{\pi}{2kn_2 I_0}, \tag{6}$$

where k'', the second derivative of the wave vector versus optical frequency, measures the GVD, and I_0 the pulse peak intensity. The dispersive length is the travel distance where the GVD broadens the pulse duration by $\sqrt{2}$. Similarly, after traveling the nonlinear length, the maximum spectral phase shift through SPM amounts to $\phi = \pi/2$. For a given fiber length L, two propagation regimes have to be distinguished: $L \ll z_{nl}$ but $L \sim z_d$ and $L \ll z_d$ but $L \sim z_{nl}$. In the first case, SPM is negligible; while in the latter case, GVD can be neglected. With the fibers at hand, z_d is around 15 m and z_{nl} has been varied between 0.01 m (for the PSM fiber at 1 W) to 10 m (for the PCF fiber at 10 mW) by successive shortening. In all cases, SPM is the larger effect.

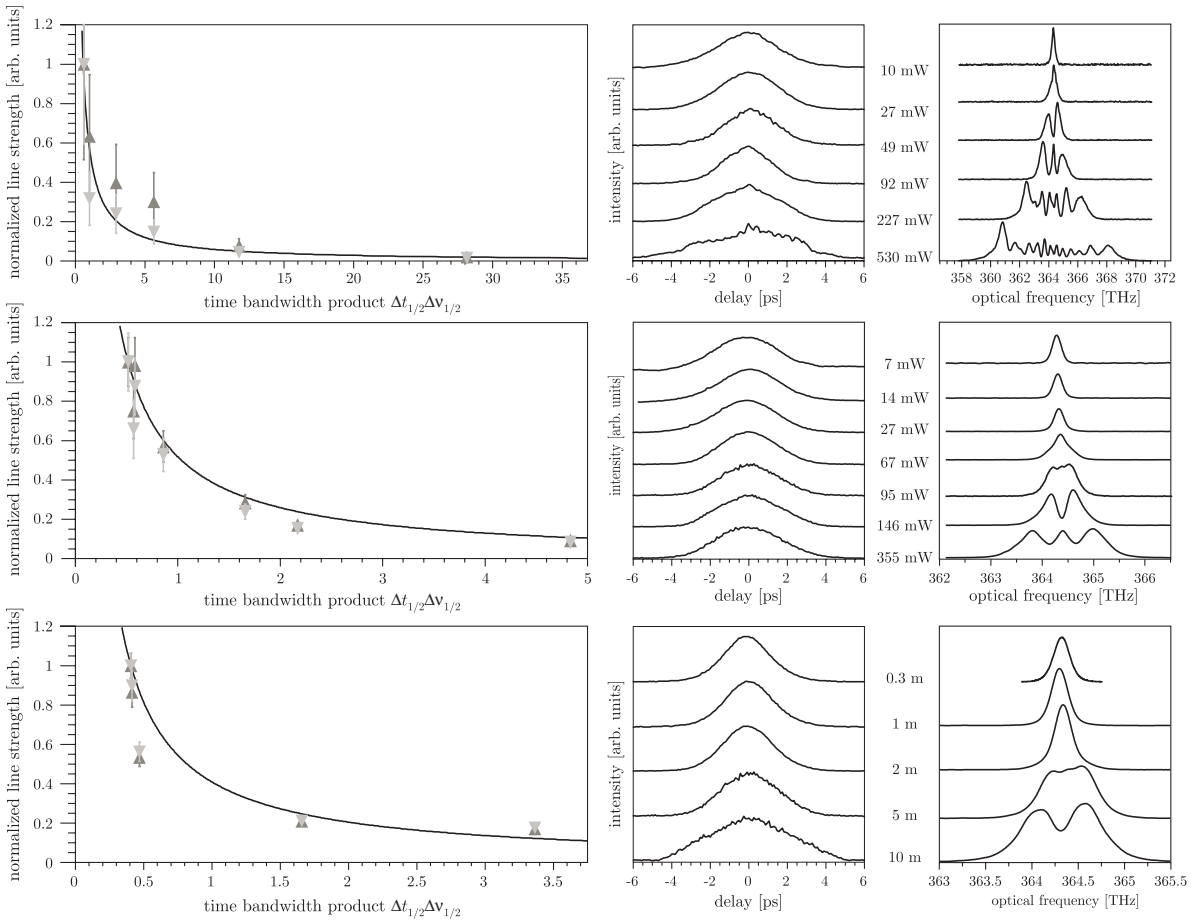

FIG. 4. Left: Normalized Doppler-free line strength versus time bandwidth product of the exciting pulses ($F = 4$: ▲ and $F = 3$: ▼). The solid line shows the theoretical line reduction according to Eq. (5) normalized to the unchirped transition rate. Right: The corresponding autocorrelation traces and pulse spectra after chirping with various chirp parameters (curves of-set for clarity). Top: Laser pulses are chirped by a single-mode polarization-maintaining fiber (PSM) of 1 m length. Center: The chirp is generated with a large-mode field diameter photonic crystal fiber (PCF) of 5 m length. Bottom: Same as center but for different fiber lengths and similar power levels: 0.3 m (84 mW), 1 m (81 mW), 2 m (86 mW), 5 m (95 mW), and 10 m (115 mW).

After the fiber, an adjustable fraction of the power is branched off to feed an autocorrelator (MC2, Femtoscope) in order to determine the pulse length Δt of the chirped pulses. In addition, an optical spectrum analyzer is used to determine the spectral width $\Delta\nu$. The waist diameter in the cell is around 50 μm. To detect the fluorescence at 456 nm, a photomultiplier tube (R6358, Hamamatsu) with an imaging system is used. An interference filter with a central wavelength of 450 nm and a width of 15 nm reduces the background from the laser and other light sources. The transmission through the filter is 63%, and the overall detection efficiency is around 0.5%.

By varying the fiber lengths and power levels coupled through the fibers, we can generate a large set of different chirp parameters. Measuring the spectral and temporal width as well as the transition rate, we can then verify Eq. (5). With the PCF fiber of 5 m length, the TBW could be varied over one order of magnitude (see center of Fig. 4).

To reach even larger TBWs, the same measurement was carried out with a single-mode polarization maintaining (PSM) fiber that possesses a smaller mode field diameter. In this case, the SPM contribution is much larger, and the TBW can vary by two orders of magnitude with only 1 m of fiber. The agreement between the measured line strength and expectation is acceptable. The observed transition rates shown in Fig. 4 are normalized to the square of the laser power measured with an accuracy ± 5 % in the beam traversing the cell. We tried to maintain the same focusing conditions cutting the incoupling end of the fiber, not touching the output facet. The transition rates are also normalized to the smallest TBW measured after the fiber. The excitation volume that varies with the pulse duration has also been divided out by multiplying Eq. (5) with the temporal pulse width.

V. DISCUSSION

As can be seen from the autocorrelation traces and spectra, the deviation from a linear chirp, i.e., Gaussian pulse shape and spectrum, are significant under some of the conditions investigated. Nevertheless the observed reduction of the excitation rate follows nicely the predictions of the simple theory developed here allowing us to estimate the reduction by the readily available time bandwidth product. For pulse shapes that largely differ from a Gaussian, the simple theory will not hold. Even though the transition rate reduction with the the chirp parameter is similar, it may not increase the time bandwidth product accordingly [27].

ACKNOWLEDGMENTS

This research was supported by the DFG cluster of excellence “Munich Centre for Advanced Photonics (MAP)”. We thank Akira Ozawa for critically reading the manuscript.

[1] Th. Udem, R. Holzwarth, and T. W. Hänsch, Nature (London) **416**, 233 (2002).
[2] S. A. Diddams, J. C. Bergquist, S. R. Jefferts, and C. W. Oates, Science **306**, 1318 (2004).
[3] A. Baltuška *et al.*, Nature (London) **421**, 611 (2003).
[4] T. Steinmetz *et al.*, Science **321**, 1335 (2008).
[5] M. C. Stowe, M. J. Thorpe, A. Pe’er, J. Ye, J. E. Stalnaker, V. Gerinov, and S. A. Diddams, in *Advances in Atomic, Molecular, and Optical Physics*, Vol. 55, edited by Ennio Arimondo, Paul Berman, and Chun Lin (Academic, New York, 2008), p. 1.
[6] M. Herrmann *et al.*, Phys. Rev. A **79**, 052505 (2009).
[7] A. Ozawa *et al.*, Phys. Rev. Lett. **100**, 253901 (2008).
[8] J. G. Eden, Prog. Quantum Electron. **28**, 197 (2004).
[9] R. Th. Zinkstok, S. Witte, W. Ubachs, W. Hogervorst, and K. S. E. Eikema, Phys. Rev. A **73**, 061801(R) (2006).
[10] D. C. Yost, T. R. Schibli, and J. Ye, Opt. Lett. **33**, 1099 (2008).
[11] Y. V. Baklanov and V. P. Chebotayev, Appl. Phys. **12**, 97 (1977).
[12] J. N. Eckstein, A. I. Ferguson, and T. W. Hänsch, Phys. Rev. Lett. **40**, 847 (1978).
[13] D. Meshulach and Y. Silberberg, Nature (London) **396**, 239 (1998).
[14] M. C. Stowe, F. C. Cruz, A. Marian, and J. Ye, Phys. Rev. Lett. **96**, 153001 (2006).
[15] M. C. Stowe, A. Pe’er, and J. Ye, Phys. Rev. Lett. **100**, 203001 (2008).
[16] D. Felinto and C. E. E. Lopez, Phys. Rev. A **80**, 013419 (2009).
[17] N. Dudovich, B. Dayan, S. M. Gallagher Faeder, and Y. Silberberg, Phys. Rev. Lett. **86**, 47 (2001).
[18] R. J. Jones, K. D. Moll, M. J. Thorpe, and J. Ye, Phys. Rev. Lett. **94**, 193201 (2005).
[19] Ch. Gohle, Th. Udem, M. Herrmann, J. Rauschenberger, R. Holzwarth, H. A. Schuessler, F. Krausz, and T. W. Hänsch, Nature (London) **436**, 234 (2005).
[20] J. Seres *et al.*, Nature (London) **433**, 596 (2005).
[21] M. Murakami, J. Mauritsson, A. L’Huillier, K. J. Schafer, and M. B. Gaarde, Phys. Rev. A **71**, 013410 (2005).
[22] V. Gerginov, C. E. Tanner, S. A. Diddams, A. Bartels, and L. Hollberg, Opt. Lett. **30**, 1734 (2005).
[23] P. Fendel, S. D. Bergeson, Th. Udem, and T. W. Hänsch, Opt. Lett. **32**, 701 (2007).
[24] W. Demtröder, *Laser Spectroscopy* (Springer, New York, 2002).
[25] K. D. Bonin and T. J. McIlrath, J. Opt. Soc. Am. B **1**, 52 (1984).
[26] T. W. Hänsch and N. C. Wong, Metrologia **16**, 101 (1980).
[27] B. Broers, H. B. van Linden van den Heuvell, and L. D. Noordam, Opt. Commun. **91**, 57 (1992).
[28] J. Cao, J. Che, and K. R. Wilson, J. Phys. Chem. A **102**, 4284 (1998).
[29] R. W. P. Drever, J. L. Hall, F. B. Kowalski, J. Hough, G. M. Ford, A. J. Munley, and H. Ward, Appl. Phys. B **31**, 97 (1983).
[30] G. P. Agrawal, *Nonlinear Fiber Optics* (Academic Press, San Diego, 2001).

Bibliography

[1] Y. V. Baklanov and V. P. Chebotayev, "Narrow resonances of two-photon absorption of super-narrow pulses in a gas," Appl. Phys. **12**, 97 – 99 (1977).

[2] E. V. Baklanov and V. P. Chebotaev, "Two-photon absorption of ultrashort pulses in a gas," Sov. J. Quantum Electron. **7**, 1252 (1977).

[3] R. Teets, J. Eckstein, and T. W. H´ansch, "Coherent two-photon excitation by multiple light pulses," Phys. Rev. Lett. **38**, 760 – 764 (1977).

[4] J. N. Eckstein, A. I. Ferguson, and T. W. Hänsch, "High-resolution two-photon spectroscopy with picosecond light pulses," Phys. Rev. Lett. **40**, 847 – 850 (1978).

[5] M. C. Stowe, F. C. Cruz, A. Marian, and J. Ye, "High resolution atomic coherent control via spectral phase manipulation of an optical frequency comb," Phys. Rev. Lett. **96**, 153001 (2006).

[6] M. C. Stowe, A. Pe'er, and J. Ye, "Control of four-level quantum coherence via discrete spectral shaping of an optical frequency comb," Phys. Rev. Lett. **100**, 203001 (2008).

[7] N. Dudovich, B. Dayan, S. M. G. Faeder, and Y. Silberberg, "Transform-limited pulses are not optimal for resonant multiphoton transitions," Phys. Rev. Lett. **86**, 47 – 50 (2001).

[8] B. Chatel, J. Degert, S. Stock, and B. Girard, "Competition between sequential and direct paths in a two-photon transition," Pys. Rev. A **68**, 041402 (2003).

[9] B. Chatel, J. Degert, and B. Girard, "Role of quadratic and cubic spectral phase in ladder climbing with ultrashort pulses," Pys. Rev. A **70**, 053414 (2004).

[10] R. Pohl, A. Antognini, F. Nez, F. D. A. F. Biraben, J. M. R. Cardoso, D. S. Covita, A. Dax, S. Dhawan, L. M. P. Fernandes, A. Giesen, T. Graf, T. W. H´ansch, P. Indelicato, L. Julien, C.-Y. Kao, P. Knowles, E.-O. L. Bigot, Y.-W. Liu, J. A. M. Lopes, L. Ludhova, C. M. B. Monteiro, F. Mulhauser, T. Nebel, P. Rabinowitz, J. M. F. dos Santos, L. A. Schaller, K. Schuhmann, C. Schwob, D. Taqqu, J. F. C. A. Veloso, and F. Kottmann, "The size of the proton," Nature **466**, 213 – 217 (2010).

[11] S. Bourzeix, B. de Beauvoir, F. Nez, F. de Tomasi, L. Julien, and F. Biraben, "Ultra-violet light generation at 205 nm by two frequency doubling steps of a cw titanium-sapphire laser," Opt. Commun. **133**, 239 – 244 (1997).

[12] M. C. Stowe, M. J. Thorpe, A. Pe'er, J. Ye, J. E. Stalnaker, V. Gerinov, and S. A. Diddams, "Direct frequency comb spectroscopy," Adv. Atom. Mol. Opt. Phy. **55**, 1 – 60 (2008).

[13] T. Udem, "Die Messung der Frequenz von Licht mit modengekoppelten Lasern," Ph.D. thesis, LMU (2000).

[14] M. Haas, U. D. Jentschura, C. H. Keitel, N. Kolachevsky, M. Herrmann, P. Fendel, M. Fischer, T. Udem, R. Holzwarth, T. W. Hänsch, and G. S. Agarwal, "Two-photon excitation dynamics in bound two-body Coulomb systems including ac Stark shift and ionization," Phys. Rev. A **73**, 052501 (2006).

[15] W. Demtröder, *Laserspektroskopie, vierte Auflage* (Springer, 2000).

[16] A. Messiah, *Quantum mechanics*, vol. 2 (North-Holland, 1961).

[17] K. D. Bonin and T. J. McIlrath, "Two-photon electric-dipole selection rules," J. Opt. Soc. Am. B **1**, 52 (1984).

[18] R. J. Jones, J. C. Diels, J. Jasapara, and W. Rudolph, "Stabilization of the frequency, phase, and repetition rate of an ultra-short pulse train to a Fabry-Perot reference cavity," Opt. Commun. **175**, 409 – 418 (2000).

[19] P. Fendel, "Präzisionsspektroskopie an Wasserstoff und Deuterium," Ph.D. thesis, LMU (2005).

[20] R. W. P. Drever, J. L. Hall, F. V. Kowalski, J. Hough, G. M. Ford, A. J. Munley, and H. Ward, "Laser phase and frequency stabilization using an optical-resonator," Appl. Phys. B **31**, 97 – 105 (1983).

[21] J.-C. Diels and W. Rudolph, *Ultrashort laser pulse phenomena* (Academic Press, 2006).

[22] G. D. Boyd and D. A. Kleinman, "Parametric interaction of focused Gaussian light beams," J. Appl. Phys. **39**, 3597 – 3639 (1968).

[23] H. Wang and A. M. Weiner, "Efficiency of short-pulse type-I second harmonic generation with simultaneous spatial walk-off, temporal walk-off, and pump depletion," IEEE J. Quantum Electron. **39**, 1600 – 1618 (2003).

[24] A. V. Smith, R. J. Gehr, and M. S. Bowers, "Numerical models of broad-bandwidth nanosecond optical parametric oscillators," J. Opt. Soc. Am. B **16**, 609 – 619 (1999).

[25] C. S. Adams and A. I. Ferguson, "Tunable narrow line width ultra-violet light generation by frequency doubling of a ring ti:sapphire laser using lithium tri-borate in an external enhancement cavity," Opt. Commun. **90**, 89 – 94 (1992).

[26] S. Bourzeix, M. D. Plimmer, F. Nez, L. Julien, and F. Biraben, "Efficient frequency doubling of a continuous wave titanium:sapphire laser in an external enhancement cavity," Opt. Commun. **99**, 89 – 94 (1993).

[27] M. Watanabe, R. Ohmukai, K. Hayasaka, H. Imajo, and S. Urabe, "High-power second-harmonic generation with picosecond and hundreds-of-picosecond pulses of a cw mode-locked Ti:sapphire laser," Opt. Lett. **19**, 637 – 639 (1994).

[28] C. S. Adams and A. I. Ferguson, "Frequency doubling of a single frequency $Ti : Al_2O_3$ laser using an external enhancement cavity," Opt. Commun. **79**, 219 – 223 (1990).

[29] P. F. Curley and A. I. Ferguson, "Resonant frequency doubling of an actively mode-locked $Ti:Al_2O_3$ laser using an external enhancement cavity," Opt. Commun. **80**, 365 – 369 (1991).

[30] A. Nebel and R. Beigang, "External frequency conversion of cw mode-locked $Ti:Al_2O_3$ laser radiation," Opt. Lett. **16**, 1729 – 1731 (1991).

[31] A. V. Smith, "How to select nonlinear crystals and model their performance using SNLO software," Proc. SPIE **3928**, 62 – 69 (2000).

[32] H. W. Kogelnik, E. P. Ippen, A. Dienes, and C. V. Shank, "Astigmatically compensated cavities for cw dye lasers," IEEE J. Quantum Elect. **QE 8**, 373 – 379 (1972).

[33] T. W. Hansch and B. Couillaud, "Laser frequency stabilization by polarization spectroscopy of a reflecting reference cavity," Opt. Commun. **35**, 441 – 444 (1980).

[34] C. Chen, "Recent advances in deep and vacuum-UV harmonic generation with KBBF crystal," Opt. Mater. **26**, 425 – 429 (2004).

[35] C. Chen, Y. Wang, B. Wu, K. Wu, W. Zeng, and L. Yu, "Design and synthesis of an ultraviolet-transparent nonlinear optical crystal $Sr_2Be_2B_2O_7$," Nature **373**, 322 – 324 (1995).

[36] F. Yang, Z. Wang, Y. Zhou, X. Cheng, S. Xie, Q. Peng, D. Cui, J. Zhang, X. Wang, Y. Zhu, C. Chen, and Z. Xu, "41 mW high average power picosecond 177.3 nm laser by second-harmonic generation in KBBF," Opt. Commun. **283**, 142 – 145 (2010).

[37] P. Lokai, B. Burghardt, and W. Mückenheim, "Sum-frequency generation in a cooled β-BaB_2O_4 crystal," Appl. Phys. B **45**, 245 – 247 (1988).

[38] Z. Min, R. W. Quandt, R. Bersohn, and H. L. Kim, "Extended range of second harmonic generation in $\beta - BaB_2O_4$," IEEE J. Quantum Electron. **34**, 2409 – 2409 (1998).

[39] A. P. Baronavski, H. D. Ladouceur, and J. K. Shaw, "Analysis of cross correlation, phase velocity mismatch, and group velocity mismatches in sum-frequency generation," IEEE J. Quantum Electron. **29**, 580 – 589 (1993).

[40] K. Kondo, M. Oka, H. Wada, T. Fukui, N. Umezu, K. Tatsuki, and S. Kubota, "Demonstration of long-term reliability of a 266-nm, continuous-wave, frequency-quadrupled solid-state laser using $\beta - BaB_2O_4$," Opt. Lett **23**, 195 – 197 (1998).

[41] K. Yamada, T. Yamazaki, N. Sei, T. Shimizu, R. Suzuki, T. Ohdaira, M. Kawai, M. Yokoyama, S. Hamada, K. Saeki, E. Nishimura, T. Mikado, T. Noguchi, S. Sugiyama, M. Chiwaki, H. Ohgaki, and T. Tomimasu, "Degradation and restoration of dielectric-coated cavity mirrors in the NIJI-IV FEL," Nuc. Instr. and Meth. A **358**, 392 – 395 (1995).

[42] G. P. Agrawal, *Nonlinear fiber optics* (Academic Press, 1989).

[43] B. Broers, H. B. van Linden van den Heuvell, and L. D. Noordam, "Large interference effects of small chirp observed in two-photon absorption," Opt. Commun. **91**, 57 – 61 (1992).

[44] S. Witte, R. T. Zinkstok, W. Ubachs, W. Hogervorst, and K. S. E. Eikema, "Deep-ultraviolet quantum interference metrology with ultrashort laser pulses," Science **307**, 400 – 403 (2005).

[45] R. T. Zinkstok, S. Witte, W. Ubachs, W. Hogervorst, and K. S. E. Eikema, "Frequency comb laser spectroscopy in the vacuum-ultraviolet region," Phys. Rev. A **73**, 061801(R) (2006).

[46] R. Holzwarth, "Measuring the frequency of light using femtosecond laser pulses," Ph.D. thesis, LMU (2002).

[47] J. C. Berengut, V. V. Flambaum, and M. G. Kozlov, "Calculation of relativistic and isotope shifts in Mg I," Phys. Rev. A **72**, 044501 (2005).

[48] M. G. Kozlov (2009). Private communication.

[49] T. Udem, J. Reichert, R. Holzwarth, and T. W. Hänsch, "Accurate measurement of large optical frequency differences with a mode-locked laser," Opt. Lett. **24**, 881 – 883 (1999).

[50] S. G. Porsev, M. G. Kozlov, Y. G. Rakhlina, and A. Derevianko, "Many-body calculations of electric-dipole amplitudes for transitions between low-lying levels of Mg, Ca, and Sr," Phys. Rev. A **64**, 012508 (2001).

[51] G. Risberg, "The spectrum of atomic magnesium, Mg I," Arkiv för Pysik **28**, 381 – 395 (1965).

[52] M. C. Fischer, "Höchstauflösende Laserspektroskopie an atomarem Wasserstoff," Ph.D. thesis, LMU (2004).

[53] H. A. Bethe and E. E. Salpeter, *Quantum mechanics of one- and two-electron atoms* (Dover, 2008).

[54] S. G. Karshenboim and V. G. Ivanov, "Hyperfine structure in hydrogen and helium ion," Phys. Lett. B **524**, 259 – 264 (2002).

[55] P. J. Mohr, B. N. Taylor, and D. B. Newell, "CODATA recommended values of the fundamental physical constants: 2006," Rev. of Mod. Phys. **80**, 633 – 730 (2008).

[56] M. I. Eides, H. Grotch, and V. A. Shelyuto, "Theory of light hydrogenlike atoms," Phys. Rep. **342**, 63 – 261 (2001).

[57] M. Fischer, N. Kolachevsky, M. Zimmermann, R. Holzwarth, T. Udem, T. W. Hänsch, M. Abgrall, J. Grünert, I. Maksimovic, S. Bize, H. Marion, F. P. D. Santos, P. Lemonde, G. Santarelli, P. Laurent, A. Clairon, C. Salomon, M. Haas, U. D. Jentschura, and C. H. Keitel, "New limits on the drift of fundamental constants from laboratory measurements," Phys. Rev. Lett. **92**, 230802 (2004).

[58] K. Pachucki, "Logarithmic two-loop corrections to the Lamb shift in hydrogen," Phys. Rev. A **63**, 042503 (2001).

[59] F. Biraben, "Spectroscopy of atomic hydrogen," Eur. Phys. J. Special Topics **172**, 109 – 119 (2009).

[60] F. Biraben. Private communication.

[61] J. W. M. DuMond and E. R. Cohen, "Least-squares adjustment of the atomic constants, 1952," Rev. Mod. Phys. **25**, 691 – 708 (1953).

[62] O. Arnoult, F. Nez, L. Julien, and F. Biraben, "Optical frequency measurement of the 1S-3S two-photon transition in hydrogen," ArXiv:1007.4794.

[63] A. Czarnecki, U. D. Jentschura, and K. Pachucki, "Calculation of the one- and two-loop Lamb shift for arbitrary excited hydrogenic states," Phys. Rev. Lett. **95**, 180404 (2005).

[64] U. Jentschura and K. Pachucki, "Higher-order binding corrections to the lamb shift of $2P$ states," Phys. Rev. A **54**, 1853 – 1861 (1996).

[65] L. P. Granath, "The absorption of ultra-violet light by oxygen, water vapor and quartz," Phys. Rev. **34**, 1045 – 1048 (1929).

[66] A. Sieradzan, M. D. Havey, and M. S. Safronova, "Combined experimental and theoretical study of the $6p\ ^2P_j \rightarrow 8s\ ^2S_{1/2}$ relative transition matrix elements in atomic Cs," Phys. Rev. A **69**, 022502 (2004).

[67] J. Lahiri and S. T. Manson, "Oscillator-strength distributions for discrete and continuum transitions of excited state of cesium," Phys. Rev. A **33**, 3151 – 3165 (1986).

[68] H. Uitenbroek and C. Briand, "The Mg 1 λ285.21 nanometer line: An example of non-LTE line formation," Astrophys. J. **447**, 453 – 463 (1995).

[69] O. H. W. Siegmund, *Vacuum ultraviolet spectroscopy II* (Academic Press, 1998), vol. 32, chap. Amplifying and position sensitive detectors.

[70] J. T. M. Walraven and I. F. Silvera, "Helium-temperature beam source of atomic hydrogen," Rev. Sci. Instrum. **53**, 1167 – 1181 (1982).

[71] V. A. Trofimov, A. A. Vasil'ev, A. I. Kovalev, and P. A. Kravtsov, "A two-coordinate detector for a beam of atomic hydrogen or deuterium," Instrum. Exp. Tech. **48**, 122 – 126 (2004).

[72] K. F. Wall, J. S. Smucz, B. Pati, Y. Isyanova, P. F. Moulton, and J. G. Manni, "A quasi-continuous-wave deep ultraviolet laser source," IEEE J. Quantum Electron. **39**, 1160 – 1169 (2003).

Danksagung

An dieser Stelle möchte ich Allen ganz herzlich danken, die mich bei meiner Arbeit unterstützt haben.

Insbesondere möchte Herrn Prof. Theodor W. Hänsch dafür danken, dass er mich in seiner Arbeitsgruppe aufgenommen und mir das sehr interessante und anspruchsvolle $1S - 3S$ Experiment anvertraut hat.

Herrn Prof. Kleineberg möchte ich für die Bereitschaft danken, das zweite Gutachten über diese Arbeit zu verfassen.

Einen großen Dank möchte ich an Thomas Udem richten, seine Tür stand immer für Diskussionen offen.

Sascha Reinhardt möchte ich für die sehr gute und freundschaftliche Zusammenarbeit an dem Projekt danken. Er brachte mich wieder auf den richtigen Kurs, wenn ich mich in Details verrannt hatte.

Ich möchte auch Scott Diddams für seine Unterstützung bei meinem Projekt in seiner Zeit als Gastwissenschaftler am MPQ danken.

Einen großen Dank möchte ich Karl Linner und Wolfgang Simon aussprechen. Ohne ihre Erfahrung und technische Fertigkeiten hätten viele Ideen nicht realisiert werden können. Ebenfalls einen großen Dank an Helmut Brückner, der mir nicht nur in Sachen Elektronik mit Rat und Tat geholfen hat. Ihm verdanke ich auch meine Ski-Fertigkeiten.

Maximillian Herrmann, Randolf Pohl und Sascha möchte ich für die kritische und konstruktive Korrektur dieser Arbeit danken.

Der gesamten Arbeitsgruppe möchte ich für die sehr freundschaftliche Arbeitsatmosphäre danken. Die gemeinsamen Ausflüge zum Klettern und Skifahren und die Grillabende an der Isar halfen den Kopf frei zu bekommen.

Zum Schluss möchte ich noch meiner Familie und insbesondere meinem Verlobten Johannes danken. Mit Geduld Vertrauen und Zuversicht haben sie mir an Tagen des Misserfolges Trost gespendet und halfen mir neuen Mut zu fassen. Ohne sie wäre die Arbeit nicht möglich gewesen.